Politecnico di Milano
Faculty of Industrial Engineering
Department of Mechanical Engineering

Master of Science Thesis

Numerical simulation of a pure water jet inside an orifice: jet stability and effects of droplets collisions

by

Francesco Arleo
ID number: 725352

Supervisors:
Prof. Massimiliano Annoni
Iraitz Etxeberria

San Sebastian - Milano
Academic year 2009/2010

To my family, with gratitude and sincere love.

Contents

Acknowledgments

The present study has been carried out in the frame of a collaboration between Dipartimento di Meccanica - Politecnico di Milano and Fatronik-Tecnalia. The author is sincerely grateful to both the institutions for the unique given opportunity.

Special thanks to professor Massimiliano Annoni for his patience and his invaluable and constant support, to Iraitz Etxeberria for her kindness and the support during my stay in Fatronik and to Alfredo Suarez Gonzalez and Fernando Veiga Suarez, irreplaceable friends and colleagues.

Chapter 1

Introduction and literature review

Recent technological progresses often bring along a down-sizing of products together with small tolerances and high precision: this trend push machining technologies to continuously improve in order to reach higher and higher standards of quality and precision on the workpieces and the capability to machine always smaller and more complex parts. Water jet cutting has always been a promising technology because of its inner simplicity and its extreme flexibility, even if often it suffers a lack of high precision, especially if compared to technologies such as laser cutting. In order to gain competitiveness and satisfy quality requirements, water jet cutting is in need of a more systematic insight of its process aiming to achieve awareness on the physics and the main causes of the disturbances which are systematically affecting the jet. Furthermore, due to the high velocities reached by the jet and the rapid dynamics in conjunction with the small characteristic dimensions of the process, quantitatively correct experiments and the empirical approach are often very difficult: it is then obvious that numerical simulations would be an invaluable and promising mean to reach a better understanding of the process and optimize such a complex unsteady turbulent two-phase micro flow. Watching a pure water jet working, it is possible to notice naked-eye that sometimes the jet pulsates losing its coherence for short whiles, spreading wider and then coming back to a stable condition: this is a random phenomenon which happens with no regular frequency whose causes are basically still unknown.

The aim of the present work is to perform a CFD numerical simulation of a pure water jet in order to investigate its creation and stability achieving a better understanding of the process and its disturbances. The internal geometry of the orifice plays an important role during the first instants of the jet creation

affecting the jet break-up and the creation of droplets which remain inside the orifice sticking or rebounding on the walls of the orifice exit tube. A CFD analysis is carried out to study the effect of the droplet collision with the main jet: the jet break-up, early presence of water, condensed humidity or jet disturbances can produce these water droplets which then can be dragged by the high velocity air field created inside the orifice tube by the main water jet. Droplets can later collide along the main jet or be sucked up toward the capillary (the upper small orifice hole where the jet is created) causing local disturbances and loss of the hydraulic flip condition which is crucial for the coherence of the jet. This random process effectively explains the instabilities which can usually be noticed by a naked-eye observation during the water jet formation and later on; the study of this phenomena can lead to new instruments for an improved design of water jet cutting head components on the way to high precision applications.

This work is actually a first attempt to analyze more deeply this problem by means of numerical simulations: it becomes a starting point for future developments in this direction with the aim of understanding and possibly solving or limiting the disturbances obtaining a more and more stable process.

Finally, the present report is organized into two main parts:

1. **Part I: THEORETICAL REVIEW** which presents the theoretical background on fluid dynamics and computational fluid dynamics which and that can be useful for non-expert readers in order to fully understand the results presented in the second part.

2. **Part II: ANALYTICAL, EXPERIMENTAL AND NUMERICAL ANALYSIS** which is specifically focused on the presentation of the work done during the present study.

1.1 Literature review

Several studies have been performed on the breakup mechanisms, stability and quality of water jets produced by different types of orifices working in different conditions. Cavitation and hydraulic flip inside orifices and injectors turn out to have a great importance on the quality and the flow regime of the produced jet, and a lot of efforts have been made in order to gain knowledge on these phenomena both theoretically and experimentally.

The first great contributions on these topics were given in 1936 by Ohnesorge [1], who presented a classification of flows regimes in rounded-edge nozzles working at different Reynolds and Weber numbers, and in the late 1960s by A. Lichtarowicz *et al.* [2], who collected comprehensive results of experimental investigations on the discharge coefficients of orifices with length to diameter ratios up to 10 working at Reynolds numbers up to 10^5.

A. H. Lefebvre *et al.* [3] proposed a well known work about the spray atomization theory which is still largely used especially in the field of injectors.

K. A. Sallam *et al.* [4] carried out an experimental study on liquid column breakup lengths and turbulent primary breakup properties at the surface of turbulent round liquid jets in still air at standard temperature and pressure; tests were performed on non-cavitating water and ethanol flows produced by constant section and long length to diameter ratios (greater than 40) orifices with Reynolds numbers and Weber numbers respectively ranging from 5000 to 200000 and from 235 to 270000.

A. Sou *et al.* [5] investigated the effects of cavitation on liquid jets under various conditions and Reynolds numbers in liquid jet produced by two-dimensional nozzles, pointing out the different produced flow regimes, such as cavitation, super-cavitation (atomization) and hydraulic flip.

M. Annoni *et al.* [6] presented a work dealing with the effect of diamond orifice geometry on the cutting performance and jet stability in cone-up and cone-down geometry orifices by measuring their coefficients of discharge.

Furthermore, numerical methods have been largely employed in order to have a deeper understanding on the physics phenomena affecting the jet quality. Among others, N. Anantharamaiah *et al.* [7] investigated on how the operating pressure and the nozzle inlet sharpness influence the dynamics of fluid flow by monitoring the formation and growth of the cavitation cloud inside a sharp-edge hydroentangling nozzle at pressures ranging from 10 to 200 bars.

W. Yuan *et al.* [8] indicated the potential of cavitation for enhancement of atomization and spray quality in injection nozzles and demonstrated the strong interaction between cavitating nozzle flow and the produced jet quality.

S. Dabiri *et al.* [9] identify the potential locations for cavitation induced by total stress on the flow of a liquid through an orifice of an atomizer; a new criterion was proposed

N. Anantharamaiah *et al.* [10] studied the role of nozzle geometry on the formation of constricted water jets carrying out numerical of water flow simulations through sharp-edge cone-capillary nozzles having a diameter of 128 μm at different Reynolds numbers, while A. T. Basha *et al.* [11] proposed a similar numerical analysis regarding water jet cutting orifices at different length to diameter ratios and working pressure ranging from 10 to 700 MPa.

These works are a selection among the several works reviewed during the present study and effectively forming its theoretical background guideline. Moreover, further works are referenced throughout the present report concerning specific topics presented in each section.

As a matter of fact, few works in the previous literature have been carried out on topics regarding the analysis of jet flow regimes and quality by means of numerical simulations which can turn out to be an helpful mean to gain

knowledge on the process mechanisms and improve the control capabilities. Moreover, most of the previous studies were performed on water jet nozzles working in completely different conditions than the ones employed in water jet cutting applications: usually, orifices with different geometry and working at lower upstream pressures are tested and the flow regime and coherence analysis always refer to steady working conditions; besides, no explicit analysis on jet stability have been performed regarding working sharp-edge orifices at high pressures as in the case of water jet cutting applications.

In this scenario, the present work offers a new perspective as it specifically focuses on occasionally random instabilities of a pure water jet.

Part I

THEORETICAL REVIEW

Chapter 2

Water Jet Technology

Water jet (WJ) is a generic term used to describe equipment that uses a high velocity stream of water for cutting or cleaning purposes. The process is essentially the same as water erosion found in nature but greatly accelerated and concentrated. High-pressure water is forced through a small hole (typically called *orifice* to concentrate an extremely high amount of energy in a small area: high pressure energy is converted in kinetic energy in the capillary restriction of the tiny orifice, creating a high-velocity beam of water.

In the 1950s, forestry engineer Norman Franz experimented with an early form of water jet cutter to cut lumber. However, the technology did not advance notably until the 1970s when Mohamed Hashish created a technique to add abrasives to the water jet cutter. Today the water jet is unparalleled in many aspects of cutting and has changed the way many products are manufactured: many types of water jets have been developed during these years, including plain water jets, abrasive water jets, percussive water jets, cavitation jets and hybrid jets [12]. The reason why WJ technology has encountered an always growing success is the fact that it is a simple, versatile and flexible machining tool which can cut a wide variety of parts from a wide variety of materials in an efficient and cost-effective way.

2.1 The water jet cutting system

A typical WJ cutting plant is represented in Figure 2.1. The main components are briefly presented below [13].

Water treatment WJ utilize specially designed pumps and nozzles that require a specific water quality threshold in order to work properly. Common criteria and specifications for water jet water are: dissolved solids under 100 or 150

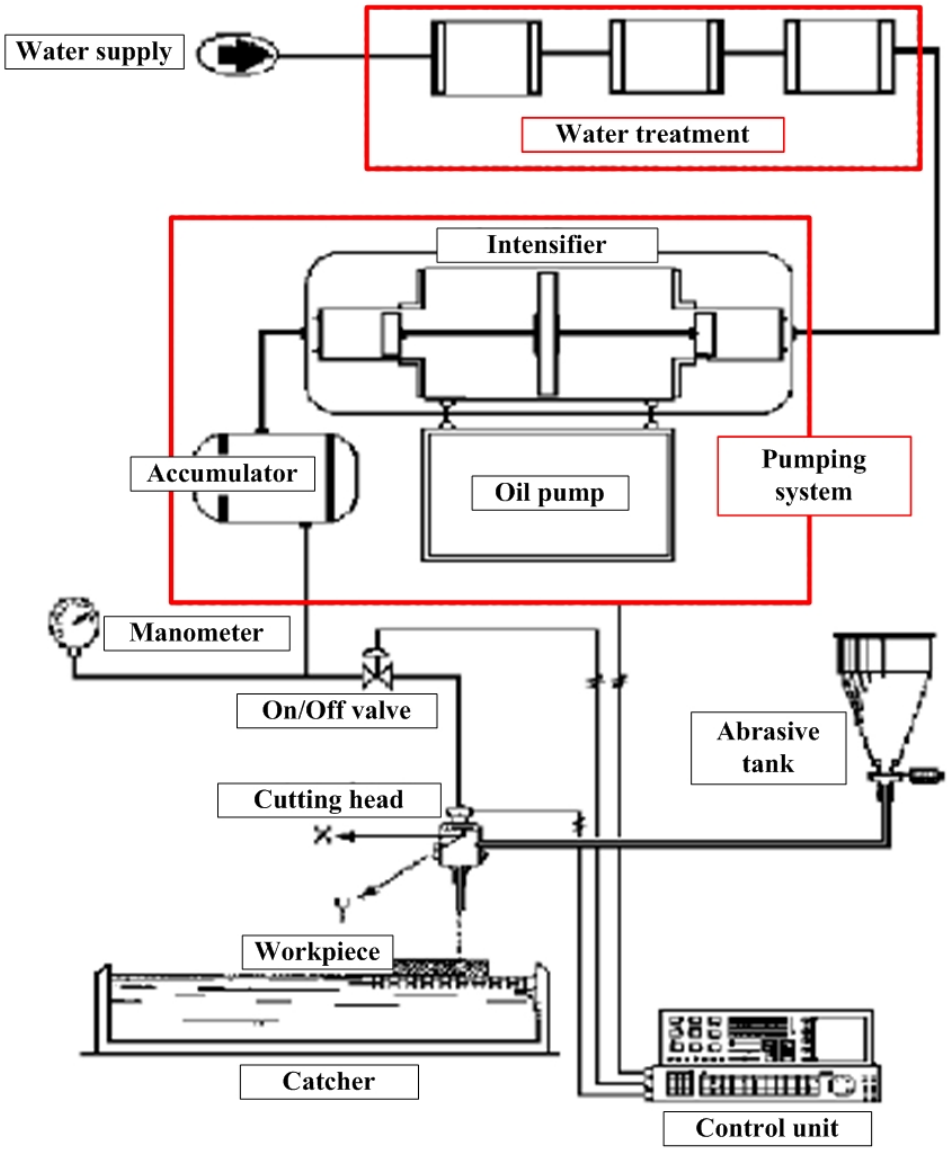

Figure 2.1: *Scheme of a typical WJ system [13]*

parts per million, hardness under 80 parts per million and *pH* between 6.5 and 8.0. Water quality is crucial for system life and proper functioning as suspended particles in tap water can accelerate wearing of the pumping system, fittings, valves and of course orifices; besides, calcium and magnesium salts dissolved in water can create deposits or encrustations which reduce the pipes section affecting the system efficiency; finally, chlorides and sulfates can cause local corrosion.

Water treatment system is installed upstream the pumping system and is usually composed of micrometric filters and a reverse osmosis apparatus: this way, the pureness of the water is guaranteed.

Pumping system This is actually the core of the WJ process where the water pressure is raised from water supply pressure up to the working pressure. It is formed by the following components:

Low-pressure circuit : it is powered by an oil volumetric pump which feeds the low-pressure circuit. The working pressure is around 20 MPa.

High-pressure circuit : it is powered by the water pump fed by the oil coming from the low-pressure circuit: the oil acts on the primary piston pushing it forward and backward; a secondary piston with reduced section is connected to the primary and the water pressure is increased proportionally to the ratio between the areas of the primary and secondary piston.

Two types of water pumps exist, as presented in Figure 2.2: single effect and double effect pumps. In the double effect pumps, the primary piston has two active strokes compressing water alternatively on the left and on the right, while in the single effect pumps, each piston has just one active stroke and because of this reason two or more pistons are coupled in order to have more continuity in pumping water.

Accumulator : when a double effect pump is used, its alternative motion produces fluctuating pressure and an accumulator (i.e. a tank with a capacity around 2 liters) is needed in order to dump the pressure oscillations and maintain at a more constant value the pressure in the downstream circuit.

In case of single effect pumps, an adequate phasing of the single piston strokes allows to obtain less pressure fluctuations and the accumulator is not needed.

Cutting head: downstream the pumping system, high pressure water reaches the cutting head where the nozzle is contained and the jet is created, with the possible addition of abrasive in case of AWJ.

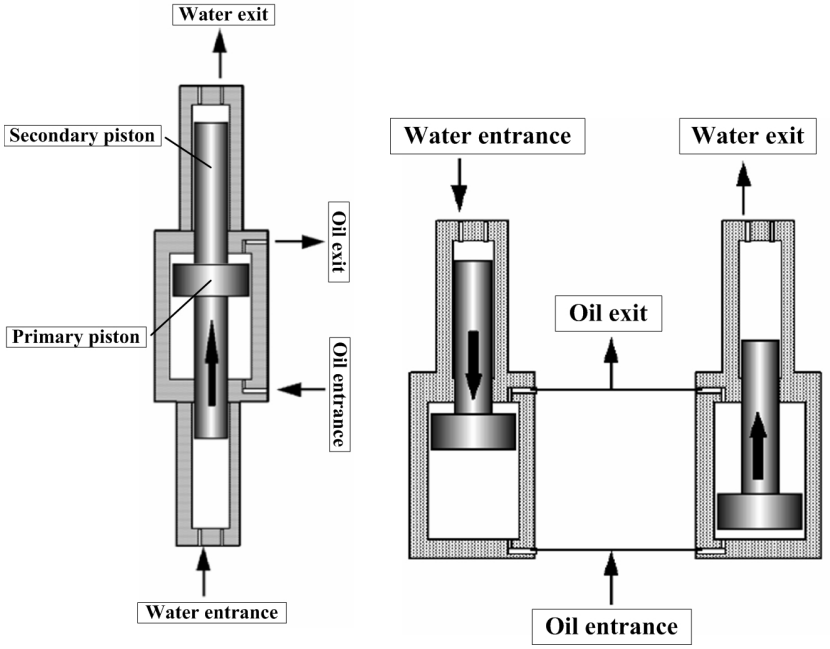

(a) *Double effect pump scheme* **(b)** *Single effect pump scheme*

Figure 2.2: *Comparison between a double effect **(a)** and single effect **(b)** pump.*

Catcher: once the jet has cut the material, water, abrasive and scraps are collected in a tank called catcher. Moreover, the catcher allows to dissipate the remaining energy of the jet avoiding reflections or reboundings against machine parts or operators.

A complete WJ system, including the high-pressure water pump, the handling system, the catcher and the abrasive feeding system costs from 50000 to 300000 €, with 150000 €being the average price for a mid-range WJ cutting system. Obviously, prices can run considerably higher than this for customized systems or very large WJ cutting systems.

2.2 Pure water jet and Abrasive water jet

The two most wide-spread WJ technologies in cutting applications are Abrasive Water Jet and Pure Water Jet: Abrasive Water Jet (AWJ) is a category of WJ in which abrasive is introduced to improve the process cutting capability, while Pure Water Jet (PWJ) is a term used for specifically distinguish water jet without abrasive. Typical PWJ and AWJ nozzles are put side by side in Figure 2.3c.

As PWJ uses the beam of water exiting the orifice to cut directly, it is basically employed just for soft material like food, clothes, foam, rubber, candy bars or thin soft wood, but is not effective for cutting harder materials. Figure 2.3a

shows a scheme of a typical PWJ cutting head. The orifice diameters used in PWJ applications are very small (between 0.05 and 0.15 mm) in order to form a ultra-thin jet and concentrate all the energy in the smallest possible area to improve cutting power. Typically, problems related to PWJ nozzles regard the orifice: they can crack, clog, or suffer the presence of deposits on them. Cracking and clogging happen as a result of dirty inlet water, and are typically avoided by a proper water purification in the water treatment system. Deposits accumulate gradually as a result of minerals in the water. Depending on the water supply, slightly fancier filtering may be necessary. Orifices are easily replaced in about two to ten minutes, and are typically cheap (from 5 to 50 €). There are also diamond orifices (200 € and up) which can last much longer due to the higher hardness and wear resistance.

Considering AWJ, an opening on the side of the cutting head allows for the introduction of the abrasive inside a *mixing chamber* where interacts with the high-pressure water stream, as shown in Figure 2.3b; abrasive particles are later accelerated in a *focusing tube* before the mixture exits the nozzle. Generally, bigger diameter orifices (from 0.25 mm up) are used in AWJ in order to increase the water flow rate and allow a more effective drag of the abrasive particles; diameter of the focusing tube is usually 3 times bigger than orifice diameter and its standard total length is 76 mm. The increased erosive power due to the addition of abrasive produces a jet able to cut hard and resistant materials such as metals, ceramics, glass or multilayer. Despite their simple design, AWJ nozzles can be subject to the main problems listed below:

- The AWJ cut through almost anything, including itself. Focusing tube is expensive and wears out in about 80-100 hours of use. Replacing mixing tubes is a large part of the operating costs;

- Due to dirt, large particle in the abrasive or moisture, abrasive can occasionally stuck inside the nozzle causing an arrest of the process. This used to be a big problem, but it is getting better with new designs of focusing tubes and abrasive inlet channel;

- The orifice needs to be precisely positioned in the cutting head and it works properly while water at high pressure impacts it: wear, misalignment, and damage to the orifice can cause a poor quality of the jet at the exit.

Due to their different complexity, the two systems differ also in the price: a complete PWJ nozzle assemblies cost around 500 to 1000 €, while AWJ cutting heads cost from 800 to 2000 €; the AWJ also requires support hardware for abrasive feed which can cost from around 500 to 2000 €. Obviously, the cost of cutting operations is much higher for the AWJ compared to PWJ because of focusing tube and mixing chamber wear, and abrasive consumption.

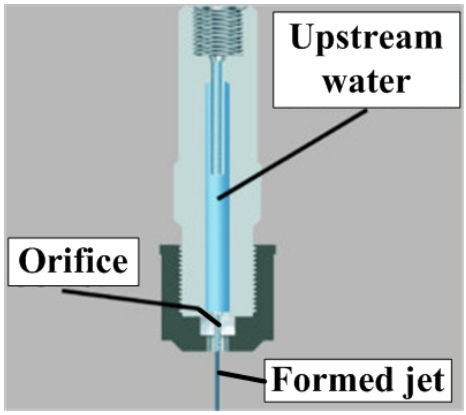

(a) *Pure water jet nozzle scheme*

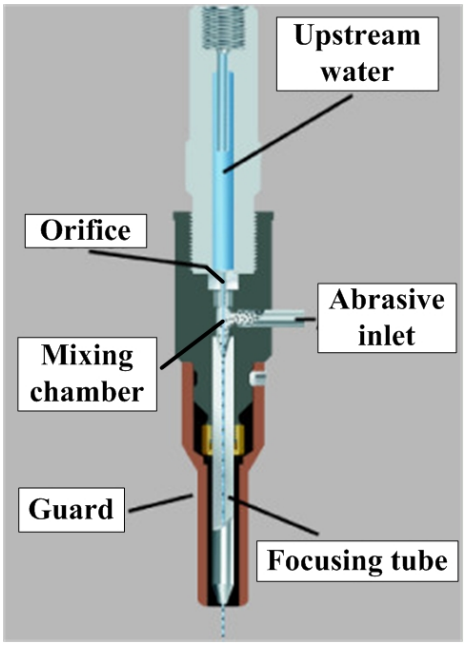

(b) *Abrasive water jet nozzle scheme*

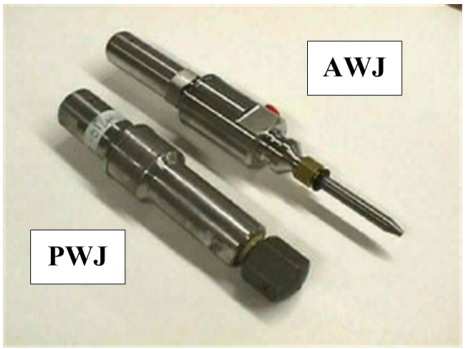

(c) *Typical PWJ and AWJ nozzles*

Figure 2.3: *Difference between typical PWJ and AWJ nozzles [14].*

2.3 Advantages of water jet cutting

There is a reason why WJ machining has rapidly grown in popularity since the mid-1990s. Actually there is a number of reasons, but they mostly come down to versatility and flexibility in the end. Allowed by its simple physical principle, a large amount of different applications have been developed during years, apart from cutting, making this technology probably one of the most flexible existing.

Limiting the analysis just to cutting operations, the main advantages of WJ are listed below:

Cutting virtually any material: since WJ cuts using water and abrasive, they can manufacture a wide variety of materials; for example, it doesn't need the target material to be conductor.

No mechanical stresses: WJ machining introduces only slightly compressive stresses into the material.

Almost no heat generation: just little heat is generated by the process and it is absorbed by the water and carried into the catcher. The material itself experiences almost no change in temperature during machining. In worst cases, during piercing or cutting thick metals with low feed rates, temperatures may rise up to 50 °C. The result is that there is no heat affected zone (HAZ) in the material which means that it is possible to machine without hardening the material, generating poisonous fumes, recasting, or warping. Moreover, it is possible to machine parts that have already been heat treated.

Ability in machining thick materials: even if most of the machined products are generally cut out from steel sheets with thicknesses under 2.5 cm, it is quite common to machine up to 10 cm with a maximum possible thickness of about 20 cm on steel. The thicker the material is, the longer it will take to cut: a part made of a material twice as thick will take more than twice the time. Moreover, multilayer materials or metals can be easily cut.

Almost no burrs production: if the process is adequately set up very little burrs are left on the machined part.

Soft fixturing for most parts: there are very low sideway forces in WJ machining which take place at high feed rates; the downward forces are also small, in the range of a few newtons. Typically, a large force is produced by the water in the tank, pushing upward against the material.

Removal of a small material amount: the amount of material removed by the WJ stream is typically about 1 mm wide, meaning that very little material is removed in a passing through cut. When working with expensive materials

(such as titanium) or hazardous materials (such as lead), this can be a significant benefit. It also means that you can get more parts from a given sheet of material and the final scrap still has value since chunks instead of chips are obtained.

Environmental sustainability: AWJ typically uses garnet as abrasive material, which is non-reactive and biologically inert mineral. As long as a material that is hazardous is not machined, the spent abrasive and waste material become suitable for landfill. The garnet abrasive is inert and can be easily disposed.

If lead or other hazardous materials are machined, the waste needs to be disposed appropriately, and water has to be recycled. However, very little metal is actually removed in the cutting process: this keeps the environmental impact relatively low, especially if hazardous material is machined occasionally. In most cases, excess water is simply drained to the sewer, even if sometimes water treatments may be necessary before the sewer. In few cases, a "closed loop" system that recycles the water may be required. Most of the environmental (and cost) impact is due to the pumps which use a considerable amount of electricity.

As WJ is trying to gain a more and more important place among non-conventional cutting technologies, next sections will present a series of advantages which WJ offers if compared to two direct competitor technologies such as laser and EDM.

2.3.1 Advantages of water jet compared to laser machining

When cutting a relatively thin material with high compatibility to laser radiation (i.e. low reflectivity and transparency to laser radiation), laser technology is probably the most precise and fast cutting technology and the best choice to satisfy high production volumes. Anyway, WJ has a number of advantages over lasers, even the two tools are complementary if in many cases and many machine shops own both of them. A list of the main advantages is presented below:

Manufacturing of a wider range of materials: WJ can cut a wide range of materials without requiring important changes in setup required. Moreover it can machine reflective materials that lasers cannot, such as copper and aluminum, and materials which are heat-sensitive can be machined as well.

No HAZ: WJ cutting does not heat your part and does not change the properties of the material. As a conclusion, there is no HAZ or thermal distortion, which can occur with lasers.

Manufacturing of thicker materials: rising up pressure and slowing down the feed rate it is possible to cut much thicker parts. WJ easily handles up to 100 mm steel, although some applications have used AWJ on thicknesses up to 250 mm in steel, even if in this latter case, it is difficult to maintain precision through all the thickness and the process is really slow. On the contrary, lasers seem to have a maximum practical cutting thickness up to 20-25 mm depending on the material to be cut. Moreover, WJ offers better tolerances on parts thicker than 10 mm. For thinner parts, both WJ and lasers offer comparable tolerances.

Manufacturing of multilayer materials: multilayer materials are practically impossible to be cut with laser due to the different behavior of each material to laser radiation, while WJ does not have any problems in machining these products, except for delamination in some cases.

Lower capital equipment and maintenance cost: the cost of a WJ machine is generally much lower than the cost of a laser system. Also the cost per machined part is slightly lower in case of WJ cutting. Finally, maintenance is easier and cheaper for a WJ system than for a laser.

Better edge finish and no burrs: materials cut by WJ have a fine, sand-blasted surface because of the way the material is abraded, which makes it easier to make a high-quality weld. Especially,thick materials cut by laser tend to have a rougher, scaly edge, which may require additional machining operations to clean up. Moreover, WJ produces less or even no burrs on the finished workpiece.

Independence from sheet-metal planarity: in laser applications, the material needs to be relatively uniform, since when cutting over uneven surfaces, the laser can lose its focus and therefore cutting power. A WJ still retains much of its cutting power over uneven material; although the material may deflect the cutting stream, it typically has a negligible effect.

More environmental sustainability: as presented in the previous Section 2.3.1, WJ is basically a more environmentally friendly technology compared to laser.

2.3.2 Advantages of water jet compared with EDM machining

EDM stands for Electrical Discharge Machining and is used to machine electrically conductive materials, essentially eroding the metal using electricity. An electrical arc rapidly discharges between an electrode and the workpiece. A high-frequency series of arcs removes metal by melting it and vaporizing it,

while the material particles removed are flushed away by a continuously circulating non-conducting fluid, such as deionized water or kerosene. EDM can create intricate shapes in hard materials that are difficult to machine using traditional methods, satisfying very small tolerances with excellent surface finishing. The main drawback of this process is that it is really slow.

The main advantages of WJ over EDM are the following:

Faster: AWJ are much faster than EDM in metal cutting.

Manufacturing of a wider range of materials: Waterjets can machine almost any material, included non-conductive materials, such as glass, wood, plastic, and ceramic.

Make its own pierce hole: in some types of EDM, such as wire-EDM, a hole needs to be first made in the material, which has to be done by a separate process. WJ can pierce the material on its own, requiring no additional fixturing or machining.

No HAZ: in WJ cutting there is no HAZ, thermal distortion or change in the properties of the material, which can occur with EDM.

Cutting of pieces: the size of the part created with a WJ is limited by the size of the material or the x-y table of the WJ machine, while machining big partd by means of EDM is quite uncommon and difficult.

Less setup required: the setup process in WJ is generally more straightforward, since often setup needs more attention in EDM, especially in operations involving complex matrices or in wire EDM.

2.4 Limitations

The main drawback of WJ cutting is the fact that it is pretty slow especially in AWJ application on thick materials. AWJ also suffers a lack of high-precision when cutting thick pieces: typically tolerances around 0.05 mm can be reached with recent WJ machines.

Moreover, there are some very few materials that WJ cannot cut such as diamonds and tempered glass: diamonds are too hard to cut (and there may be a few other very hard materials that can't be cut), while tempered glass will shatter when it is cut with a WJ because it is designed to shatter when it's disturbed. Besides, a few advanced ceramics are so hard that it's not economically convenient to cut them and some composite materials can't be cut as well because the water can seep between the layers and cause delamination.

Furthermore, the WJ process produces loud noise, even if this problem can be limited by cutting the pieces dipped under water.

Chapter 3

Fluid Dynamics

3.1 Fluid as Continuum

Fluids are made of rapidly vibrating molecules situated at a distance much greater than their dimensions.

In such a discontinuous medium, dealing with any physical property (e.g. density, velocity, pressure, viscosity,. . .) of each point has no sense, as long as it would be variable in space and time depending whether a molecule is present or not.

It is anyway possible to disregard from this discontinuous nature by considering a not too small volume of fluid containing a set of molecules, so that it is possible to refer all the kinematic values to its *center of inertia* and all the physical intensive properties to its volume. The density will then be the ratio between the mass of the molecules and the occupied volume, the acceleration will be the one of the *center of inertia*, and so on.

Whereas the volume of this set of molecules is anyway much smaller than the order of magnitude of the length scale interesting fluid mechanics, it is clearly possible to assume that this fluid behaves as a *continuum*. Based on this assumption, Eulero founded the *Mechanics of Continuum* [15].

3.1.1 Physical Properties

The fluids can be divided into two main categories: *liquids* and *gases*. We call liquids the fluids which have low compressibility and show great resistance to volume variations; as a consequence, they'll tend to fill just the bottom of the container where they are put inside, and it is always possible to define an interface with atmosphere that it is usually called *free surface*. On the other hand, gases have high compressibility and normally can bear higher volume variations

offering lower resistance; as a consequence, they tend to expand and fill all the space in which they're contained.

Furthermore each fluid has specific physical properties which define its physical behavior. The main physical properties are listed below.

Density and Specific Gravity

Density ρ is the ratio between the mass and the volume containing it; the measurement unit in the International System (I.S.) is kg/m^3.

Specific gravity γ is the weight of a volume unit and it is measurement unit in the I.S. is N/m^3.

A well known relation exists between the two quantities:

$$\gamma = \rho \cdot g \tag{3.1}$$

where g is the gravity acceleration whose value can be well approximated by $9.81\ m/s^2$.

Both density and specific gravity are function of the pressure p and the temperature T; commonly, the relation

$$\rho = \rho(p, T) \tag{3.2}$$

is called *equation of state* of the fluid.

The following experimental relation is generally used for water at atmospheric pressure:

$$\rho = \rho_0 + 5.29\ 10^{-5} \cdot T - 6.53\ 10^{-6} \cdot T^2 + 1.45\ 10^{-8} \cdot T^3 \tag{3.3}$$

where $\rho_0 = 999.46\ kgm^3$ is the value of density at 0 °C. The variations are smaller than 0.8% in the range of temperature 0 °C $< T <$ 40 °Cand it is then possible to neglect them and using an approximated value of $1000\ kg/m^3$ for the density.

Compressibility

Every fluid shows a change in volume (and density) depending on the pressure surrounding it. As stated before, compressibility is the main evident difference between a liquid and a gas; their behavior is presented separately below:

Liquid Let's consider a volume V of liquid surrounded by a pressure p eventually varying in space and time; increasing the pressure p by a constant value dp along the whole surface, it is possible to notice that it undergoes a reduction of the volume dV proportional both to dp and V:

$$dV = -\frac{V}{\epsilon} \cdot dp \tag{3.4}$$

where ϵ is a physical property of the liquid called *modulus of elasticity of volume* $[N/m^2]$: the higher it is the more the liquid offers resistance to changes in volume.

Generally it is preferable to show the density ρ instead of the volume V in (3.4); considering that the mass ρV remains constant, we obtain $\rho dV + Wd\rho = 0$ by differentiation, and using the (3.4) the equation:

$$\frac{d\rho}{\rho} = \frac{dp}{\epsilon} \tag{3.5}$$

.

In a liquid, ϵ has an order of magnitude up to $10^9 N/m^2$; for water at a temperature of 10 °C, ϵ is around $2.03 \cdot 10^9 N/m^2$.

Furthermore, ϵ is barely dependent on pressure, while it could change with more evidence proportionally to temperature; e.g. with an increase in temperature from 0 °C to 30 °C, the value of ϵ rise up about 10%.

The high values of ϵ allow to neglect compressibility in most of the cases so that we can consider the density of the liquid (and so the specific gravity) constant: $\rho = cost$. In the case of WJ applications anyway, due to the very high pressures that usually are reached in the process, it is not fair to account for compressibility; the relation often used in this case is

$$\rho = \rho_{\text{amb}} \cdot \left(1 + \frac{p - p_{\text{amb}}}{L}\right)^c \tag{3.6}$$

where ρ_{amb} is the reference ambient pressure, L and c experimental parameters whose value are respectively $L = 300MPa$ and $c = 0.1368$.

Figure 3.1 shows how density varies in percentage as a function of the pressure, according to equation (3.6): it is possible to notice that the percentage stays below 10% up to 300MPa; if this is not crucial for the problem, complicating a model by considering compressibility is than senseless at low pressure values.

Gas The *equation of state* usually applied in this case is the perfect gases one:

$$\frac{p}{\gamma} = RT \tag{3.7}$$

where p is the absolute pressure and T the absolute pressure measured in Kelvin degrees (K) and R is the *constant of perfect gas* given by

$$R = \frac{848}{M} \frac{\text{mol}}{K} \tag{3.8}$$

where M is the molecular weight of the specific gas.

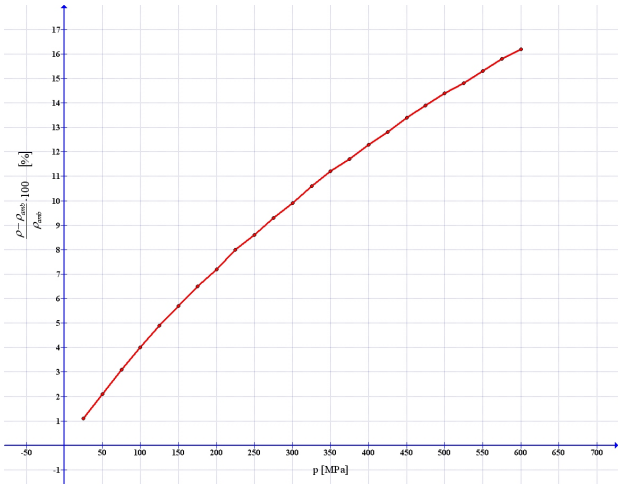

Figure 3.1: *Density variation in percentage as a function of pressure; reference value* $\rho_{\text{amb}} = 1000 kg/m^3$

Surface Tension

When a liquid interfaces with another not-miscible fluid (liquid or gas) the surface of separation behaves like an elastic membrane subjected to a uniform stress field: this property is called *surface tension*. If we cut this surface along a line, a force F needs to be applied in order to keep the two sides of the cut together: the surface tension is expressed as the ratio between this force and the length $s = F/L$ and is measured according to IS in (N/m).

It is function of the two interfacing fluids and the temperature: more precisely, the surface tension decreases when temperature increases, while, for a given liquid, its values are slightly changing with the nature of gases.

Because of its spread use, it is common to find tables with air at a temperature $T = 20$ °Cas reference fluid, like Table 3.1.

Primary fluid: AIR, $T = 20$ °C	
Secondary Liquid	s (N/m)
Water	0.073
Mercury	0.559
Benzene	0.029
Olive oil	0.319

Table 3.1: *Surface tension between different liquids and air [15].*

Viscosity

While moving, each fluid is subjected to internal stresses both normal and tangential: while normal stresses are always present, even when the fluid is static, tangential stresses occur just during the motion and cease to exist when the fluid is quiet. Moreover, tangential stresses oppose to the flow and their intensity is dependent on the rate of deformation as much as on some fluid's physical properties. A widespread expression of the local tangential stress, also called as *Newton's law*, is:

$$\tau = \mu \cdot \frac{du}{dn} \tag{3.9}$$

where n is the normal to the motion direction and μ is viscosity.

Therefore, viscosity is a physical expression of the *internal friction* of a fluid which describes the internal resistances generated during the fluid motion. Viscosity is expressed in N s/m^2 according to IS, even if it is possible to find it also in the equivalent form Pa·s.

An experiment showing the different behavior of two fluids with different viscosity is presented in Figure 3.2: the cylinders containing the fluids start rotating around their axis with the same angular velocity (pictures refer to the same instant): the layers which are close to the wall start moving soon due to the no-slip boundary condition while the layers far away from the wall start moving later. The distance from the wall that is affected by the motion is also called *viscous diffusion length* and it is increases as time goes on. Higher tangential stresses due to a higher viscosity, (case **(b)**) make the deformation propagate more deeply inside the fluid than in case **(a)** where viscosity is 10 times smaller.

(a) *low viscosity:* $\mu = 10$ *mPa s.* **(b)** *high viscosity:* $\mu = 100$ *mPa s.*

Figure 3.2: *Comparison between two fluids respectively with low* ***(a)*** *and high* ***(b)*** *viscosity.*

In most of the cases and for most of the fluids in practical applications, the value of viscosity keeps almost constant at least in a specific range of temperatures: these kind of fluids are called *Newtonian*; for instance, all the gases and all the homogeneous not-macromolecular liquids belong to this category.

In fluid mechanics is common to refer also to another parameter ν that is called *cinematic viscosity*, which is the ratio between the *dynamic viscosity* μ and the *density* ρ:

$$\nu = \frac{\mu}{\rho} \tag{3.10}$$

expressed with m^2/s according to IS.

Stresses inside continuum

Usually the forces acting on a continuum are divided into two main categories: *mass forces* and *surface forces*.

Mass forces are all the external forces acting remotely on the matter and proportionally to its mass; generally they are expressed as force per unit mass N/kg.

Surface forces are the ones acting on a specific area of the fluid across its boundary surface; generally they are expressed as surface stresses N/m^2.

The stress field in a point generally depends on the inclination of the surface element where it acts; as a consequence, the stress distribution around a point in the continuum is tightly related to the surface tilt. In order to analyze this stress distribution it is usual to refer to Cauchy tetrahedron, centered in point O as shown in Figure 3.3.

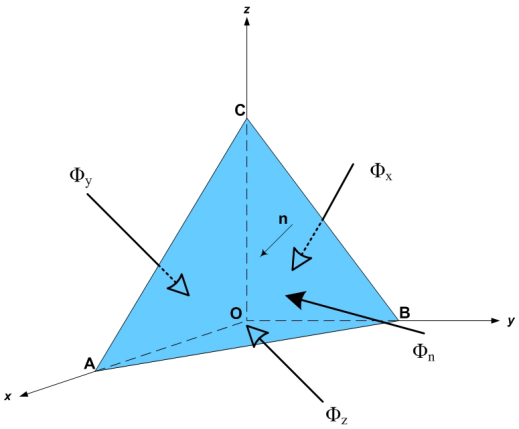

Figure 3.3: *Cauchy tetrahedron for the stress field analysis*

The vectors $\mathbf{\Phi_i}$ represent the generic stresses acting on the surface perpendicular to i-direction and $\mathbf{n}$ is the unit vector perpendicular to the face ABC inclined in a random way and identified by the angles $\hat{nx}$, $\hat{ny}$, $\hat{nz}$ formed with the principal axis.

As long as fluids can not withstand significant tensile stresses, most of the time fluid dynamics deals with compressive stresses: consequently it is usual to consider positive the unit vector pointing toward the inside of the element contrarily to the convention used in the elastic theory of solids.

The forces pushing on the four faces are obviously proportional to the faces area; naming A the area of the face ABC, they can be expressed as follows:

$$-\mathbf{\Phi_x} A \cos \hat{nx}; \quad -\mathbf{\Phi_y} A \cos \hat{ny}; \quad -\mathbf{\Phi_z} A \cos \hat{nz}; \quad \mathbf{\Phi_n} A \tag{3.11}$$

Being proportional to the area, they are a second order infinitesimal, while the mass and inertia forces are proportional to the volume, and so they are a

third order infinitesimal: for this reason it is possible to neglect them.

For the first cardinal equation of dynamics (static and dynamic equilibrium) it is possible to write:

$$\mathbf{\Phi_n} = \mathbf{\Phi_x} \cos \hat{nx} + \mathbf{\Phi_y} \cos \hat{ny} + \mathbf{\Phi_z} \cos \hat{nz} \tag{3.12}$$

which synthesizes the *Cauchy's theorem*:

Theorem. *In a point, the stress acting on an element generically inclined is a linear function of the stresses acting in the same point on three faces orthogonal to each other.*

The projections of the stresses along the three axis are indicated with a double index: the first index represents the direction perpendicular to the face where the stress is acting and the second index the direction along which it is projected; eg. Φ_{xn} is the projection of the stress $\mathbf{\Phi_n}$ along the direction of the x-axis. The vectorial equation (3.12) can be then split into the following three scalar equations:

$$\begin{aligned}
x-\text{axis}: &\quad \Phi_{nx} = \Phi_{xx} \cos \hat{nx} + \Phi_{yx} \cos \hat{ny} + \Phi_{zx} \cos \hat{nz} \\
y-\text{axis}: &\quad \Phi_{ny} = \Phi_{xy} \cos \hat{nx} + \Phi_{yy} \cos \hat{ny} + \Phi_{zy} \cos \hat{nz} \\
z-\text{axis}: &\quad \Phi_{nz} = \Phi_{xz} \cos \hat{nx} + \Phi_{yz} \cos \hat{ny} + \Phi_{zz} \cos \hat{nz}
\end{aligned} \tag{3.13}$$

The nine components of the stress can be grouped inside the well known *stress tensor*:

$$\begin{vmatrix} \Phi xx & \Phi yx & \Phi zx \\ \Phi xy & \Phi yy & \Phi zy \\ \Phi xz & \Phi yz & \Phi zz \end{vmatrix} \tag{3.14}$$

Moreover, calculating the equilibrium of the rotation around the three principal axis, it is possible to find out the following relations:

$$\Phi_{xy} = \Phi_{yx}, \qquad \Phi_{xz} = \Phi_{zx}, \qquad \Phi_{yz} = \Phi_{zy} \tag{3.15}$$

;

this way the tensor (3.14) has just six independent components, as shown in Equation (3.16):

- three diagonal terms Φ_{ii} representing normal components that are usually called

$$\sigma_x, \qquad \sigma_y, \qquad \sigma_z$$

- three extra-diagonal symmetrical terms Φ_{ij} representing tangential components usually called respectively

$$\tau_x, \qquad \tau_y, \qquad \tau_z.$$

$$\begin{vmatrix} \sigma_x & \tau_z & \tau_y \\ \tau_z & \sigma_y & \tau_x \\ \tau_y & \tau_x & \sigma_z \end{vmatrix} \tag{3.16}$$

Types of Flow

Steady flow: is characterized by kinematic values which are not time-dependent; the velocity vector and all its three components u, v, z are then just function of the spatial coordinates, but not of time:

$$u = u(x,\ y,\ z) \qquad v = v(x,\ y,\ z) \qquad w = w(x,\ y,\ z)$$

Figure 3.4a is an example of a steady flow in nature: the flow of the river can be considered never-changing in time and each portion is uniquely defined by constant kinematic values.

Uniform flow: it is characterized by velocity values never-changing in space. An example is the steady laminar flow in a circular duct as shown in Figure 3.4b: assuming the flow as axis-symmetric, the velocity profile could be defined as function of the only parameter r

$$u = u(r)$$

and remains identical in each cross section.

Average steady and uniform flow in case we are considering turbulent flows, as it will be explained in Section 4, fluid motion can be expressed as superposition of a *motion of agitation* representative of turbulence's effects and the *main transport motion* which is the only responsible of the mass stream. A turbulent flow should be theoretically considered as unsteady because the turbulent motion of agitation is completely random and unpredictable; however, according to Reynolds theories (Section 4.3) it is still possible to refer to steady and uniform turbulent flow when it is so the main transport motion.

Figure 3.4c shows a turbulent flow downstream a cylinder at a Reynolds number of about 4: the flow separates in the downstream and the wake is formed by two symmetric eddies. The eddies remain steady and symmetrical but grow in size up to a Reynolds number of about 40 where Von Karman's instabilities start to appear.

Figure 3.4d is a scheme of a uniform turbulent flow inside a duct: once the flow is fully developed, similarly to the laminar case of Figure 3.4b, its average velocity profile does not vary anymore along x-axis.

3.2 Fluid Kinematics

3.2.1 Eulerian and Lagrangian Approach

It is possible to describe the dynamics of a fluid by following two different approaches: Lagrangian and Eulerian [15].

Lagrangian approach This is a way of looking at fluid motion where the observer focuses on an individual fluid particle while moving through space and time (Figure 3.5a). Within this specification of the flow field, all fluid particles are labeled by a time-independent vector field **a**. Often, **a** is chosen to be the position of the particles at some initial time t_0. Specifically, the flow velocity $\mathbf{v}(\mathbf{a}, t)$ is related to the position $\mathbf{x}(\mathbf{a}, t)$ of the fluid particles by the relation

$$\mathbf{v} = \frac{\partial \mathbf{x}}{\partial t}$$

.

Eulerian approach This is a way of looking at fluid motion that focuses on specific and fixed locations in the space –also called Control Volume (CV)– through which the fluid flows (Figure 3.5b). Within this specification of the flow field, quantities are expressed as a function of fixed position **x** and time t and specifically, the flow velocity is described as $\mathbf{v}(\mathbf{x}, t) = \mathbf{v}(x,\ y,\ z,\ t)$.

For an arbitrary property of the fluid ϕ, it is possible to derive the lagrangian equations from the eulerian ones –and viceversa– by using the following relationship:

$$\begin{aligned} \overbrace{\rho \frac{d\phi}{dt}}^{\text{for a MOVING PARTICLE}} &= \overbrace{\frac{\partial(\rho\phi)}{\partial t} + div(\rho\phi\mathbf{v})}^{\text{for a FIXED FLUID CONTROL VOLUME}} \\ &= \rho\Big(\frac{\partial \phi}{\partial t} + \mathbf{v} \cdot grad\phi\Big) + \underbrace{\phi\Big(\frac{\partial \rho}{\partial t} + div(\rho\mathbf{v})\Big)}_{\text{equal to zero because of continuity}} \\ &= \rho \frac{\partial \phi}{\partial t} + \mathbf{v} \cdot grad\phi \end{aligned} \tag{3.17}$$

which in the case of velocity becomes:

$$\begin{aligned}\frac{d\mathbf{v}}{dt} &= \overbrace{\frac{\partial \mathbf{v}}{\partial t}}^{\text{local rate of change}} + \overbrace{\left(\frac{\partial \mathbf{v}}{\partial x}\cdot\frac{\partial x}{\partial t}+\frac{\partial \mathbf{v}}{\partial y}\cdot\frac{\partial y}{\partial t}+\frac{\partial \mathbf{v}}{\partial z}\cdot\frac{\partial z}{\partial t}\right)}^{\text{convective rate of change}} \\ &= \frac{\partial \mathbf{v}}{\partial t}+\left(\frac{\partial \mathbf{v}}{\partial x}\cdot u+\frac{\partial \mathbf{v}}{\partial y}\cdot v+\frac{\partial \mathbf{v}}{\partial z}\cdot w\right) \\ &= \frac{\partial \mathbf{v}}{\partial t}+\mathbf{v}\cdot grad(\mathbf{v})\end{aligned} \tag{3.18}$$

Even if the Eulerian approach fits better the Computational Fluid Dynamics (CFD) purposes, experts agree that deriving the conservation equations in a Lagrangian form leads to easier solving algorithms; according to the relation (3.17) it is fortunately easy to convert equations from a form to the other.

3.2.2 Continuity Equation

In an Eulerian frame the mass balance guarantees that

> mass increasing rate inside the fluid element must be equal to the net mass flow rate into the element.

Referring to a control volume (CV) whose dimensions are $\delta x,\ \delta y,\ \delta z$ as shown in Figure 3.6, it is possible to express the following quantities:

Rate of increase in mass: $\frac{\partial \rho}{\partial t}\,\delta x\,\delta y\,\delta z\,dt$;

Net mass flow along x: $\left(\rho u+\frac{\partial(\rho u)}{\partial x}dx\right)dy\,dz-\left(\rho u\right)dy\,dz=\frac{\partial(\rho u)}{\partial x}\,dx\,dy\,dz\,dt$;

Net mass flow along y: $\left(\rho v+\frac{\partial(\rho v)}{\partial y}dy\right)dx\,dz-\left(\rho v\right)dx\,dz=\frac{\partial(\rho v)}{\partial y}\,dy\,dx\,dz\,dt$;

Net mass flow along z: $\left(\rho w+\frac{\partial(\rho w)}{\partial z}dz\right)dx\,dy-\left(\rho w\right)dx\,dy=\frac{\partial(\rho w)}{\partial z}\,dz\,dx\,dy\,dt$.

and finally write the equation of continuity in an Eulerian form as

$$\begin{aligned}\frac{\partial \rho}{\partial t}\delta x\,\delta y\,\delta z\,dt+\left(\frac{\partial(\rho u)}{\partial x}+\frac{\partial(\rho v)}{\partial y}+\frac{\partial(\rho w)}{\partial z}\right)dx\,dy\,dz\,dt&=0\\ \frac{\partial \rho}{\partial t}+div(\rho\mathbf{v})&=0\end{aligned} \tag{3.19}$$

By exploiting Equation (3.17) it is then possible to convert it into the equivalent Lagrangian form:

$$\frac{d\rho}{dt}+\rho\,div(\rho\,\mathbf{v})=0. \tag{3.20}$$

The two Equations (3.19),(3.20) must be respected in every single point of the fluids and for this reason they are also called *local continuity equations*.

(a) *Steady flow in a small river*

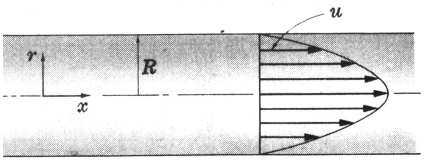

(b) *Uniform laminar flow inside a duct*

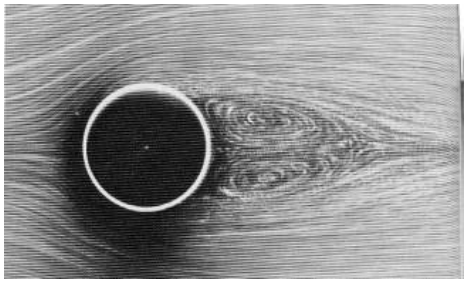

(c) *Steady turbulent flow downstream a cylinder*

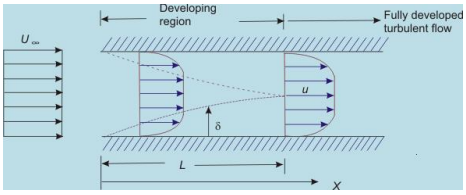

(d) *Uniform turbulent flow inside a duct*

Figure 3.4: *Different types of flow*

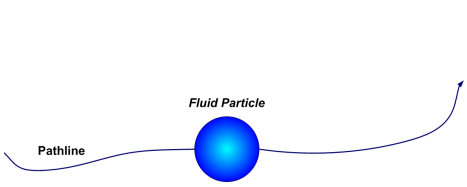

(a) *Lagrangian approach scheme*

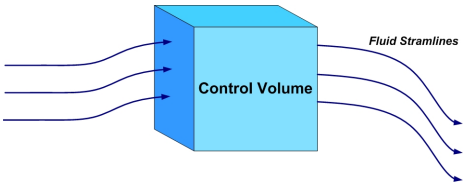

(b) *Eulerian approach scheme*

Figure 3.5: *Difference between Lagrangian and Eulerian approach*

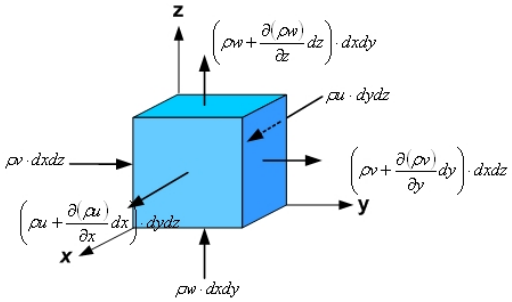

Figure 3.6: *Net mass flows in a generic Control Volume*

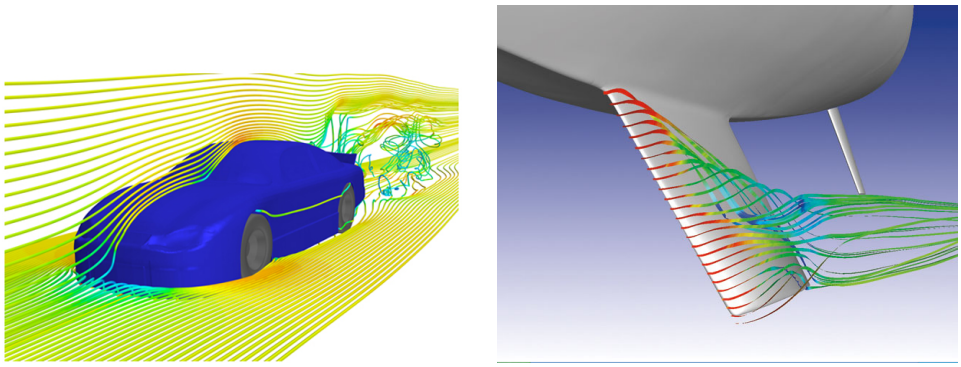

(a) *Example of stramlines around a Nascar car taken from www.cd-adapco.com*

(b) *Example of pathlines of water around a drift taken from www.fluent.com*

Figure 3.7: *Examples of Streamlines and Pathlines*

3.2.3 Fluid Motion

Once the flow field has been solved, there are many ways to represent it and to focus on different aspects characterizing it: two of the most effectve and mainly used are *streamlines* and *pathlines*.

Streamlines

In 2D flow fields it is possible to define a *stream function* Ψ so that the two following relations are satisfied:

$$u = \frac{\partial \Psi}{\partial y} \qquad v = -\frac{\partial \Psi}{\partial x} \tag{3.21}$$

Streamlines are then simply the isolines of the stream function Ψ and keep always tangent to the velocity vector $\mathbf{v}$.

This definition of streamlines contains precious informations on the mass flow rate as well: the distance between the values of two different streamlines is equal to the mass flow rate between the same streamlines. Thus when a pair of streamlines are closer to each other, this implies that the velocity is greater than when the same pair has wide spacing, since the same amount of mass must pass through the space between the lines: this is also the reason why when representing the stream function contours plot, it is expressed in (kg/s). An example is shown on Figure 3.7a

Pathlines

If we imagine to feed the domain with massless particles, pathlines are the trajectories left behind by these particles so that this way the flow field can be visualized. Pathlines depend on the location of the domain where particles are

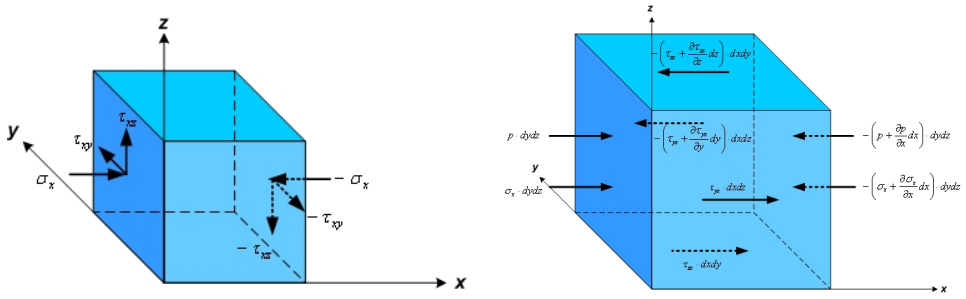

(a) *Viscous stresses acting on the faces perpendicular to x-axis of a fluid control volume*

(b) *Surface forces acting on a control volume along x-axis*

Figure 3.8: *Viscous stresses and Surface forces on a control volume*

injected and for unsteady flows also on the time when they are injected; while in steady conditions they are coincident with the streamlines. An example of pathlines is shown in Figure 3.7b.

3.3 Governing Equations of Fluid Dynamics

In order to explicitly solve the flow field, it is necessary to derive the conservation equations for momentum which are the ones responsible for the dynamics behavior of the fluid.

According to the first Newton's law, the following relation must be always respected for an infinitesimal control volume:

$$\begin{aligned} dm\ \mathbf{a} &= d\mathbf{R} \\ \rho\ dxdydz &= d\mathbf{R} \end{aligned} \tag{3.22}$$

where $d\mathbf{R}$ is the result of all the forces acting on the element that is generally split into:

- the *mass force* $\rho\mathbf{F}_{\text{mass}}\ dxdydz$, where $\mathbf{F}_{\text{mass}}$ is the specific force expressed as (N/kg). Tipical mass forces that can be considered are the gravity force, elecromagnetic force, centrifugal, Coriolis...

- the *surface force* transmitted to the element by the surface viscous stresses and the pressure. Figure 3.8a represents a scheme of the viscous stresses acting just on the faces perpendicular to x-axis; the rest of the faces withstand an equivalent situation. The marks of the stresses follow this rules: normal stresses are marked as σ_i, where i is the name of their direction axis; while tangential stresses are marked as τ_{ij}, where i is the name of the axis perpendicular to the face where they lay and j is their direction axis.

Referring to Figure 3.8b, the net surface force $F_{\text{surf},x}$ acting on the element along x-axis is given by:

$$F_{\text{surf},x}\, dxdydz = p\, dxdy - p\, dxdy - \frac{\partial p}{\partial x}\, dxdydz - \frac{\partial \sigma_x}{\partial x}\, dxdydz + \\ - \frac{\partial \tau_{yx}}{\partial y}\, dxdydz - \frac{\partial \tau_{zx}}{\partial z}\, dxdydz$$

$$F_{\text{surf},x}\, dxdydz = -\Big(\frac{\partial (p+\sigma_x)}{\partial x} + \frac{\partial \tau_{yx}}{\partial y} + \frac{\partial \tau_{zx}}{\partial z}\Big)\, dxdydz \tag{3.23}$$

Inserting these terms inside Equation (3.22) and considering that the components of the acceleration vector **a** are respectively du/dt, dv/dt, dw/dt, we obtain for the equilibrium along x-axis:

$$\begin{aligned} \rho\, dxdydz\, \frac{du}{dt} &= \rho\, F_{\text{mass},x}\, dxdydz + F_{\text{surf},x}\, dxdydz \\ \rho\, \frac{du}{dt} &= \rho\, F_{\text{mass},x} + F_{\text{surf},x} \\ \rho\left(F_{\text{mass},x} - \frac{du}{dt}\right) &= -F_{\text{surf},x} \\ \rho\left(F_{\text{mass},x} - \frac{du}{dt}\right) &= \frac{\partial (p+\sigma_x)}{\partial x} + \frac{\partial \tau_{yx}}{\partial y} + \frac{\partial \tau_{zx}}{\partial z} \end{aligned} \tag{3.24}$$

Similarly it is possible to derive the equations for the two other cardinal axis so that finally we obtain the following system of scalar equations:

$$\begin{aligned} &\text{x-axis:} \quad \rho\left(F_{\text{mass},x} - \frac{du}{dt}\right) = \frac{\partial (p+\sigma_x)}{\partial x} + \frac{\partial \tau_{yx}}{\partial y} + \frac{\partial \tau_{zx}}{\partial z} \\ &\text{y-axis:} \quad \rho\left(F_{\text{mass},y} - \frac{dv}{dt}\right) = \frac{\partial \tau_{xy}}{\partial x} + \frac{\partial (p+\sigma_y)}{\partial y} + \frac{\partial \tau_{zy}}{\partial z} \\ &\text{z-axis:} \quad \rho\left(F_{\text{mass},z} - \frac{dw}{dt}\right) = \frac{\partial \tau_{xz}}{\partial x} + \frac{\partial \tau_{yz}}{\partial y} + \frac{\partial (p+\sigma_z)}{\partial z} \end{aligned} \tag{3.25}$$

As shown by Equation (3.14) in Paragraph 3.1.1, the tensor of the stresses is symmetrical so that the Equations 3.25 can be simplified as:

$$\begin{aligned} &\text{x-axis:} \quad \rho\left(F_{\text{mass},x} - \frac{du}{dt}\right) = \frac{\partial (p+\sigma_x)}{\partial x} + \frac{\partial \tau_z}{\partial y} + \frac{\partial \tau_y}{\partial z} \\ &\text{y-axis:} \quad \rho\left(F_{\text{mass},y} - \frac{dv}{dt}\right) = \frac{\partial \tau_z}{\partial x} + \frac{\partial (p+\sigma_y)}{\partial y} + \frac{\partial \tau_x}{\partial z} \\ &\text{z-axis:} \quad \rho\left(F_{\text{mass},z} - \frac{dw}{dt}\right) = \frac{\partial \tau_y}{\partial x} + \frac{\partial \tau_x}{\partial y} + \frac{\partial (p+\sigma_z)}{\partial z} \end{aligned} \tag{3.26}$$

and rewritten as well in a vectorial form:

$$\rho\left(\mathbf{F}_{\text{mass}} - \frac{d\mathbf{v}}{dt}\right) = \frac{\partial \mathbf{\Phi_x}}{\partial x} + \frac{\partial \mathbf{\Phi_y}}{\partial y} + \frac{\partial \mathbf{\Phi_z}}{\partial z}$$

$$\rho\left(\mathbf{F}_{\text{mass}} - \frac{d\mathbf{v}}{dt}\right) = div\underline{\mathbf{\Phi}} \tag{3.27}$$

where $\mathbf{\Phi_i}$ is the generic stress vector acting on a plane normal to i-axis and $\underline{\mathbf{\Phi}}$ the stress tensor.

Summarizing, a generic process of fluid motion is explained by the following set of equations:

- CONSERVATION EQUATION FOR MOMENTUM which explains the dynamics of a fluid. It is summed up evenly by the vectorial Equation (3.27) or by the scalar Equations (3.26);
- CONTINUITY EQUATION, expression of the mass balance and represented by the scalar Equation (3.19);
- EQUATION OF STATE which expresses the link between density, temperature and stress field. If the fluid can be considered as incompressible this equation can be simplified to ρ = const while in the other case it is represented by the scalar Equation (3.6) for liquids and scalar Equation (3.7) for gases.

Finally, we obtain a system of 5 scalar equations in 10 unknown variables, function both of space and time:

$$\rho, \quad u, \quad v, \quad w, \quad \sigma_x, \quad \sigma_y, \quad \sigma_z, \quad \tau_x, \quad \tau_y, \quad \tau_z \, .$$

It is then evident that in order to solve the problem it is necessary to write five more equations in the same variables: these equations are written exploiting the link between stresses and deformation velocity –also called *rheological equation*– and lead to the Navier or Navier-Stokes Equations, as explained in the next Section 3.4.

3.4 Navier and Navier-Stokes Equations

In the previous Section 3.3, deriving Equation (3.25) the compression stresses acting on the fluid element have been expressed as $p + \sigma_i$ because the stress field can generally be considered as superposition between two main contributions as shown and explained below:

$$\underline{\mathbf{\Phi}} = \overbrace{\begin{vmatrix} p & 0 & 0 \\ 0 & p & 0 \\ 0 & 0 & p \end{vmatrix}}^{\text{Static part}} + \underbrace{\begin{vmatrix} \sigma_x & \tau_z & \tau_y \\ \tau_z & \sigma_y & \tau_x \\ \tau_y & \tau_x & \sigma_z \end{vmatrix}}_{\text{Deviator of stress tensor}}$$

Static part which is just formed by normal stresses due to the pressure p surrounding the fluid element. When a *perfect fluid* is considered, this is the only part taken into account.

Deviator of stress tensor which is tightly related to the dynamics and responsible for the different behavior of a real fluid compared to a perfect fluid. As already explained, the six components are the stresses generated in the fluid by the viscosity μ during the motion.

The key for the closure of the problem is then finding the relation between the six components of the deviator, the viscosity μ and the velocity components u, v, w which are themselves connected to the deformations occurring in the fluid.

3.4.1 Analysis of fluid deformations

The analysis of the link between velocity field and deformations is needed in order to express explicitly the terms of the deviator of the stress tensor.

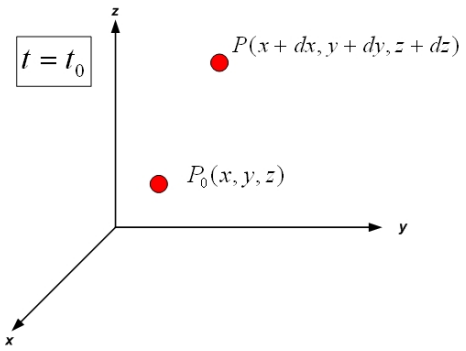

Figure 3.9: *Generic points in a deforming fluid*

As long as we are treating the fluid as a continuum (Section 3.1), referring to the situation shown in Figure 3.9 it is possible to express the velocity of the point P in a given instant t_0 as:

$$\mathbf{v} = \mathbf{v_0} + \left.\frac{\partial \mathbf{v}}{\partial x}\right|_{x,y,z,t_0} dx + \left.\frac{\partial \mathbf{v}}{\partial y}\right|_{x,y,z,t_0} dy + \left.\frac{\partial \mathbf{v}}{\partial z}\right|_{x,y,z,t_0} dz$$

or, in the equivalent vectorial form

$$\mathbf{v} = \mathbf{v_0} + d\mathbf{x} \cdot \underline{\mathbf{A}}$$

where

$$\underline{\mathbf{A}} = grad\mathbf{v} = \begin{vmatrix} \frac{\partial u}{\partial x} & \frac{\partial v}{\partial x} & \frac{\partial w}{\partial x} \\ \frac{\partial u}{\partial y} & \frac{\partial v}{\partial y} & \frac{\partial w}{\partial y} \\ \frac{\partial u}{\partial z} & \frac{\partial v}{\partial z} & \frac{\partial w}{\partial z} \end{vmatrix}$$

is a tensor representing the velocity gradient in a point; it can be rewritten as sum of two other tensors: a symmetrical one $\underline{\mathbf{D}}$ and an emi-symmetrical one $\underline{\mathbf{\Omega}}$ as follows:

$$\underline{\mathbf{A}} = \underbrace{\begin{vmatrix} \frac{\partial u}{\partial x} & \frac{1}{2}(\frac{\partial v}{\partial x} + \frac{\partial u}{\partial y}) & \frac{1}{2}(\frac{\partial w}{\partial x} + \frac{\partial u}{\partial z}) \\ \frac{1}{2}(\frac{\partial u}{\partial y} + \frac{\partial v}{\partial x}) & \frac{\partial v}{\partial y} & \frac{1}{2}(\frac{\partial w}{\partial y} + \frac{\partial v}{\partial z}) \\ \frac{1}{2}(\frac{\partial u}{\partial z} + \frac{\partial w}{\partial x}) & \frac{1}{2}(\frac{\partial w}{\partial y} + \frac{\partial v}{\partial z}) & \frac{\partial w}{\partial z} \end{vmatrix}}_{\underline{\mathbf{D}}} + \underbrace{\begin{vmatrix} 0 & \frac{1}{2}(\frac{\partial v}{\partial x} - \frac{\partial u}{\partial y}) & \frac{1}{2}(\frac{\partial w}{\partial x} - \frac{\partial u}{\partial z}) \\ \frac{1}{2}(\frac{\partial u}{\partial y} - \frac{\partial v}{\partial x}) & 0 & \frac{1}{2}(\frac{\partial w}{\partial y} - \frac{\partial v}{\partial z}) \\ \frac{1}{2}(\frac{\partial u}{\partial z} - \frac{\partial w}{\partial x}) & \frac{1}{2}(\frac{\partial w}{\partial y} - \frac{\partial v}{\partial z}) & 0 \end{vmatrix}}_{\underline{\mathbf{\Omega}}} \tag{3.28}$$

The two tensors have a specific physical meaning that worths to be explained:

Tensor of the deformation velocities $\underline{\mathbf{D}}$ In this case the diagonal and extra-diagonal components have two different meanings:

- the simultaneous action of the diagonal components D_{ii} causes an expansion of the volume of the fluid element without changing its shape; more precisely, the specific volume deformation velocity is equal to the trace of $\underline{\mathbf{D}}$

$$\frac{dV}{dt}\frac{1}{V} = \Big(\frac{\partial u}{\partial x} + \frac{\partial v}{\partial y} + \frac{\partial w}{\partial z}\Big) = div\mathbf{v} \tag{3.29}$$

  so that when the fluid is considered incompressible no change in volume occurs because in this case $div\mathbf{v} = 0$;

- the angular deformation rate $\dot{\gamma}_i$ of a fluid element is exactly the double of the extra-diagonal terms of tensor $\underline{\mathbf{D}}$, where the subscript of $\dot{\gamma}_i$ indicates the axis of rotation. For example, the deformation rate around z-axis can be written as

$$\dot{\gamma}_z = \Big(\frac{\partial u}{\partial y} + \frac{\partial v}{\partial x}\Big) \tag{3.30}$$

  ;

Tensor of rigid rotation $\underline{\mathbf{\Omega}}$ The non-zero components of this tensor represent the rigid rotation ω_i around the i-axis of the fluid element. For example, rotational speed around z-axis is

$$\omega_z = \frac{\partial v}{\partial x} = -\frac{\partial u}{\partial y} = \frac{1}{2}\Big(\frac{\partial v}{\partial x} - \frac{\partial u}{\partial y}\Big) \tag{3.31}$$

.

The main point of this analysis is that the tensor $\underline{\mathbf{D}}$ is the only one responsible for the fluid element deformations.

In order to explicit the expression of the tensor $\underline{\mathbf{\Phi}}$, it is necessary to introduce the hypothesis of a *stokesian fluid* which is a fluid characterized by the following properties:

– the tensor of the stresses $\underline{\mathbf{\Phi}}$ is a function of the only tensor $\underline{\mathbf{D}}$

$$\underline{\mathbf{\Phi}} = f(\underline{\mathbf{D}}) \tag{3.32}$$

;

– the following relation is valid for static conditions

$$\underline{\mathbf{\Phi}} = p\,\underline{\mathbf{I}} \tag{3.33}$$

;

– the fluid is *isotropic*, which means there are no preferential directions and the function f is independent from the reference system;

– the fluid is *homogeneous*, which means it is not direcly depending on the position $\mathbf{x}$, but on the variation of $\underline{\mathbf{D}}$ with the position.

Under this hypothesis and considering the fluid *newtonian* as well, which means the function f is linear, it is possible finally to explicit the tensor of the stresses as

$$\underline{\mathbf{\Phi}} = \begin{vmatrix} p & 0 & 0 \\ 0 & p & 0 \\ 0 & 0 & p \end{vmatrix} + \begin{vmatrix} \sigma_x & 0 & 0 \\ 0 & \sigma_y & 0 \\ 0 & 0 & \sigma_z \end{vmatrix} \tag{3.34}$$

and then relate it to the tensor $\underline{\mathbf{D}}$

$$\begin{array}{rcccl} \Phi_{xx} - p & = & \sigma_x & = & \mu_{xx}D_{xx} + \mu_{xy}D_{yy} + \mu_{xz}D_{zz} \\ \Phi_{yy} - p & = & \sigma_y & = & \mu_{yx}D_{xx} + \mu_{yy}D_{yy} + \mu_{yz}D_{yz} \\ \Phi_{zz} - p & = & \sigma_z & = & \mu_{zx}D_{xx} + \mu_{zy}D_{yy} + \mu_{xz}D_{zz} \end{array} \tag{3.35}$$

where μ_{ij} are the linear coefficients which still are not known.

Moreover it is possible to demonstrate that the coefficients μ_{ii} are all negative and do not differ all from each others but they can be conventionally expressed as

$$\begin{array}{rcl} \mu_{ii} & = & -\mu' - 2\mu \\ \mu_{ij} & = & -\mu' \end{array} \tag{3.36}$$

which, once substituted inside Equations 3.35, lead to the following expression of the stress tensor

$$\underline{\mathbf{\Phi}} = \left(p - \mu' div\mathbf{v}\right)\underline{\mathbf{I}} - 2\mu\underline{\mathbf{D}} \tag{3.37}$$

which is also called *rheological equation*.

The physical meaning of μ and μ' is explained below analyzing the previous Equation (3.37):

- μ' multiplies $div\mathbf{v}$, which is directly linked to the volume variation as explained before in this Section. Under hypothesis of stokesian fluid, it assumes also the value
$$\mu' = -\frac{2}{3}\mu$$
- μ is directly linked to $\underline{\mathbf{D}}$ and it is possible to write
$$\Phi_{xz} = \tau_y = -2\mu D_{xz} = -2\mu\frac{1}{2}\Big(\frac{\partial u}{\partial z} + \frac{\partial w}{\partial x}\Big) = \mu\frac{\partial \gamma_y}{\partial t};$$
it is then the coefficient which links tangential stresses to angular deformations.

Considering this, it is finally possible to rewrite the rheological Equation 3.37 as

$$\underline{\mathbf{\Phi}} = \Big(p - \frac{2}{3}\mu\, div\mathbf{v}\Big)\underline{\mathbf{I}} - 2\mu\underline{\mathbf{D}} \tag{3.38}$$

which is the required explicit expression of the stress tensor.

3.4.2 Navier Equations

It is now possible to substitute the rheological equation (3.38) inside the conservation equation for momentum (3.27) obtaining

$$\rho\left(\mathbf{F}_{\text{mass}} - \frac{d\mathbf{v}}{dt}\right) = div\Big[\Big(p - \frac{2}{3}\mu\, div\mathbf{v}\Big)\underline{\mathbf{I}} - 2\mu\underline{\mathbf{D}}\Big] \tag{3.39}$$

;

furthermore, the previous Equation (3.39) can be simplified considering that

$$\begin{aligned} &div[p\ \underline{\mathbf{I}}] = grad\ p \\ &div\Big[\frac{2}{3}\mu\ div\mathbf{v}\ \underline{\mathbf{I}}\Big] = \frac{2}{3}\mu\ grad(div\mathbf{v}) \\ &div\Big[-2\mu\ \underline{\mathbf{D}}\Big] = -\mu\ grad(div\mathbf{v}) - \mu\nabla^2\mathbf{v} \end{aligned} \tag{3.40}$$

These considerations finally lead to the simplified Equation (3.41):

$$\rho\left(\mathbf{F}_{\text{mass}} - \frac{d\mathbf{v}}{dt}\right) = grad\ p - \frac{1}{3}\mu\ grad(div\mathbf{v}) - \mu\nabla^2\mathbf{v} \tag{3.41}$$

Adding to the last one also the equation of continuity (3.19) and the equation of state (3.2) plus *boundary conditions (BC)* and *initial conditions (IC)* , it is finally

possible to complete the following fully determined system

$$\begin{cases} \rho\left(\mathbf{F}_{\text{mass}} - \frac{d\mathbf{v}}{dt}\right) = grad\ p - \frac{1}{3}\mu\ grad(div\mathbf{v}) - \mu\nabla^2\mathbf{v} \\ \frac{\partial\rho}{\partial t} + div(\rho\mathbf{v}) = 0 \\ \rho = \rho(p,T) \\ \text{Boundary Conditions (BC)} \\ \text{Initial Conditions (IC)} \end{cases} \tag{3.42}$$

better known as *Navier Equations*.

3.4.3 Navier-Stokes Equations

The Navier equations (3.42) become simpler if the studied fluid can be considered incompressible; in this case the equation of continuity gives $div\mathbf{v} = 0$ and so the system of equations is simplified as follows

$$\begin{cases} \rho\left(\mathbf{F}_{\text{mass}} - \frac{d\mathbf{v}}{dt}\right) = grad\ p - \mu\nabla^2\mathbf{v} \\ div(\rho\mathbf{v}) = 0 \\ \rho = \rho(p,T) = \text{const} \\ \text{Boundary Conditions (BC)} \\ \text{Initial Conditions (IC)} \end{cases} \tag{3.43}$$

well known as *Navier-Sokes Equations*.

Chapter 4

Turbulence

«When I meet God, I am going to ask him two questions: Why relativity? And why turbulence? I really believe he will have an answer for the first»

Werner Eisenberg

Figure 4.1: *Picture from NASA Langley Research Center.*

Turbulence is a ubiquitous phenomenon in environmental fluid mechanics characterized by chaotic and stochastic property changes that dramatically affect flow structure and mixing. Thus, it is very important to form both a conceptual understanding and a quantitative description of turbulent flows.

It is shown by experience that turbulent phenomena occur in a specific fluid flow when the velocity exceed a certain value dependent on the flow type. The first systematic studies on turbulence were carried out by Osborne Reynolds in 1880s: he related the transition from laminar to turbulent flow to the well known dimensionless number –later named after him *Reynolds number Re* – which is the expression of the ratio between the inertial forces $\rho\, v^2$ and the viscous forces $\frac{\mu v}{L}$:

$$Re = \frac{\rho\, v^2}{\frac{\mu v}{L}} = \frac{\rho\, v\, L}{\mu} = \frac{v\, L}{\nu} \tag{4.1}$$

Laminar flow occurs at low Reynolds numbers, where viscous forces are dominant, and is characterized by smooth and constant fluid motion; while turbulent flow occurs at high Reynolds numbers and is dominated by inertial forces, which tend to produce random eddies, vortexes and other flow instabilities.

The main characteristics of a turbulent flow are listed below:

- *High Reynolds number*: all the turbulent flows are primarily characterized by high values of Reynolds number which can be physically traduced in a prevalence of the inertia forces acting inside the flow;

- *Randomness*: all the turbulent flows are dominated by chaos, irregularities and unpredictability;

- *Non-linearity and instability*: turbulent fields are highly non-linear. In unstable non-linear flows small perturbations grow spontaneously and frequently equilibrate as finite amplitude disturbances; anyway, further exceeding the stability criteria, the new state can become unstable to more complicated disturbances, and the flow eventually reaches a chaotic state. Moreover, the non-linearity of a turbulent flow results in vortex stretching, a key process by which turbulent flows maintain their vorticity [16].

- *Diffusivity*: rapid rate of diffusion of momentum and heat are due to the macroscopic mixing of fluid particles.

- *Vorticity*: turbulent flows are *rotational* which means that have non-zero vorticity; vortexes and rotating structures are noticeable inside the flow and are called usually *eddies*. Mechanism such as vortex formation, 3D stretching and coalescence are crucial in turbulence.

- *Dissipation*: the vortex stretching mechanism transfers energy and vorticity to increasingly smaller scales, until it becomes so small to be smeared out by viscosity dissipation; this process is well explained in Section 4.1.

4.1 Richardson's energy cascade

> «Big whirls have little whirls which feed on their velocity, and little whirls have lesser whirls and so on to viscosity in the molecular sense »
>
> *Lewis Fry Richardson*

As stated before, the presence of vorticity inside turbulence implies the presence of whirling structures called *eddies* concentrated along vortex lines or bundles. Referring to Figure 4.2a, the Richardson's theory of the energy cascade states that energy is transferred from large eddies progressively to smaller ones until the viscous effects become dominant and the energy is dissipated as heat [16].

Figure 4.2b shows the different phases of the *vortex stretching* phenomena: as the ending point of a vortex move randomly apart, the vortex line increases in length and decreases in diameter (i.e. stretches) while vorticity increases also because angular momentum is nearly conserved; then (from t_3 on) new smaller vortexes create from these lateral appendixes and so on with this energetic cascade. Normally energy transfer takes place from bigger vortexes to smaller, but it is sometimes possible that smaller eddies interact together, summing up energy and joining in larger ones: this process is called *backscatter* [17].

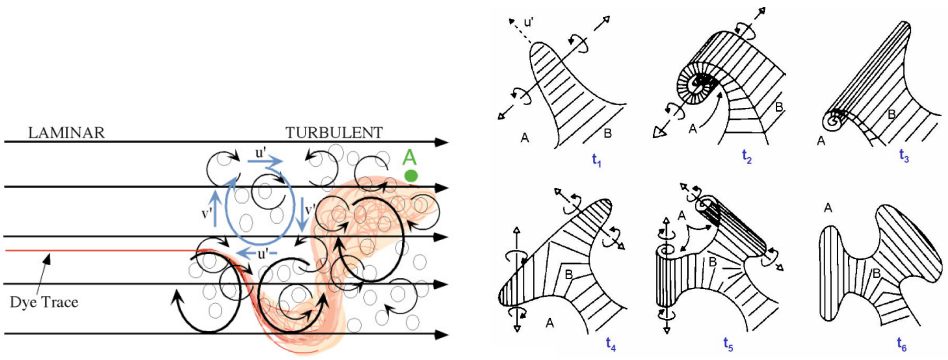

(a) *Turbulence scheme (www.dspace.mit.edu).* **(b)** *Vortex stretching process [17].*

Figure 4.2: *Whirling structures in turbulence.*

4.1.1 The integral scale

It is usual to refer to the eddies as entities localized over a region of size l, with a velocity $u(l)$ and a characteristic timescale $\tau(l) \equiv l/u(l)$. In the case of the larger eddies, the characteristic length-scale is l_0 and it is of the same order of magnitude of the flow length-scale L while the characteristic velocity is proportional to the root mean square of the turbulent intensity. As the Reynolds number of this edges $Re_0 = u_0 l_0/\nu$ is relatively high (the same order of magnitude as Re) the viscous effect are negligible.

The idea of Richardson was that the energy cascade goes on toward smaller and smaller eddies until the characteristic Reynolds number $Re(l) = u(l)l/\nu$ is sufficiently small that the eddy keeps stable and the effects of viscosity become dominant dissipating the kinetic energy into heat [17].

The process of energy transfer is essentially inviscid as the phenomena of vortex stretching is independent from non-linearities contained in the equations of motion. Therefore, in fully turbulent shear flow (i.e. for large Reynolds numbers) the viscosity of the fluid does not affect the shear production, while it determines directly the scales at which turbulent energy is dissipated into heat [16]. As the energy contained in these vortexes is proportional to u_0^2, then the *energy dissipation rate*, usually called $\varepsilon[m^2 s^3]$, must then be in the order of:

$$\varepsilon \sim \frac{u_0^2}{\tau_0} = \frac{u_0^3}{l} \tag{4.2}$$

which underlines the relation between ε and l.

By means of a dimensional analysis based on the following assumptions

- velocity and time scale for an eddy within the integral scale are respectively u_0 and τ_0;
- the characteristic velocity u_0 is in the order of the r.m.s. turbulent intensity $u' = (2 \cdot k/3)^{1/2}$;
- the energy of a eddy with a characteristic velocity u_0 is dissipated in a time τ_0;

it is possible to derive an estimation of the integral scale:

$$l_0 \propto \frac{k^{3/2}}{\varepsilon} \tag{4.3}$$

where the proportionality constant is close to one and $k[m^2/s^2]$ is the *turbulent kinetic energy* . Moreover, the Reynolds number associated to this scale can be written as

$$Re_0 = \frac{k^{1/2} \cdot l_0}{\nu} = \frac{k^2}{\varepsilon \cdot \nu} \tag{4.4}$$

Anyway, this is not enough to explain the dissipating process and point out its characteristic scales; an invaluable support to the theory of turbulence was given by Kolmogorov which under specific hypothesis proposed a dimensional analysis giving the birth to the well known Kolmogorov's theory.

4.2 The Kolmogorov's Theory

As stated in the previous section, Kolmogorov proposed an analytical expression of the Richardson's theory giving actually one of the most important contribution to the turbulence theory. The mentioned studies are based on three different hypothesis which are listed below.

4.2.1 First hypothesis: local anisotropy

The first postulate is that for very high Reynolds number, the small scale turbulent motions are statistically isotropic which means that there is no preferential spatial direction

$$\overline{u'^2} = \overline{v'^2} = \overline{w'^2}$$

while the characteristics of the flow in the order of the integral scale l_0 are not generally isotropic, since they are determined by the particular geometrical features of the boundaries. Kolmogorov supposed that since the energy cascade focuses more and more on the small scales, the geometrical and directional informations are progressively lost, so that the statistics of the small scales gains a universal character: for sufficiently high Reynolds numbers they are the same for all turbulent flows.

The largest length scale which marks the passage from the large anisotropic eddies (l_0) and the small scale isotropic eddies is called l_{EI} and for many high Reynolds number flows it can be estimated as [17]

$$l_{EI} = l_0/6 \tag{4.5}$$

4.2.2 Second hypothesis: the first similarity

Thus Kolmogorov argued that the directional information is not the only one getting lost in the microscale but all the statistics regarding the small-scale motions are universal for a high Reynolds number flows and moreover are uniquely determined by two quantities: the turbulent dissipation rate ε and the kinematic viscosity ν. By means of a dimensional analysis it is then possible to find out a characteristic length scale η , a velocity scale u_η, a time scale τ_η and Reynolds

number as functions of the previous quantities:

$$\begin{aligned} \eta &= \left(\frac{\nu^3}{\varepsilon}\right)^{1/4} \\ u_\eta &= \left(\varepsilon \cdot \nu\right)^{1/4} \\ \tau_\eta &= \left(\frac{\nu}{\varepsilon}\right)^{1/2} \\ Re_\eta &= \frac{\eta \cdot u_\eta}{\nu} = 1 \end{aligned} \tag{4.6}$$

Note that the fact that Re_η is 1 is consistent with the previously done hypothesis which says that the energy cascade goes on until the vortex's specific Re reaches a small enough value, which means that viscous dissipation is dominant.

The size range $l < l_{EI}$ is also called *universal equilibrium range* and within this range the characteristic time scale $l/u(l)$ is small compared to the flow characteristic one l_0/u_0, which means that the small eddies can adapt quicker to the energy transfers coming from the larger ones.

4.2.3 Third hypothesis: the second similarity

Using the relation $l_0 \sim k^{3/2}/\varepsilon$ presented in Section 4.1.1 and substituting it in Equations (4.6), it is possible to define the ratio between the small scale and the large scale eddies:

$$\begin{aligned} \eta/l_0 &\sim Re_L^{-3/4} \\ u_\eta/u_0 &\sim Re_L^{-1/4} \\ \tau_\eta/\tau_0 &\sim Re_L^{-1/2} \end{aligned} \tag{4.7}$$

As expected, if Re_L increases, small eddies time and velocity scales become little compared to the ones of the big eddies; η/l_0 progressively decreases as well, but there will be a range of scale l which will be small compared to l_0 and big compared to η. As a consequence, this intermediate scales will be characterized by relatively high Re_l and they will be not much affected by viscosity ν. Based on this considerations, Kolmogorov hypothesized that in every sufficiently high Reynolds number flows, the statistics of the motions of scale l in the range $l_0 \ll l \ll \eta$ have a universal form that is uniquely determined by ε and independent from ν. A new length scale l_{DI} is introduced which splits the universal equilibrium range into two subranges:

- *inertial subrange* ($l_{\mathrm{DI}} < l < l_{\mathrm{EI}}$) typical of the intermediate scales where viscous effects are negligible;
- *dissipation range* ($l < l_{DI}$) where viscous effects and dissipation are dominant.

It is possible to estimate $l_{DI} \approx 60\eta$ for most of the turbulent flow.

Considering now eddies in the inertial subrange of size l, using the definition of ε given in Equation 4.2

$$\varepsilon = \frac{u_\eta^3}{\eta} = \frac{\eta^2}{\tau_\eta^3} \tag{4.8}$$

and the relationships given in Equation (4.7), it is possible to derive velocity and time scales within this range as

$$\begin{aligned} u(l) &= (\varepsilon\, l)^{1/3} = u_\eta (l/\eta)^{1/3} \sim u_0 (l/l_0)^{1/3} \\ \tau(l) &= (l^2/\varepsilon)^{1/3} = \tau_\eta (l/\eta)^{2/3} \sim \tau_0 (l/l_0)^{2/3} \end{aligned} \tag{4.9}$$

The velocity scales and time scales $u(l)$ and $\tau(l)$ decrease as l decreases [17] in the inertial subrange, as a consequence of the second similarity hypothesis.

Taylor microscale

It is common to refer to the characteristic length-scale within the inertial subrange λ as Taylor microscale, which is defined as follows

$$\lambda \simeq \left(\frac{10\,\nu\,k}{\varepsilon}\right)^{1/2} \tag{4.10}$$

Comparing it respectively to Kolmogorov's length-scale η and the integral length-scale l_0, it is possible to notice that it falls exactly between the small scale eddies and the large scale eddies:

$$\begin{aligned} \lambda/l_0 &= \sqrt{10}\, Re_L^{-1/2} < 1 \\ \lambda/\eta &= \sqrt{10}\, Re_L^{1/4} > 1 \end{aligned} \tag{4.11}$$

Moreover, a commonly used quantity in the characterization of turbulence is the Taylor-scale Reynolds number Re_λ , which is related to the flow Re by the relation

$$Re_\lambda = \left(\frac{20}{3} Re_L\right)^{1/2} \tag{4.12}$$

Figure 4.3a summarizes the subdivision of the spatial ranges and their corresponding length-scale, each one characterized by specific velocity-scale and time-scale, as previously explained.

4.2.4 Wavenumber and energy spectrum

The final purpose of Kolmogorov's analysis is to find out the energy distribution among the previous presented ranges. It is possible to define a wavenumber

$$\kappa = 2\pi/l \tag{4.13}$$

and relate the previous ranges to it. Figure 4.3b shows how the turbulence ranges as a function of κ and its relative dimensionless group obtained multiplying it by the Kolmogorov length scale η.

The *energy spectrum* $E(\kappa)$ represents the energy contained in eddies of size l (and so wavenumber $\kappa = 2\pi/l$); by definition, the turbulent energy contained in eddies with wavenumber between κ_A and κ_B is expressed as

$$k = \int_{\kappa_A}^{\kappa_B} E(\kappa) d\kappa$$

According to the second similarity hypothesis (Section 4.2.2), $E(\kappa)$ will solely depend on κ and ε; by means of a dimension analysis, it is possible to obtain an expression of $E(\kappa)$ within the inertial subrange:

$$E(\kappa) = C\varepsilon^{2/3}\ \kappa^{-5/3} \tag{4.14}$$

where C is the universal Kolmogorov constant experimentally determined to be $C = 1.5$; this expression is also well known as the *Kolmogorov -5/3 spectrum*.

Further empirical model equations for $E(\kappa)$ in the production range (f_L) and dissipation range (f_η) have been added to this expression so that the complete expression for the spectrum is:

$$E(\kappa) = C\ \varepsilon^{2/3}\ \kappa^{-5/3}\ f_L\ f_\eta \tag{4.15}$$

For given values of ε, ν and k the full spectrum can finally be calculated basing on Equation 4.15; however, it is common to normalize the spectrum based on the Kolmogorov scales so that it results a function of the only variable R_λ instead of having three adjustable parameters (ε, ν, k). Figure 4.4a is a scheme of the normalized energy spectrum while Figure 4.4b shows how spectrum changes when Re_λ varies. With a deeper mathematical analysis, it is possible to derive which length scales contain most of the turbulent kinetic energy in the flow: the conclusion is that most of the energy (80%) is contained in eddies of length scale $l_{EI} = l_0/6 < l < 6l_0$.

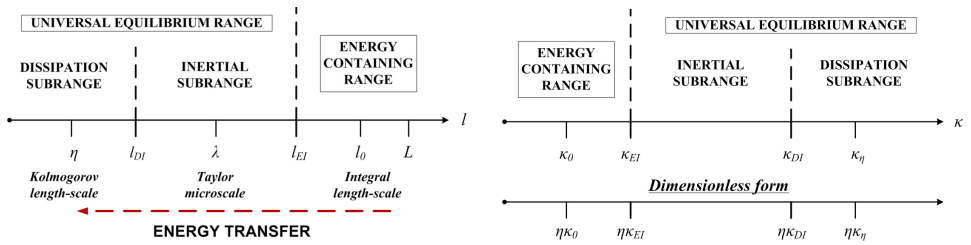

(a) *Turbulence ranges as function of length-scale* **(b)** *Turbulence ranges as function of wavenumber*

Figure 4.3: *Turbulence ranges as function of length-scale **(a)** and wavenumber **(b)** [17].*

Once that the energy content of the eddies has been studied, the unique unsolved question is to exactly point out which eddies dissipate the energy. Similarly, this question can be answered by constructing a dissipation rate spectrum $D(\kappa)$: the integral of $D(\kappa)$ over the full wavelength range is by definition the energy dissipation rate ε

$$\varepsilon = \int_0^\infty D(\kappa) d\kappa \tag{4.16}$$

Furthermore, considering that ε is defined as the multiple of the kinematic viscosity and squared velocity gradients (of order $\nu(du/dx)^2 \approx \nu k/l^2 \approx \nu k\kappa^2 \approx \nu\kappa^2 E(\kappa)$), we can then deduce:

$$D(\kappa) = 2\nu\ \kappa^2\ E(\kappa) \tag{4.17}$$

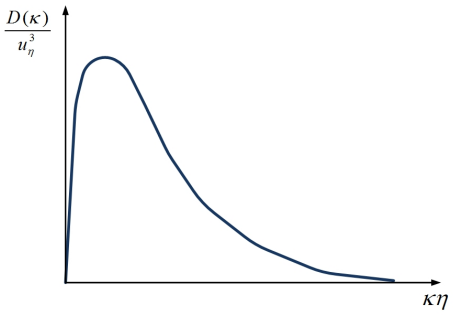

Figure 4.5: *Dissipation normalized spectrum*

Since the unit of $D(\kappa)$ is (m^3/s^3), it can thus be normalized with a velocity scale cubed (typically the Kolmogorov velocity scale), so that, as the normalized $E(\kappa)$, it is only dependent on R_λ, as shown in Figure 4.5. The dissipation rate spectrum can be integrated to show that most of the dissipation (90%) occurs in eddies of length scales $l_{DI}/\eta = 60 > l/\eta > 8$: this means that most of the dissipation occurs at scales that are larger than the Kolmogorov length scale η; so the Kolmogorov length scale should be interpreted as a measure of the smallest eddies that are present in a turbulent flow at high Reynolds numbers.

The spectra can be further analyzed to show that eddies spend about 90% of their total lifetime $\tau = k/\varepsilon$ in the production range, and that once eddies enter

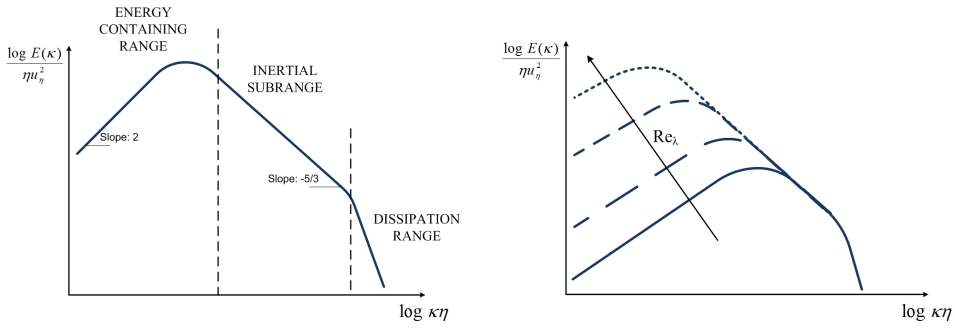

(a) *Normalized energy spectrum* **(b)** *Influence of* Re_λ

Figure 4.4: *Kolmogorov energy spectrum*

the inertial subrange it takes only about $\tau/10$ before the energy is dissipated. This time $\tau/10$ is also referred to as the *cascade time scale* [17].

4.2.5 Validity of Kolmogorov's theory

Kolmogorov's theory is an asymptotic theory: it has been shown to work well in the limit of very high Reynolds numbers: the exact shape of the normalized spectra may deviate from Kolmogorov's model spectra for intermediate Reynolds numbers. For instance, in many laboratory scale flows which have Reynolds numbers on the order of 10000 with $Re_\lambda \approx 250$, the exponent of $E(\kappa)$ in the inertial subrange is often measured to be $-3/2$ instead of the famous $-5/3$. Besides, the theory assumes that turbulence at high Reynolds numbers is completely random; in practice, large scale coherent structures may form as well.

Moreover, Kolmogorov's theory assumes that the energy cascade is one way: from large eddies to small eddies. Experimental studies have shown that even if the dominant energy transfer is indeed from large to small eddies, energy is also transferred, at a much lower rates, from smaller scales to larger scales in a process called backscatter, as mentioned in Section 4.1.

Research on the fundamental aspects of turbulence continues as the theory needs to be refined; both experimental and numerical simulations by means of large computer using Direct Numerical Simulation (DNS) are continuously carried out.

4.3 Reynolds Averaged Navier-Stokes Equations (RANS)

4.3.1 Overview

Navier-Stokes Equations 3.43 derived in Section 3.4 have no analytical solution except for some simple problems involving simple geometries. As it will be presented in Section 5, Computational Fluid Dynamics (CFD) developed numerical methods in order to solve numerically fluid-dynamics problems in a discrete domain.

There is no theoretical analytical difference between laminar and turbulent flow since Navier-Stokes Equations are valid for any flow regime, but turbulent flows have some peculiarities which cannot be neglected in a numerical analysis:

- **Irregularity**: by definition turbulent flow is a chaotic and irregular physical phenomenon. It is therefore necessary an enough fine mesh able to solve the flow field properly, up to the smallest significant spatial scales which are in the order of η according to the Kolmogorov's theory presented in Section 4.2.

Being L the characteristic dimension of the analyzed system, the number of mesh elements needed along a spatial direction is

$$N_{\text{elem,x}} = \frac{L}{\eta} \propto Re^{3/4}$$

and so the total number in a three-dimensional grid should be

$$N_{\text{elem,tot}} \propto Re^{9/4}$$

- **Unsteadiness**: turbulence is never a steady process, so it always requires an unsteady solution.
- **Three-dimensional**: as it is an ubiquitous phenomenon, a three-dimensional analysis must be always performed.

The numerical solution of a turbulent flow by means of direct Navier-Stokes equations is therefore extremely costly in terms of computational effort; a simplification is needed in order to make it feasible.

4.3.2 Reynolds decomposition and averaging

A turbulent flow instantaneously satisfies the Navier-Stokes equations. However, it is virtually impossible to predict the flow in detail, as there is an enormous range of scales to be resolved, the smallest spatial scales being less than millimeters and the smallest time scales being milliseconds. Even the most powerful computer nowadays would take an enormous amount of computing time to predict the details of an ordinary turbulent flow, resolving all the involved fine scales. Fortunately, we are generally interested in finding only the gross characteristics in such a flow, such as the distributions of mean velocity and temperature [16].

Reynolds derived the equations of motion for the mean state in a turbulent flow and examined what effect the turbulent fluctuations may have on the mean flow. His fundamental idea is based on *Reynolds decomposition*: each variable, such as velocity $\mathbf{v}$, is separated into the mean (time-averaged) component $\mathbf{v}_{\text{m}}$ and the fluctuating turbulent component $\mathbf{v}'$:

$$\mathbf{v}(\mathbf{x}, t) = \mathbf{v}_{\text{m}}(\mathbf{x}) + \mathbf{v}'(\mathbf{x}, t)$$

where $\mathbf{x}$ is the position vector, the subscript "m" indicates the mean time-averaged component and the superscript "′" indicates the turbulent fluctuating component [18].

The true time average $\bar{\mathbf{a}}$ of a variable $\mathbf{a}$ is defined by

$$\bar{\mathbf{a}} = \frac{1}{T} \int_0^T \mathbf{a}\, dt \tag{4.18}$$

By applying Reynolds decomposition to the terms in the Navier-Stokes equations and subsequently time averaging, it is therefore possible to simplify them.

The averaging process is straightforward in case of linear terms; for instance, in case of the pressure term, it gives

$$\bar{\mathbf{p}} = \frac{1}{T}\int_0^T (\mathbf{p}_\mathrm{m} + \mathbf{p}')dt = \mathbf{p}_\mathrm{m}$$

since the time average of any fluctuating random components is zero.

While non-linear terms generate new contributions containing the fluctuating components; for instance, in case of a general convective term Reynods averaging gives:

$$\overline{\left(v\frac{\partial u}{\partial y}\right)} = \overline{\left((v_\mathrm{m}+v')\frac{\partial(u_\mathrm{m}+u')}{\partial y}\right)} = u_\mathrm{m}\frac{\partial u_\mathrm{m}}{\partial y} + v'\frac{\partial u'}{\partial y} = u_\mathrm{m}\frac{\partial u_\mathrm{m}}{\partial y} + \left(\frac{\partial(u'\,v')_\mathrm{m}}{\partial y}\right) - \left(v'\frac{\partial u'}{\partial y}\right)_\mathrm{m}$$

The application of Reynolds averaging process to all the terms in Navier-Stokes equations leads finally to the Raynolds Averaged Navier-Stokes (RANS) equations, which give approximated averaged solutions to Navier-Stokes equations:

$$\begin{cases} \rho\left(\mathbf{F}_{\mathrm{mass,m}} - \frac{d\mathbf{v}_\mathrm{m}}{dt}\right) = grad\ p_\mathrm{m} - \mu\nabla^2\mathbf{v}_\mathrm{m} + \rho\ \nabla\cdot\underline{\mathbf{\Phi}}_{Re} \\ div(\rho\mathbf{v}_\mathrm{m}) = 0 \\ \rho = \rho(p,T) = \mathrm{const} \\ \text{Boundary Conditions (BC)} \\ \text{Initial Conditions (IC)} \end{cases} \tag{4.19}$$

This new system of equations is similar to the Navier-Stokes one, with the addition of a new symmetrical tensor $\underline{\mathbf{\Phi}}_\mathrm{Re}$ called *Reynolds stress tensor*

$$\underline{\mathbf{\Phi}}_\mathrm{Re} = \begin{vmatrix} (u'u')_\mathrm{m} & (u'v')_\mathrm{m} & (u'w')_\mathrm{m} \\ (v'u')_\mathrm{m} & (v'v')_\mathrm{m} & (v'w')_\mathrm{m} \\ (w'u')_\mathrm{m} & (w'v')_\mathrm{m} & (w'w')_\mathrm{m} \end{vmatrix} \tag{4.20}$$

which collects all the non-linear fluctuating components originated during Reynolds averaging process.

The advantages of RANS equations compared to Navier-Stokes are the followings:

- Possible spatial and temporal regularities;
- Possible stationarity;
- Possible symmetries in the flow field which allow to simplify the problem from 3D to 2D or eventually 1D;
- Coarser mesh dimension;

- Numerical solutions are possible exploiting the same numerical techniques used for Navier-Stokes equations and the computational effort is much more acceptable.

4.4 Closure Models for Turbulence

Since its 6 components are unknown, symmetrical tensor $\underline{\mathbf{\Phi}}_{\mathrm{Re}}$ in Equation 4.19 results completely undefined and so do the system of equations which is now formed by 4 scalar equations in 10 unknown variables u_{m}, v_{m}, w_{m}, p_{m}, $(u'u')_{\mathrm{m}}$, $(u'v')_{\mathrm{m}}$, $(u'w')_{\mathrm{m}}$, $(v'v')_{\mathrm{m}}$, $(v'w')_{\mathrm{m}}$, $(w'w')_{\mathrm{m}}$.

In order to close the system it is therefore necessary a closure model, function of the averaged flow field and able to derive the 6 new unknown variables:

$$\underline{\mathbf{\Phi}}_{\mathrm{Re}} = f(u_{\mathrm{m}}, v_{\mathrm{m}}, w_{\mathrm{m}}, p_{\mathrm{m}})$$

where f will be an approximated relation based on physical assumptions and experimental approach.

A lot of turbulence models have been developed in order to close the problem and make finally possible numerical solutions. These models are generally divided into four main categories according to the number of differential equations added to the RANS equations in order to derive the 6 unknown components [17]:

- Zero equation models: these models add no equation and express the 6 Reynolds turbulent stresses with constants derived by experimental analysis and physical assumptions; the most famous is the *mixing length model* developed by Prandtl: the model is extremely simple, with basically no addiction of computational effort, although it results in a very poor accuracy in describing turbulent quantities. Since much better models exist, it is almost never used and gives good predictions just for very simple 2-D flows where experimental correlations for the mixing length exist, such as flow in a cylindrical pipe or channel.

- One equation models: for the turbulent viscosity they solve just a single conservation equation containing convective and diffusive transport terms, as well as expressions for the production and dissipation of ν_t. It was firstly developed for use in unstructured codes in the aerospace industry and results economical and accurate for attached wall-bounded flows and flows with mild separation and recirculation.

- Two equations models: these models are for sure the most spread used since they give the best compromise between accuracy and precision .The most famous is the $k-\varepsilon$ model which will be explained in following Section 4.4.2.

- Reynolds Stress Model (RSM): this is the most accurate, complete and time consuming method since it solves additional transport equations for the six independent Reynolds stresses; these transport equations are derived by Reynolds averaging the product of the momentum equations with a fluctuating property. RSM is good for accurately predicting complex flows involving high streamline curvature, swirl, rotation and high strain rates.

4.4.1 The Bussinesq hypothesis

Basically all the two equation models are based on the hypothesis introduced by Bussinesq who proposed, in 1877, that the Reynolds stresses could be linked to the fluid mean rate of deformation, similarly to what happens for the viscous stresses.

$$\text{Viscous stresses:} \quad \tau_{ij} = \mu\left(\frac{\partial v_i}{\partial x_j} + \frac{\partial v_j}{\partial x_i}\right)$$

$$\text{Reynolds stresses:} \quad \tau_{\mathrm{t},ij} = \mu_\mathrm{t}\left(\frac{\partial v_{\mathrm{m},i}}{\partial x_j} + \frac{\partial v_{\mathrm{m},j}}{\partial x_i}\right)$$

where the subscript "t" refers to turbulence and μ_t is the *turbulent or eddy viscosity* which has the same dimensions of μ.

As consequence, the Reynolds stress tensor $\underline{\mathbf{\Phi}}_\mathrm{Re}$ can be written with the same form of the viscous stress tensor $\underline{\mathbf{\Phi}}$ (Equation 3.38):

$$\underline{\mathbf{\Phi}}_\mathrm{Re} = \frac{2}{3}k\underline{\mathbf{I}} + 2\nu_\mathrm{t}\underline{\mathbf{D}_\mathrm{m}} \tag{4.21}$$

where $\nu_\mathrm{t} = \mu_\mathrm{t}/\rho$ is the *turbulent cinematic viscosity* [18]. This fact allows to derive the six component of the Reynolds stress tensor by defining just the two quantities k and ν_t.

The Boussinesq assumption is both the strength and the weakness of two equation models. This assumption is a huge simplification which allows one to think of the effect of turbulence on the mean flow in the same way as molecular viscosity affects a laminar flow. The assumption also makes it possible to introduce intuitive scalar turbulence variables like the turbulent kinetic energy k and dissipation rate ε and relate thereafter these variables to even more intuitive variables like turbulence intensity and turbulence length scale. The weakness of the Boussinesq assumption is that it is not generally valid: there is no evidence that the Reynolds stress tensor is proportional to the strain rate tensor $\underline{\mathbf{D}_\mathrm{m}}$: this is probably true in simple flows like straight boundary layers and wakes, but in complex flows, like flows with strong curvature, or strongly accelerated or decelerated flows the Boussinesq assumption is simply not valid. This fact gives to the two equation models inherent problems to predict strongly rotating

flows, flows where curvature effects are significant or strongly decelerated flows involving stagnation [19].

4.4.2 The k-ε models

The $k-\varepsilon$ models are one of the most common turbulence models which have become an industry standard and commonly used for the most types of engineering problems. They are two equation models, which means that they include two extra transport equations to represent the turbulent properties of the flow: this allows to account for history effects like convection and diffusion of turbulent energy. The first transported variable is turbulent kinetic energy k that determines the energy in the turbulence while the second one is the turbulent dissipation rate ε which is directly related to the scale of the turbulence. The basic idea behind this model is explained below.

The turbulent cinematic viscosity ν_t can be alternatively expressed as

$$\nu_t = C_\mu \frac{k^2}{\varepsilon}$$

where C_μ is a constant experimentally determined to be equal to 0.09 [17]. Equation 4.21 can then be finally written as

$$\underline{\mathbf{\Phi}}_{\mathrm{Re}} = \frac{2}{3} k \, \underline{\mathbf{I}} + 2 \, C_\mu \frac{k^2}{\varepsilon} \underline{\mathbf{D}}_{\mathrm{m}}$$

which express $\underline{\mathbf{\Phi}}_{\mathrm{Re}}$ as a function of the only two variables k and ε: this relation is obviously approximated since it express 6 new unknown variables as a function of just two variables. As previously mentioned, two transport equations are then added in order to express k and ε as a function of the flow field variable allowing the effective analytical closure of the RANS equations.

4.4.3 The RNG $k-\varepsilon$ model

The RNG model was developed using Re-Normalisation Group (RNG) methods by Yakhot *et al.* [20] to renormalize the Navier-Stokes equations, to account for the effects of smaller scales of motion. In the standard $k-\varepsilon$ model the eddy viscosity is determined from a single turbulence length scale, so the calculated turbulent diffusion is the one which occurs only at the specified scale, whereas in reality all scales of motion will contribute to the turbulent diffusion. The RNG approach, which is a mathematical technique that can be used to derive a turbulence model similar to the $k-\varepsilon$, results in a modified form of the epsilon equation which attempts to account for the different scales of motion through changes to the production term. The resulting RNG model has different constants from those in the standard $k-\varepsilon$ model, and additional terms and functions in the transport equations for k and ε. These features make the RNG model more accurate and

reliable for a wider class of flows than the standard model. Moreover, while the standard $k-\varepsilon$ model is a high-Reynolds-number model, the RNG theory provides an analytically-derived differential formula for effective viscosity that accounts for low-Reynolds-number effects. Effective use of this feature does, however, depend on an appropriate treatment of the near-wall region. [21]

4.4.4 The Realizable $k-\varepsilon$ model

One of the most successful recent developments in $k-\varepsilon$ models is the Realizable model developed by Shih *et al.* [22]. This model contains a new transport equation for the turbulent dissipation rate, along with the critical coefficient C_μ which is expressed as a function of mean flow and turbulence properties, rather than assumed to be constant as in the standard model. This fact allows the model to satisfy certain mathematical constraints on the normal stresses consistent with the physics of turbulence (realizability). The concept of a variable is also consistent with experimental observations in boundary layers.

The realizable $k-\varepsilon$ model is substantially better than the standard $k-\varepsilon$ model for many applications, and can generally be relied upon to give answers that are at least as accurate. An immediate benefit of the Realizable $k-\varepsilon$ model is that it more accurately predicts the spreading rate of both planar and round jets. It is also likely to provide superior performance for flows involving rotation, boundary layers under strong adverse pressure gradients, separation, and recirculation. Because of these reasons, this is the chosen model for the simulations carried out in the present work.

Chapter 5

Computational Fluid Dynamics and numerical methods

An overview on Computational Fluid dynamics (CFD) is introduced in this section, since in the present work a PWJ process numerical analysis by means of CFD is carried out. Therefore, a collection of the basic principles and the numerical methods which CFD is founded on is presented, with a specific insight on the methods that have been employed in the present work.

Computational Fluid Dynamics is one of the branches of fluid mechanics that uses numerical methods and algorithms to solve and analyze problems that involve fluid flows.

5.1 Numerical methods

The differential equations presented in the Section 3.4 describe the continuous movement of a fluid in space and time. To be able to solve those equations numerically, all aspects of the process need to be discretized, or changed from a continuous to a discontinuous formulation. For example, the region where the fluid flows needs to be described by a series of connected control volumes, or computational cells; the equations themselves need to be written in an algebraic form; advancement in time and space needs to be described by small, finite steps rather than the infinitesimal steps. All of these processes are collectively referred to as *discretization*. Discretization of the domain, or grid generation, and discretization of the equations are described in this section [23].

5.1.1 Domain discretization: mesh generation

The domain is broken into a set of discrete sub-domains, or computational cells, or control volumes, by a grid also called *mesh*, which contains elements of many shapes and sizes. The elements are usually either quadrilaterals or triangles in 2D domains, as presented in Figure 5.2, while they can be tetrahedra (with four sides), prisms (five sides), pyramids (five sides) or hexahedra (six sides) in a 3D domain.

A series of line segments (2D) or planar faces (3D) connecting the boundaries of the domain are used to generate the elements: structured grids are always quadrilateral (2D) or hexahedral (3D), and every their element is aligned to the grid coordinate directions and is therefore spatially and geometrically organized coherently with the elements surrounding it. Structured meshes produce the best results precision and stability during calculations, even if they can only be correctly generated for simple and linear geometries.

On the contrary, unstructured grids do not follow any organized pattern, with the elements which are deformed and arranged by the mesh generator in order to adapt even to complex geometries with curved boundaries. See Figure 5.1 for a visual comparison between structured and unstructured mesh.

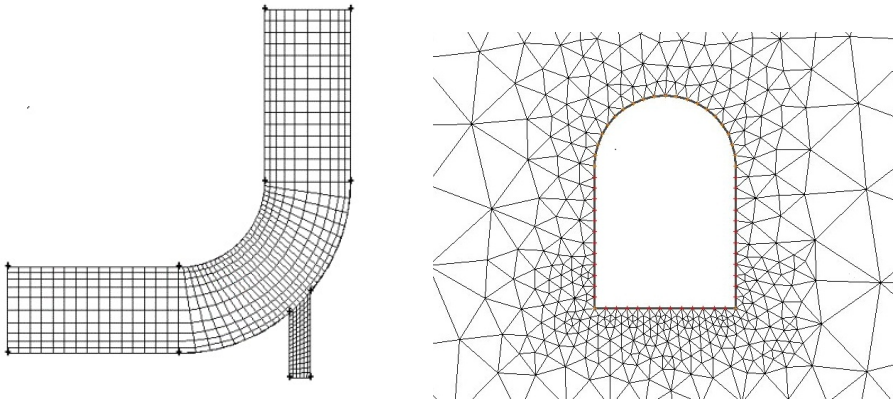

(a) *Example of structured mesh (www.fluent.com).* **(b)** *Example of unstructured mesh (www.rocscience.com),*

Figure 5.1: *Comparison between structured **(a)** and unstructured **(b)** mesh.*

In general, the density of cells in a computational grid needs to be fine enough to capture the flow details, but not so fine that the overall number of cells in the domain is excessively large, since problems described by large numbers of cells require more time to solve. Nonuniform grids of any topology and adaptive meshing methods can be used to focus the grid density in regions where it is needed and allow for expansion in other regions.

Choose the appropriate mesh type

When choosing the mesh type, the following issues must be considered. [21]:

Setup time: many flow problems solved in engineering practice involve complex geometries. The creation of structured or block-structured grids (consisting of quadrilateral or hexahedral elements) for such problems can be extremely time-consuming if not impossible. Therefore, setup time for complex geometries is the major motivation for using unstructured grids employing triangular or tetrahedral cells. However, if your geometry is relatively simple, there may be no saving in setup time with both the approaches, and the generation of a structured mesh is strongly recommended as it leads to more stable calculations.

Computational expense: when geometries are complex or the range of length scales of the flow is large, a triangular/tetrahedral mesh can be created with far fewer cells than the equivalent mesh consisting of quadrilateral/hexahedral elements. This is because a triangular/tetrahedral mesh allows clustering of cells in selected regions of the flow domain, while structured quadrilateral/hexahedral meshes will generally force cells to be placed in regions where they are not needed. Unstructured quadrilateral/hexahedral meshes cover many of the advantages of triangular/tetrahedral meshes for moderately-complex geometries.

A characteristic of quadrilateral/hexahedral elements that might make them more economical in some situations is that they permit a much larger aspect ratio than triangular/tetrahedral cells. A large aspect ratio in a triangular/tetrahedral cell will invariably affect the skewness of the cell, which is undesirable as it may impede accuracy and convergence.

Therefore, if you have a relatively simple geometry in which the flow conforms well to the shape of the geometry, such as a long thin duct, use a mesh of high-aspect ratio quadrilateral/hexahedral cells. The mesh is likely to have far fewer cells than if you use triangular/tetrahedral cells.

Numerical diffusion: all practical numerical schemes for solving fluid flow contain a finite amount of numerical diffusion as explained in Section 5.2.5. This is because numerical diffusion arises from truncation errors that are a consequence of representing the fluid flow equations in discrete form. The amount of numerical diffusion is inversely related to the resolution of the mesh and it is minimized when the flow is aligned with the mesh. Therefore, one way of dealing with numerical diffusion is to refine the mesh and align it along the flow direction. This is the most relevant point to the choice of the grid. If you use a triangular/tetrahedral mesh, the flow can never be aligned with the grid. If you use a quadrilateral/hexahedral

mesh, this situation might occur, but not for complex flows. It is only in a simple flow, such as the flow through a long duct, in which you can rely on a quadrilateral/hexahedral mesh to minimize numerical diffusion and get a better solution with fewer cells than using a triangular/tetrahedral mesh.

Furthermore, helpful solution-adaptive mesh algorithms are also available, as it will be presented in Section 11.4.

Mesh quality

The quality of the mesh plays a significant role in the accuracy and stability of the numerical computation. The attributes associated to mesh quality are node point distribution, smoothness, and skewness.

Node density: since you are discretely defining a continuous domain, the degree to which the salient features of the flow (such as shear layers, separated regions, shock waves, boundary layers, and mixing zones) are resolved, depends on the density and distribution of nodes in the mesh. In many cases, poor resolution in critical regions can dramatically alter the flow characteristics. Proper resolution of the mesh for turbulent flows is also very important. Due to the strong interaction of the mean flow and turbulence, the numerical results for turbulent flows tend to be more susceptible to grid dependency than those for laminar flows. For this latter case, see the example reported in Section 11.3.

In general, no flow passage should be represented by fewer than 5 cells. Most cases will require many more cells to adequately resolve the passage. In regions of large gradients, as in shear layers or mixing zones, the grid should be fine enough to minimize the change in the flow variables from cell to cell. Unfortunately, it is very difficult to determine the locations of important flow features in advance. Moreover, the grid resolution in most complicated flow fields will be constrained by CPU time and computer resource limitations (i.e., memory and disk space). Although accuracy increases with larger grids, the CPU and memory requirements to compute the solution and post-process the results also increase. Solution-adaptive grid refinement can be used to increase and/or decrease grid density based on the evolving flow field, and thus provides the potential for more economical use of grid points (and hence reduced time and resource requirements). These methods will be largely employed in present work, as explained in Section 11.4 and 12.4.

Smoothness: truncation error is the difference between the partial derivatives in the governing equations and their discrete approximations. Rapid changes in cell volume between adjacent cells translate into larger truncation errors.

FLUENT®provides the capability to improve the smoothness by refining the mesh based on the change in cell volume or the gradient of cell volume.

Cell shape: the shape of the cell (including its skewness and aspect ratio) also has a significant impact on the accuracy of the numerical solution.

- **Skewness** is defined as the difference between the shape of the cell and the shape of an equilateral cell of equivalent volume. Highly skewed cells can decrease accuracy and destabilize the solution. For example, optimal quadrilateral meshes will have vertex angles close to 90°, while triangular meshes should preferably have angles of close to 60° or generally all angles less than 90°. Usually skewness is expressed with a "equi-size skewness" factor varying in the range from 0 (non-distorted element) to 1 (very distorted element); good mesh have skewness factors at least below 0.5.
- **Aspect ratio** is a measure of the stretching of the cell and it is defined in 2D cells as the ratio of the maximum and the minimum distance between the cell centroid and face centroids. For highly anisotropic flows, the use of extreme aspect ratios cells stretched along the flow direction may yield accurate results with fewer cells. However, a general rule is to avoid aspect ratios in excess of 5:1 [21].

5.1.2 Discretization of the equations

Several methods have been employed over the years to numerically solve the Navier-Stokes equations, including the finite difference, finite element, spectral element, and finite volume methods. The focus of this chapter is on the finite volume method, which is the one employed in FLUENT®solver. Since this is the solver employed, the finite volume method is described in detail below.

To illustrate the discretization of a typical transport equation using the finite volume formulation [24][25], a generalized scalar equation can be used with the rectangular control volume shown in Figure 5.3. The scalar equation for the generic variable ϕ has the following form:

$$\frac{\partial(\rho\,\phi)}{\partial t} + \frac{\partial}{\partial x_i}(\rho\, v_i\, \phi) = \frac{\partial}{\partial x_i}\left(\Gamma \frac{\partial \phi}{\partial x_i}\right) + S' \tag{5.1}$$

The parameter Γ is used to represent the diffusion coefficient for the scalar ϕ; if ϕ is one of the components of velocity, for example, Γ would represent the viscosity. All sources are collected in the term S'; again, if ϕ is one of the components of velocity, S' would be the sum of the pressure gradient, the gravitational force, and any other additional forces.

The control volume has a node P, at its center, where all problem variables are stored. The transport equation describes the flow of the scalar ϕ into and

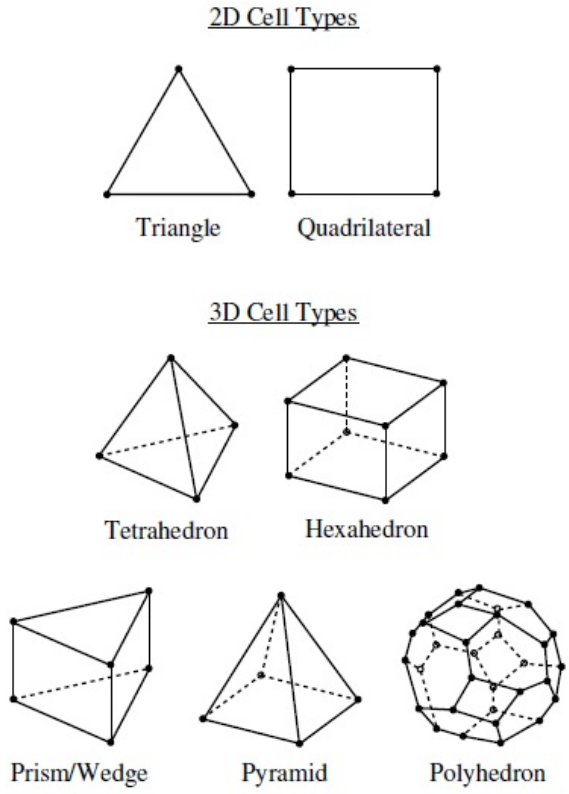

Figure 5.2: *Different mesh cell types [21].*

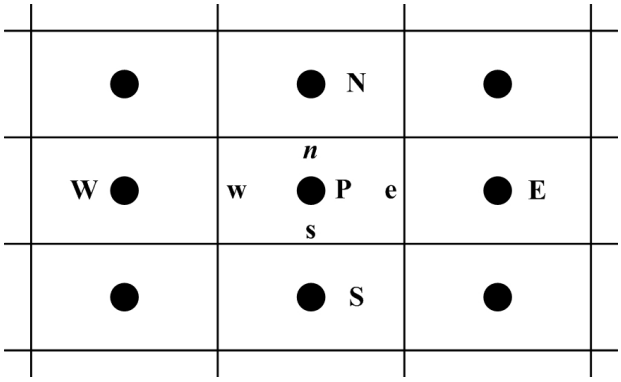

Figure 5.3: *Quadrilateral 2D mesh showing cell centers and faces [23].*

out of the cell through the cell faces *n*,*s*,*w* and *e*. The neighboring cells also have nodes at their centers, and these are labeled with the capital letters *E*, *W*, *N*, and *S*. 1D-flow along the row of cells $W \rightarrow P \rightarrow E$ of Figure 5.3 is considered for the purpose of this example.

The first step in the discretization of the transport equation is an integration over the control volume. The volume integral can be converted to a surface integral by applying the divergence theorem. Using a velocity in the positive x-direction, neglecting time-dependence, and assuming that the faces e and w have area A, the integrated transport equation takes the following form:

$$(\rho_e u_e \phi_e - \rho_w u_w \phi_w)A = \left(\Gamma_e \left[\frac{d\phi}{dx}\right]_e - \Gamma_w \left[\frac{d\phi}{dx}\right]_w\right)A + S \tag{5.2}$$

where S is the volume integral of the source terms contained in S'. This expression contains four terms that are evaluated at the cell faces. A discretization scheme is required in order to obtain the face values of these terms as a function of values that are stored at the cell centers.

5.1.3 Discretization schemes

As previously presented, a discretization scheme is necessary in order to allow the discretization of the differential equations as the ones presented in Equation (5.2). Since all of the problem variables are stored at the cell center, the face values (the derivatives) need to be expressed in terms of cell center values. To do this, consider a steady-state conservation equation in one dimension without any source terms:

$$\frac{d}{dx}(\rho\, v\, \phi) = \frac{d}{dx}\left(\Gamma \frac{d\phi}{dx}\right) \tag{5.3}$$

This equation can be exactly solved. On a linear domain that extends from $x = 0$ to $x = \mathrm{L}$, corresponding to the locations of two adjacent cell nodes, with $\phi = \phi_0$ at $x = 0$ and $\phi = \phi_\mathrm{L}$ at $x = \mathrm{L}$, the solution for ϕ at any intermediate location (such as the face) has the form:

$$\phi = \phi_0 + (\phi_\mathrm{L} - \phi_0)\frac{\exp\left(Pe\frac{x}{L} - 1\right)}{\exp(\mathrm{Pe\text{-}1})}$$

where the Peclet number Pe is the ratio between convection and diffusion influence on the flow field:

$$Pe = \frac{\rho\, u\, L}{\Gamma}$$

Depending on the value of Pe, different limiting behavior exists for the variation of ϕ between $x = 0$ and $x = L$. These limiting cases are discussed below, along with some more rigorous discretization or differencing schemes that are in popular use today [23].

Central differencing scheme

For $Pe = 0$, there is no convection and the solution is purely diffusive. This would correspond to heat transfer due to pure conduction, for example. In this case, the variable ϕ varies linearly from cell center to cell center, so the value at the cell face can be found from linear interpolation. When linear interpolation is used in general, i.e when both convection and diffusion are present, the discretization scheme is called central differencing. When used in this manner, as a general purpose discretization scheme, it can lead to errors and loss of accuracy in the solution. One way to reduce these errors is to use a refined grid, but the best way is to use another differencing scheme. There is one exception to this rule.

Upwind differencing scheme

For $Pe \gg 1$, convection dominates and the value at the cell face can be assumed to be identical to the upstream or upwind value (i.e. $\phi_w = \phi_W$). When the value at the upwind node is used at the face, independently of the flow conditions, the process is called first order upwind differencing. A modified version of first order upwind differencing makes use of multi-dimensional gradients in the upstream variable, based on the upwind neighbor and its neighbors. This scheme, which makes use of a Taylor series expansion to describe the upwind gradients, is called *second order upwind* differencing. It offers greater accuracy than the first order upwind method, but requires additional computational effort.

Power law differencing scheme

For intermediate values of the Peclet number, $0 < Pe < 10$, the face value can be computed as a function of the local Peclet number. This expression can be approximated by one that does not use exponentials, involving the Peclet number raised to an integral power. It is from this approximate form that the power law differencing scheme draws its name. This first order scheme is identical to the first order upwind differencing scheme in the limit of strong convection, but offers slightly improved accuracy for the range of Pe numbers mentioned above.

QUICK differencing scheme

The QUICK differencing scheme [26] is similar to the second order upwind differencing scheme, with modifications that restrict its use to quadrilateral or hexahedral meshes. In addition to the value of the variable at the upwind cell center, the value from the next upwind neighbor is also used. Along with the value at the node P, a quadratic function is fitted to the variable at these three points and used to compute the face value. This scheme can offer improvements over the second order upwind differencing scheme for some flows with high swirl.

Choosing the most appropriate differencing scheme

If the flow is aligned with the grid, first order differencing schemes such as upwind and power law differencing are acceptable. Flow in a straight pipe modeled with a hexahedral grid is one example where these schemes would be sufficient. However, since flow patterns in both static and stirred mixers do not generally satisfy this condition, especially if unstructured grids are used, second order differencing is recommended to reduce the numerical errors in the final solution. In general, first order schemes allow the error to reduce linearly with the grid spacing while second order schemes allow the error to reduce as the square of the grid spacing. A common practice in CFD is to obtain a partially converged solution using one of the first order schemes, and then switch to a higher order scheme to obtain the final converged result.

5.1.4 Final discretized solution

Once the face values have been computed using one of the above differencing schemes, terms multiplying the unknown variable at each of the cell centers can be collected. Large coefficients multiply each of these terms. These coefficients contain information that includes the properties, local flow conditions, and results from previous iterations at each node. In terms of these coefficients, A_i, the discretized equation has the following form for the simple 2D grid shown in Figure 5.3:

$$A_P\phi_P = A_N\phi_N + A_S\phi_S + A_E\phi_E + A_W\phi_W = \sum_{i,\text{neighbors}} A_i\phi_i \tag{5.4}$$

For a complex, or even a simple flow simulation, there will be one equation of this form for each variable solved, in each cell in the domain. Furthermore, the equations are coupled, since, for example, the solution of the momentum equations will impact the transport of every other scalar quantity. It is the job of the solver to collectively solve all of these equations with the best accuracy in the shortest amount of time.

5.2 Solution methods

The result of the discretization process is a finite set of coupled algebraic equations that need to be solved simultaneously in every cell of the solution domain. For small problems (i.e. those with fewer than 1000 elements), a matrix inversion can be done. however, few problems can be solved with adequate solution accuracy using such a small cell count, so alternative methods are usually employed. Two iterative methods exist for this purpose: *segregated* and *coupled* solution approach.

One variable at a time is solved throughout the entire domain in a segregated solution approach. Thus the x-component of the velocity is solved on the entire domain, then the y-component is solved, and so on. One iteration of the solution is complete only after each variable has been solved in this manner.

In a coupled solution approach, on the other hand, is one where all variables, or at least, momentum and continuity, are solved simultaneously in a single cell before the solver moves to the next cell, where the process is repeated. The segregated solution approach is popular for incompressible flows with complex physics, typical of those found in mixing applications. Typically, the solution of a single equation in the segregated solver is carried out on a cells subset, using a Gauss-Seidel linear equation solver. The solution time can be improved (i.e. reduced) in some cases, by using an algebraic multigrid correction scheme.

Independently of the method used, however, the equations must be solved over and over again until the collective error reduces to a value that is below a pre-set minimum value. At this point, the solution is considered converged, and the results are most meaningful. Converged solutions should demonstrate overall balances in all computed variables, including mass, momentum, heat, and species for example.

5.2.1 The SIMPLE algorithm

The three equations of motion and the equation of continuity combine to form a system of four equations (3.43) for the four unknowns that are the pressure p and the three velocity components of vector $\mathbf{v}$. Because there is no explicit equation for the pressure, special techniques have been devised to extract it in an alternative manner. The most well known of these techniques is the SIMPLE algorithm, or Semi-Implicit Method for Pressure-Linked Equations [24]. Indeed, a family of algorithms has been derived from this basic one (such as SIMPLEC, PISO or Fractional-Step method), each one of them with a small modification that makes it well suited to one application or another. A deeper insight on PISO algorithm will be presented in the following section 5.2.1, as this is the algorithm employed in the present work.

The essence of SIMPLE algorithm is as follows: a guessed pressure field is used in the solution of the momentum equations (for all but the first iteration, the guessed pressure field is simply the last updated one). The new velocities are computed, but these will not, in general, satisfy the continuity equation, so corrections to the velocities are determined. Based on the velocity corrections, a pressure correction is computed which, when added to the original guessed pressure, results in an updated pressure. Following the solution of the remaining problem variables, the iteration is completed and the entire process repeated.

PISO

The Pressure-Implicit with Splitting of Operators (PISO) pressure-velocity coupling scheme, part of the SIMPLE family algorithms, is based on the higher degree of the approximate relation between the corrections for pressure and velocity. One of the limitations of the SIMPLE algorithm is that new velocities and corresponding fluxes do not satisfy the momentum balance after the pressure-correction equation is solved. As a result, the calculation must be repeated until the balance is satisfied. To improve the efficiency of this calculation, the PISO algorithm performs two additional corrections: *neighbor correction* and *skewness correction*.

Neighbor correction The main idea of the PISO algorithm is to move the repeated calculations required by SIMPLE inside the solution stage of the pressure-correction equation [27]. After one or more additional PISO loops, the corrected velocities satisfy the continuity and momentum equations more closely. This iterative process is called a momentum correction or "neighbor correction".

The PISO algorithm takes a little more CPU time per solver iteration, but it can dramatically decrease the number of iterations required for convergence, especially for transient problems. This makes it perfectly suitable for the purposes of a PWJ numerical simulation.

Skewness correction For meshes with some degree of skewness, the approximate relationship between the correction of mass flux at the cell face and the difference of the pressure corrections at the adjacent cells is very rough. Since the components of the pressure-correction gradient along the cell faces are not known in advance, an iterative process similar to the PISO neighbor correction described above is desirable [28]. After the initial solution of the pressure-correction equation, the pressure-correction gradient is recalculated and used to update the mass flux corrections. This process, which is referred to as "skewness correction", significantly reduces convergence difficulties associated with highly distorted meshes.

Moreover, in case of meshes with a high degree of skewness, the simultaneous coupling of the neighbor and skewness corrections at the same pressure correction equation source may cause divergence or a lack of robustness. An alternative, although more expensive, method for handling the neighbor and skewness corrections inside the PISO algorithm is to apply one or more iterations of skewness correction for each separate iteration of the neighbor correction. For each individual iteration of the classical PISO algorithm [27], this technique allows a more accurate adjustment of the face mass flux correction according to the normal pressure correction gradient.

For the present numerical model developed, since the mesh generated is basically formed by quadrilateral elements, its level of skewness is extremely low and no corrections are needed.

5.2.2 Residuals

If the algebraic form of a conservation equation (Equation 5.4) in any control volume could be exactly solved, it would be written as:

$$A_P\phi_P - \sum_{i,\text{neighbors}} A_i\phi_i = 0$$

Since the solution of each equation at any step in an iterative calculation is based on inexact information, originating from initial guessed values and refined through repeated iterations, the right hand side of the above equation is always non-zero. This non-zero value represents the error, or *residual* in the solution of the equation in the control volume.

$$A_P\phi_P - \sum_{i,\text{neighbors}} A_i\phi_i = R_P$$

The total residual is the sum over all cells in the computational domain of the residuals in each cell:

$$R_{\text{tot}} = \sum_{i,\text{cells}} R_i$$

Since the total residual, R_{tot}, defined in this manner, is dependent upon the magnitude of the variable being solved, it is customary to either normalize or scale the total residual to gauge its changing value during the solution process. While normalization and scaling can be done in a number of ways, it is important to evaluate the change in the normalized or scaled residuals to check the rate and level of convergence of the solution.

5.2.3 Convergence criteria

The convergence criteria are preset conditions (generally user-defined) for the usually normalized or scaled residuals that determine when an iterative solution is converged. One convergence criterion could require that the total normalized residual for the pressure equation drop below 1E-03. Another could require that the total scaled residual for a species equation drop below 1E-06. Alternatively, it could require that the sum of all normalized residuals drops below 1E-04. For any set of convergence criteria, the assumption is that the solution is no longer changing when the condition is reached, and that there is an overall mass balance throughout the domain. When additional scalars are being solved (heat and species, for example), there should be overall balances in these scalars as well. Whereas the convergence criteria indicate that overall balances probably exist, further examination are recommended to verify that indeed they do.

5.2.4 Under-relaxation

The solution of a single differential equation, solved iteratively, makes use of information from the previous iteration. If ϕ_n is the value of the variable from the previous iteration and ϕ_{n+1} is the new value, then some small difference or change in the variable brings the variable from the old value to the new one:

$$\phi_{n+1} = \phi_n + \Delta\phi$$

Rather than use the full computed change in the variable, $\Delta\phi$, it is often necessary to use a fraction of the computed change when several coupled equations are involved:

$$\phi_{n+1} = \phi_n + \text{URF}\ \Delta\phi$$

This process is called under-relaxation, and under-relaxation factors (URF) typically range from 0.1 to 1.0 depending on the complexity of the flow physics (laminar flow or turbulent reacting flow, for example), the variable being solved (pressure or momentum), the solution method being used, and the state of the solution (during the first few iterations or near convergence). Lowering URFs makes the convergence process stable, but slower. Guidelines exist for the optimum choices for under-relaxation factors for a variety of conditions [21]. As the solution converges, the under-relaxation factors should be gradually raised to ensure convergence that is both rapid and stable at all times.

5.2.5 Numerical diffusion

Numerical diffusion is a source of error that is always present in CFD, owing to the fact that approximations are made during the equations discretization process. It is so named because it presents as equivalent to an increase in the diffusion coefficient. Thus the fluid will appear more viscous in the solution of the momentum equation; the solution will appear to have a higher conductivity in the solution of the energy equation; in the solution of the species equation, it will appear that the species diffusion coefficient is larger than in actual fact. These errors are most noticeable when diffusion is small in the actual problem definition.

Two steps can be taken to minimize numerical diffusion:

- First, a higher order discretization scheme can be used, such as the QUICK or second order upwinding schemes discussed in Section 5.1.3.
- Second, the grid can be built to minimize the effect. Numerical diffusion is generally a problem on coarse grids, so it is wise to plan ahead and avoid coarse meshes in regions where the most accuracy is sought. Numerical diffusion is generally a less noticeable problem with quadrilateral or hexahedral meshes, if the flow is aligned with the mesh.

Unfortunately, the flow is rarely aligned to the mesh throughout the entire flow field, so certain levels of numerical diffusion are unavoidable.

5.2.6 Time dependance

The time derivative appearing in Equation (5.1) must be discretized to solve a time-dependent problem. If $F(\phi)$ is the spatially discretized part of Equation (5.1), the time derivative can be approximated to first order as:

$$\frac{\phi^{n+1} - \phi^n}{\Delta t} = F(\phi) \tag{5.5}$$

In this expression, ϕ^n is the solution at time t and ϕ^{n+1} is the solution at time $t + \Delta t$. While certain flow conditions, such as compressible flow, are best suited to an explicit method for the solution of Equation (5.5), an implicit method is usually the most robust and stable choice for a wide variety of applications, including mixing. The major difference between the explicit and implicit methods is whether the right hand side of Equation (5.5) is evaluated at the current time so that $F(\phi) = F(\phi^n)$ or at the next time step so that $F(\phi) = F(\phi^{n+1})$. The implicit method uses the latter:

$$\phi^{n+1} = \phi^n + \Delta t\, F(\phi^{n+1})$$

The assumption at the core of this quasi-steady approach is that the new value of the variable ϕ prevails throughout the entire time step, which takes the solution from time t to time $t + \Delta t$.

5.3 CFD applications and advantages

CFD is becoming an always growing and promising mean in engineering design processes. Therefore, the main application fields re conceptual studies of new design and solutions along with new detailed product development, troubleshooting and redesign of already existing projects; furthermore, CFD analysis complements testing and experimentation since a reliable numerical model reduces the total effort required in the experimental design and data acquisition.

A series of the main advantages of CFD is listed below [17]:

- Relatively low cost: there is no need to build a new physical model for each trial.
- Relatively fast: even if some simulations can take long time depending on the available computational power, most of the simulations are faster than building and testing a physical model.
- Flexible: changing physical properties and boundary conditions is straightforward and rapid. The settings can be easily modified and controlled.

- Easy to set ideal conditions such as incompressibility which is often impossible in reality.
- Complete control of the physical process since different physical models can be easily changed or modified according to the working conditions.
- Comprehensive informations: numerical simulations give a map of the results of each physical variable throughout the whole domain, while empirical experiments can extract just single measures in limited regions.

5.4 Limitations of CFD

The following is a list of the main limitations and drawbacks of CFD mainly deriving by the fact that numerical models unavoidably bring along numerical errors and physical approximations:

- **Numerical errors**:
  - Round-off error: it is due to finite word size (depending on the bit number) available in the employed computer; this error is always present even though it is often very small.
  - Truncation error: it is due to numerical approximations in numerical model; this error goes to zero as the grid is refined.
- **Physical models**: CFD solutions rely upon physical models of real world processes such as turbulence, compressibility, chemistry, multiphase flow, etc... As a consequence, solutions can only be as accurate as the physical models on which they are based on.
- **Boundary conditions**: the accuracy of the CFD solution is strongly dependent on the initial boundary conditions provided to the numerical model.

Chapter 6

Multiphase Models in FLUENT

Most of the fluid-dynamic problems involve more than one fluid or phase: multiphase models are then developed with the aim of modeling the flow field of different phases interacting with each other. In fluid dynamics and computational fluid dynamics, a phase is defined as an identifiable class of material that has a particular inertial response and interaction with the flow and the potential field in which it is immersed.

According to the different nature of the interacting phases, multiphase flow regimes can be grouped into four main categories [21]:

1. Gas-liquid or liquid-liquid flows which are distinguished in:
    - Bubbly flow: this is the flow of discrete gaseous or fluid bubbles in a continuous fluid;
    - Droplet flow: this is the flow of discrete fluid droplets in a continuous gas;
    - Slug flow: this is the flow of large bubbles in a continuous fluid;
    - Stratified/free surface flow: This is the flow of immiscible fluids separated by a clearly-defined interface.
2. Gas-solid flows distinguished in:
    - Particle-laden flow: this is the flow of discrete particles in a continuous gas;
    - Pneumatic transport: this is a flow pattern involving transport in ducts that depends on factors such as solid loading, Reynolds numbers, and particle properties;
    - Fluidized bed: this consists of a vertical cylinder containing particles; a gas is introduced and rises through the bed suspending the particles.

Depending on the gas flow rate, bubbles appear and rise through the bed, intensifying the mixing process.

3. Liquid-solid flows distinguished in:
   - Slurry flow: this is the transport of particles in liquids. The behavior of liquid-solid flows varies according to the relative properties of the solid particles and those of the liquid. Stokes number St (see Section 6.2.4) is normally less than 1; when the Stokes number overcomes 1, the regime of the flow is liquid-solid fluidization;
   - Hydrotransport: this describes densely-distributed solid particles in a continuous liquid;
   - Sedimentation: this describes the situation of a tall recipient initially containing a uniform dispersed mixture of particles slowly falling toward the bottom and forming a sludge layer; at the top of it, a clear interface will appear, and a constant settling zone will exist in the middle.
4. Three phases flows which are a combination of some of the previously presented flow regimes.

Similarly to what reported in Section 3.2.1, there are both a Euler-Lagrangian and Euler-Euler approaches to mutiphase models, as it will be presented below.

6.1 The Euler-Lagrangian Approach

This is one of the simplest methods to solve a multiphase problem even if it is suitable just for models where the second phase can be considered as dispersed. The main fluid phase is treated as a continuum by solving the time-averaged Navier-Stokes equations in an Eulerian way (the first term *Euler* in the approach name is due to this fact), while the single particles are observed on their way through the flow field by solving the equations of particle motion and particle position in a Lagrangian approach (from which the subsequent term *Lagrangian* in the name). The two phases can exchange energy, momentum or mass among each other. The basic assumption of this model is that the dispersed second phase occupies a low volume fraction, even though high mass loading is accepted. The trajectories of the particles are then computed individually at specified intervals during the fluid phase calculation [21, 29].

These features make this approach appropriate for spray modeling, coal and liquid fuel combustion, and some particle-laden flows, but inappropriate for the modeling of liquid-liquid mixtures, fluidized beds, or any application where the volume fraction of the second phase is not negligible as in the case of water jet. Because of this fact, this model will no longer be studied in deep.

6.2 The Euler-Euler Approach and its Models

The Euler-Euler or Eulerian-Eulerian is the most general approach in simulating multiphase flows. In principle, any multiphase flow can be simulated this way. Each individual fluid is treated as a continuous phase and conservation laws apply for each fluid within an Eulerian approach. The concept of the volume fraction is introduced as a consequence of the assumption that the volume of a phase cannot be occupied by any other phase; these volume fractions are then assumed to be continuous functions of space and time and their sum is equal to one for each control volume.

Three different Euler-Euler multiphase models are availablein FLUENT®: the mixture model, the Eulerian model and the volume of fluid (VOF) model which are briefly explained below.

6.2.1 The Mixture Model

The mixture model is a simplified multiphase model that can be used to model multiphase flows where the phases move at different velocities, but assume local equilibrium over short spatial length scales: the coupling between the phases should then be strong. The concept behind this model is intuitively simple: the continuity and momentum equation are written in the same form of those for a single-phase flow but referring to a mixture of continuous and dispersed phases; the slip of the dispersed phase relatively to the continuous phase is later calculated by balancing the drag and the body forces resulting from differences in density, while the volume fraction for each dispersed phase is solved from a phase continuity equation. This way, only one set of velocity components is solved from the momentum differential equation, saving computational effort if compared to the complete multiphase Eulerian model presented in Section 6.2.2 [30]. The mixture model has enjoyed success with gas-liquid and liquid-granular mixtures of all types and it forms the basis of the cavitation model, which allows for mass transfer due to pressure tension between liquid and gaseous phases [31].

6.2.2 The Eulerian Model

The Eulerian multiphase model is the most general and complex model. Making use of separate sets of momentum, continuity and, if necessary, energy equations for each phase, it can be applied to mixtures with individual phase concentrations from 0 to 100% [31]: as a consequence additional sets of conservation equations must be introduced and the original set must also be necessarily modified. The modifications involve, among other things, the introduction of the volume fractions for the multiple phases, as well as mechanisms for the exchange of momentum, heat, and mass between the phases.

Coupling and interaction between phases is achieved through the pressure and interphase exchange coefficients and the way this coupling is handled depends upon the type of phases involved, i-e. whether a granular (fluid-solid) flows rather than nongranular (fluid-fluid) flow is being modeled.

6.2.3 The VOF Model

While the Eulerian and mixture models are appropriate for fluid mixtures, they are not the most suitable for immiscible fluids. For this class of problems, the shape and evolution of the free surface is often of interest. The volume of fluid method (or in short VOF method) is a numerical technique for tracking and locating the free surface (also called fluid-fluid interface) in a fixed Eulerian mesh. The VOF method is known for its ability to conserve the "mass" of the traced fluid and even when the fluid interface changes its topology, this change is traced easily, so that the interfaces can for example join, or break apart.

As this method is particularly suitable for stratified flows and breakup prediction or transient tracking of any liquid-gas interface, it is perfectly suitable to simulate the WJ process which is characterized by a jet of water immersed in air; because of this, a deeper insight to this model will be presented in Section 7.

6.2.4 How to Choose the Appropriate Model

The first step in choosing a multiphase model is to approximately determine the flow regime, the type and the percentage of the phases involved: for stratified, surface-free or slug flows the choice of VOF is straightforward, while the mixture and Eulerian models are appropriate for flows in which the phases mix or separate and/or dispersed-phase volume fractions exceed 10%. If the dispersed-phase volume fraction in less than 10% it is also possible to use the Discrete phase model which is another specific built-in model (not strictly considered as multiphase) for problems involving a secondary discrete phase.

The choice between mixture and Eulerian model usually is not that straightforward on the other hand and the following guidelines should be considered: if the problem to be solved is pretty simple and requires a low computational effort, then the mixture model may be a better option, since it solves a smaller number of equations than the Eulerian model. While if accuracy is more important, the Eulerian model is the best choice. However, the complexity of the Eulerian model can make it less computationally stable than the mixture model. Moreover, the following parameters can help in evaluating which is the most appropriate multiphase model between Mixture or Eulerian:

- **Particulate loading and material density ratio** Particulate loading is defined as the mass density ratio between the dispersed phase and the carrier

phase:

$$\dot{p} = \frac{\alpha_d \, \rho_d}{\alpha_c \, \rho_c}$$

where the subscript d refers to the dispersed phase, while subscript c to the carrier phase; while the material density ratio is defined as

$$\varrho = \frac{\rho_d}{\rho_c}$$

Using these parameters it is possible to determine how the dispersed phase should be treated by estimating the average distance between the particles composing the particulate phase with the following expression

$$\frac{L}{d_d} = (\frac{\pi}{6}\frac{1+\kappa}{\kappa})^{1/3}$$

where $\kappa = \dot{p}/\varrho$.

Low $\dot{p}$: the distance between particles is high enough to suppose that the coupling is one-way: the main flow carries the particles via drag and turbulence without being influenced by them. In this case the Mixture model is strongly recommended because less computationally expensive.

Intermediate $\dot{p}$: the coupling is two-way as the carrier influences particles via drag and turbulence, but the particles as well influence the carrier reducing mean momentum and turbulence. Discrete phase, mixture and Eulerian models can all be applicable in this case and other factors like Stokes number should be taken into account.

High $\dot{p}$: the coupling is four-way as there is two-way coupling plus pressure and viscous stresses due to particulate. In this case Eulerian model is the only one able to solve the problem.

- **Stokes number** St As previously mentioned, in case of intermediate particulate loading another parameter to take into account is St, defined as the relation between particle (d) and system (s) response times:

$$St = \frac{\tau_d}{t_s} = \frac{\frac{\rho_d \, d_d^2}{18\mu_c}}{\frac{L_s}{v_s}} \tag{6.1}$$

where subscript c refers to the carrier phase and L_S and v_s are respectively the characteristic length and velocity of the system.

For $St \ll 1$ the particle will closely follow the flow and all the models can be used; it is therefore possible to chose the least expensive (mixture model). For $St > 1$ the particles will move independently and it is therefore needed

either the discrete phase or Eulerian model. For $St \approx 1$ again all the three model are suitable and the least expensive or the most appropriate, basing on other factors, must be chosen.

Chapter 7

The Volume Of Fluid multiphase model

As previously mentioned in Section 6.2.3 the VOF multiphase model is particularly suitable, among others, in modeling the prediction of jet breakup and the steady or transient tracking of any liquid-gas interface [21]; then it comes out to be an effective way to simulate WJ process and investigate the causes of jet breakup and its disturbances. On the other hand, since it is basically developed to work with immiscible fluids, its main drawback is the incapability in modeling phase transitions.

As this is the model employed throughout the present work, it will be explained more in detail below.

7.1 Overview

The problem of correctly tracing the boundary interface between two immiscible and interacting fluids has been challenging for CFD.

Discrete Lagrangian fluid representations are conceptually simple because each zone of a grid that subdivides the fluid into elements remains identified with the same fluid element for all time. Body and surface forces on these elements are easy to define, so it is relatively straightforward to compute the dynamic response of the elements. In an Eulerian representation the grid remains fixed and the identity of individual fluid elements is not maintained. Nevertheless, it is customary to view the fluid in an Eulerian mesh cell as a fluid element on which body and surface force may be computed, in a manner completely analogous to a Lagrangian calculation. The two methods differ, however, in the manner in which the fluid elements are moved to next positions after their new velocities have been computed. The grid simply moves with the computed ele-

ment velocities in the Lagrangian case, while it is necessary to compute the flow of fluid through the mesh in an Eulerian calculation. This *convective flux calculation* requires to average the flow properties of all fluid elements that are in a given mesh cell after a period of time: this averaging process, inherent in convective flux approximations, is the biggest drawback of Eulerian methods. Convective averaging results in a smoothing of all variations in flow quantities, and, in particular, in a smearing of discontinuity surfaces such as free surfaces. The only way to overcome this loss in resolution for free boundaries is to introduce some special treatment that recognizes a discontinuity and avoids averaging across it.

Eight function, *marker particles* and *line segment* are some of the attempts that have been proposed, among others, with the aim of solving this problem, and the VOF theory has come out to be one of the most successful [32].

7.2 The VOF model theory

Define a function α whose value is unity at any point occupied by fluid and zero otherwise. The average value of α in a cell would then represent the fractional volume of the cell occupied by fluid. In particular, a unit value of α would correspond to a cell full of fluid, while a zero value would indicate that the cell contains no fluid. Cells with α values between zero and one must then contain an interface, and so a free surface.

The normal direction to this boundary interface lies in the direction in which the value of α changes most rapidly. Because α is a step function, however, its derivatives must be computed in a special way, as it will be described below: when properly computed, the derivatives can then be used to determine the boundary normal. Finally, when both the normal direction and the value of α in a boundary cell are known, a line cutting the cell can be constructed approximating the interface there. This boundary location can then be used in setting boundary conditions according to the flow field values in that point.

In a Lagrangian mesh, α remains constant in each cell: in this case, α serves solely as a flag identifying cells that contain fluid. While in an Euler-Euler mesh, the flux of α moving with the fluid through a cell must be computed although, as noted in previous Section 7.1, standard finite-difference approximations would lead to a smearing of the α function and interfaces would lose their definition: *interpolation schemes near the interface* are flux approximations which allow to preserve the discontinuous nature of function α avoiding the smearing of interfaces; they will be described more in detail in Section 7.3.5.

Moreover, since the VOF method requires only one storage word for each mesh cell, its storage requirements are lower compared with other methods such as the *marker particle*.

Thus, the VOF method provides a simple and economical way to track free

boundaries in two or three-dimensional meshes.

7.3 The Driving Equations

7.3.1 Volume Fraction equation

The solution of a continuity equation for the volume fraction of one (or more) of the phases is needed in order to accomplish the tracking of the interfaces between the phases. For the i^{th} phase, this can be written as:

$$\frac{1}{\rho_i} \cdot \left[\frac{\partial \, \alpha_i \rho_i}{\partial t} + \nabla \cdot (\alpha_i \rho_i \, \mathbf{v}) = S_{\alpha_i} + \sum_{i=1}^{n} (\dot{m}_{ij} - \dot{m}_{ji}) \right] \tag{7.1}$$

where $\dot{m}_{ij}$ is the mass transfer from phase i to phase j, $\dot{m}_{ji}$ is the mass transfer from j to i and the term S_{α_i} is a user defined further mass source term set to zero by default.

The volume fraction equation will not be solved for the primary phase; the primary-phase volume fraction is simply computed based on the constraint that the volume fractions must sum to one

$$\sum_{i=1}^{n} \alpha_i = 1$$

i.e. the cell is always completely filled.

Once the volume fraction in each cell has been calculated, by means of *interpolation schemes* (see Section 7.3.5) it is then possible to trace the shape of the interface between phases.

The volume fraction equation may be solved either through implicit or explicit time discretization.

The Implicit Scheme

The following equation is employed in order to calculate the volume fraction in each cell at every time step (or iteration if a steady-state solution is performed):

$$\frac{\alpha_i^{n+1} \rho_i^{n+1} - \alpha_i^n \rho_i^n}{\Delta t} V + \sum_f \left(\rho_i^{n+1} \, U_f^{n+1} \alpha_{i,f}^{n+1} \right) = \left[S_{\alpha_i} + \sum_{i=1}^{n} (\dot{m}_{ij} - \dot{m}_{ji}) \right] V \tag{7.2}$$

where $n+1$ refers to the actual time step, n refers to the previous calculated time step, V is the cell volume, $\alpha_{i,f}$ if the face value of the i^th volume fraction, U_f is the volume normal flux through the face.

Since in the second term appears the volume fraction at the current time step $\alpha_{i,f}^{n+1}$, a standard scalar transport equation is solved iteratively for each of the secondary-phase volume fractions at each time step.

The implicit scheme can be used for both time-dependent and steady-state calculations: the previous equation is applied for every iteration instead of time step in this latter case.

The Explicit Scheme

In the explicit scheme there is no need of iterative solution of the transport equation during each time step, as is needed for the implicit scheme, and the following equation is used:

$$\frac{\alpha_i^{n+1}\rho_i^{n+1} - \alpha_i^n \rho_i^n}{\Delta t} V + \sum_f \left(\rho_i \, U_f^n \alpha_{i,f}^n\right) = \left[S_{\alpha_i} + \sum_{i=1}^{n} (\dot{m}_{ij} - \dot{m}_{ji})\right] V \tag{7.3}$$

Just a time-dependent solution can be calculated in this case. Furthermore, this scheme, together with the geometric reconstruct or donor-acceptor scheme (see Section 7.3.5) is suggested by FLUENT® user's guide in order to simulate jet breakup: it will be selected during simulations in the present work because of this fact, as later explained.

7.3.2 Physical properties

The physical properties employed in the transport equations are determined by weighting the physical properties of the phases occupying each control volume. In a two-phase system, referring to the primary and secondary phase by the subscripts 1 and 2 and with the volume fraction of the secondary phase being tracked, the density in each cell, for example, is given by

$$\rho = \alpha_2 \cdot \rho_2 + (1 - \alpha_2) \cdot \rho_1 \tag{7.4}$$

which, in the general case of a n-phase system, leads to the following general form for the volume-fraction-averaged density:

$$\rho = \sum_{i=1}^{n} \alpha_i \cdot \rho_i \tag{7.5}$$

All other physical properties, such as viscosity, are defined exactly the same way.

7.3.3 Momentum equation

A single momentum equation is solved throughout the domain and the resulting velocity field is shared among the phases. The momentum equation, shown below, is dependent on the volume fractions of all phases through the properties ρ and μ calculated as presented in the previous Section 7.3.2:

$$\frac{\partial(\rho\,\mathbf{v})}{\partial t} + \nabla\cdot(\rho\,\mathbf{vv}) = -\nabla p + \nabla\cdot\left[\mu\left(\nabla\mathbf{v} + \nabla\mathbf{v}^T\right)\right] + \rho\mathbf{g} + \mathbf{F} \tag{7.6}$$

It is possible to calculate the velocity field of the mixture, by solving this equation.

7.3.4 Energy equation and additional scalar equations

If introduced in the calculations, also the energy equation is shared among all the phases through the properties ρ and μ, calculated as presented in the previous Section 7.3.2:

$$\frac{\partial(\rho\,E)}{\partial t} + \nabla\cdot\left(\mathbf{v}(\rho\,E + p)\right) = \nabla\cdot\left(k_{eff}\,\nabla T\right) + S_h \tag{7.7}$$

where k_{eff} is the effective thermal conductivity which is another shared volume-fraction-averaged variable like ρ; the source term S_{h} contains contributions from radiation as well as any other volumetric heat sources and can be user-defined. Moreover, energy E is treated as a mass-averaged variables

$$E = \frac{\sum_{i=1}^{n}(\alpha_i\,\rho_i\,E_i)}{\sum_{i=1}^{n}\alpha_i\,\rho_i} \tag{7.8}$$

and similarly it happens for temperature T.

Depending the problem definition, additional scalar equations may be involved as in the case of the presence of turbulence: another single set of transport equations is solved and the turbulence variables (i.e. k and ϵ or the Reynolds stresses) are shared by the phases throughout the field.

7.3.5 Interpolation schemes near the interface

As previously underlined,the introduction of special interpolation schemes is needed to preserve the definition and the discontinuous nature of the boundary interface between phases limiting its smearing effect due to numerical diffusion.

FLUENT®'s control-volume formulation requires the convection and diffusion fluxes through the control volume faces be computed and balanced with source terms within the control volume itself: when a cell is near the interface between two phases (i.e. the volume fraction of a phase is less than 1), the *geometric reconstruction* or *donor-acceptor* interpolation scheme is used in order to reconstruct the behavior of the interface. Figure 7.1 shows comparisons between these two schemes which are also presented below.

The geometric reconstruct scheme

This scheme is based on a interface reconstruction method using a piecewise-linear approach and is the most accurate method in surface tracking.

It assumes that the interface between two fluids has a linear slope within each cell, and uses this linear shape for calculating the advection of fluid through the cell faces. The first step in this reconstruction scheme is calculating the position of the linear interface relative to the center of each partially-filled cell, based on the information about the volume fraction and its derivatives in the cell. The second step is calculating the advecting amount of fluid through each face using the computed linear interface representation and information about the normal and tangential velocity distribution on the face. The third step is calculating the volume fraction in each cell using the balance of fluxes calculated during the previous step.

The donor acceptor scheme

This scheme is based on a finite volume discretization method which identifies one cell as a donor of an amount of fluid from one phase and another (neighbor) cell as the acceptor of the same amount of fluid, and is used to prevent numerical diffusion at the interface. The amount of fluid from one phase that can be convected across a cell boundary is limited by the minimum of two values: the filled volume in the donor cell or the free volume in the acceptor cell. The orientation of the interface is also used in determining the face fluxes. The interface orientation is either horizontal or vertical, depending on the direction of the volume fraction gradient of the i^{th} phase within the cell, and the one of the neighbor cell that shares the considered face.

7.4 Additional Models

When two or more phases are present, surface tension and wall adhesion effects cannot be negligible: this two physical phenomena act directly on the inter-

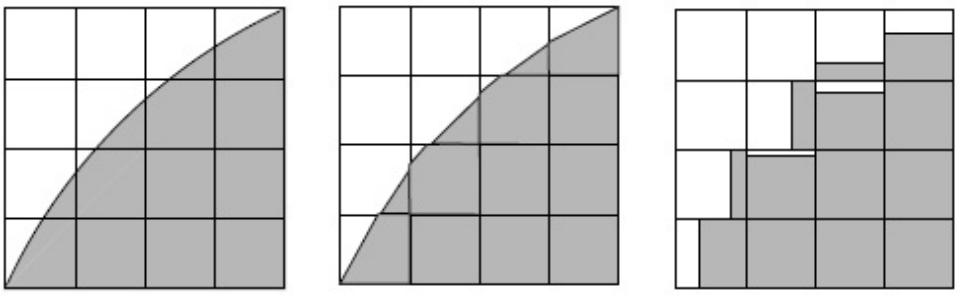

(a) *Actual interface shape* **(b)** *Geometric reconstruct scheme* **(c)** *Donor-acceptor scheme*

Figure 7.1: *Comparison between interpolation schemes near an interface [21]*

face between phases and so it could be necessary to insert their effects during calculations, especially if the aim is correctly tracking the surface shape.

7.4.1 Surface Tension

The physical definition of surface tension s is presented in Section 3.1.1.

The surface tension model in FLUENT® is the continuum surface force (CSF) model proposed by Brackbill *et al.* [33]. With this model, the addition of surface tension to the VOF calculation results in a source term in the momentum equation. The surface curvature is computed from local gradients in the surface normal at the interface. Let $\mathbf{n}$ be the surface normal, defined as the gradient of the i^{th} phase volume fraction α_i:

$$\mathbf{n} = \nabla \alpha_i \tag{7.9}$$

the curvature κ is defined in terms of the divergence of the unit normal $\hat{\mathbf{n}}$

$$\kappa = \nabla \cdot \hat{\mathbf{n}} \tag{7.10}$$

where

$$\hat{\mathbf{n}} = \frac{\mathbf{n}}{|\mathbf{n}|} \tag{7.11}$$

The surface tension can then be written in terms of the pressure jump across the surface. The force at the surface can be expressed as a volume force using the divergence theorem and is then added to the momentum equation as additional source term; in case of two interacting phases, the expression of the force has the following form:

$$F_{\text{vol}} = s_{ij} \frac{\rho \, \kappa_i \, \nabla \alpha_i}{1/2(\rho_i + \rho_j)} \tag{7.12}$$

where ρ is the volume-fraction-averaged density computed with Equation (7.5). Equation (7.12) shows that the surface tension source term for a cell is proportional to the average density in the cell.

Surface tension will be employed in the present model (see Section 12.2) since it turns out to be a a crucial parameter. When taking this model into account, it is useful to remember that the calculation of surface tension effects on triangular and tetrahedral meshes is not as accurate as on quadrilateral and hexahedral meshes. The region where surface tension effects are most important should therefore be meshed with quadrilaterals or hexahedra.

When Consider Surface Tension Effects Some dimensionless parameters can help in establishing whether the effects of surface tension are significant or not. When $Re \ll 1$, the quantity of interest is the *capillary number* Ca

$$Ca = \frac{\mu \, U}{s}$$

while if $Re \gg 1$, the quantity to be considered is the *Weber number*

$$We = \frac{\rho\, L\, U^2}{s}$$

where U is the free-stream velocity.

Surface tension effects can be generally neglected if $Ca \ll 1$ or $We \gg 1$.

7.4.2 Wall Adhesion

It is usual to consider wall adhesion effects by referring to the *contact angle* θ, which is the angle between the wall and the tangent to the interface at the wall, measured inside the drop which is sticked onto the wall, as shown in Figure 7.2.

The value of θ is strongly dependent on the nature of the two interacting phases and the wall as well. In case of drops of water immersed in air and sticked on a steel wall, the contact angle is around 76° [34].

In FLUENT®, the implemented model for wall adhesion is taken from work done by Brackbill *et al.* [33] as well. Rather than imposing this boundary condition at the wall itself, the contact angle that the fluid is assumed to make with the wall is used to adjust the surface normal just in cells near the wall. This so-called dynamic boundary condition results in the adjustment of the curvature of the surface near the wall.

The surface normal at the cell next to the wall can be written as

$$\hat{\mathbf{n}} = \hat{\mathbf{n}}_w \cos\theta + \hat{\mathbf{t}}_w \sin\theta$$

where $\hat{\mathbf{n}}_w$ and $\hat{\mathbf{t}}_w$ are the unit vectors normal and tangential to the wall, respectively. The combination of this contact angle with the surface normal one cell away from the wall determines the local curvature of the surface, and this curvature is used to adjust the body force term in the surface tension calculation.

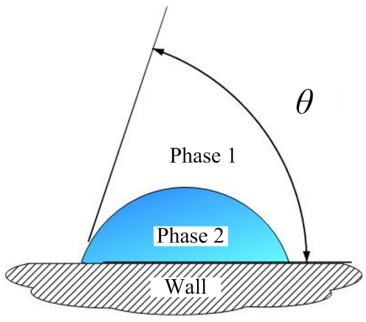

Figure 7.2: *Contact angle definition*

Part II

ANALYTICAL, EXPERIMENTAL AND NUMERICAL ANALYSIS

Chapter 8

Model geometry and nomenclature

The present Section is inserted in order to present and clarify the model geometry, the terms and the nomenclature common to all the following sections; obviously, specific nomenclature regarding each single topic is presented in the related section when necessary.

The orifice tested in the present study is a typical orifice employed in PWJ applications as the one shown in Figure 8.1a.

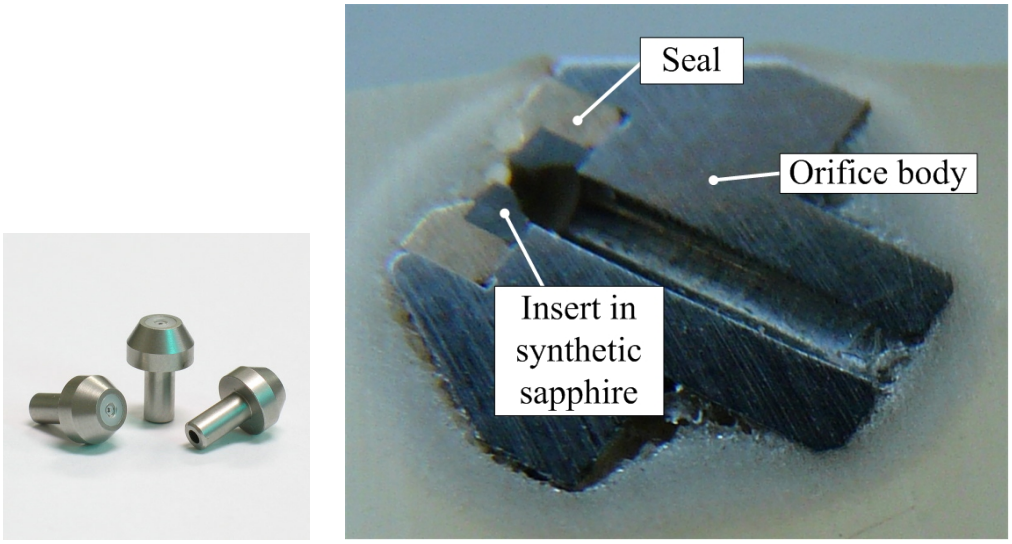

(a) *PWJ orifices (www.gattiam.com).*

(b) *AWJ orifice sectioned by means of grinding and polishing.*

Figure 8.1: *Typical PWJ orifice and section of an AWJ orifice.*

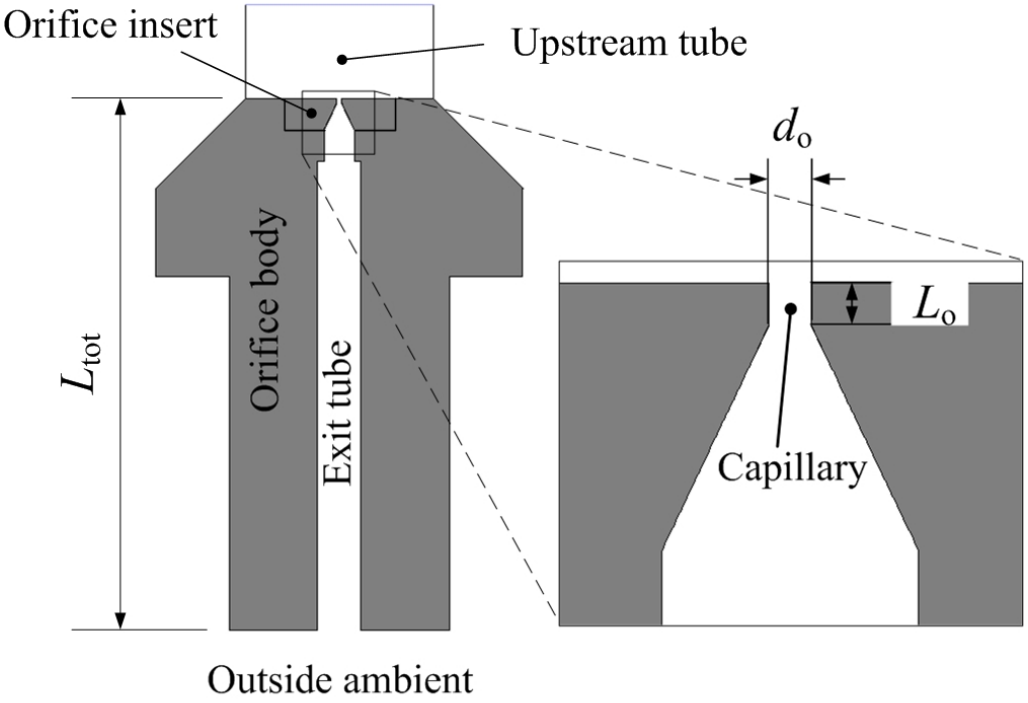

Figure 8.2: *Orifice nomenclature employed throughout the present work*

The regions that schematically make up an orifice are presented in Figure 8.2 and are briefly listed below:

Upstream tube: this is the pipe feeding the orifice with high-pressure water. It is also known as *collimation tube*.

Orifice body: this is the body of the orifice, usually made of stainless steel.

Orifice insert: This is the part where the orifice hole is machined. It is generally made of synthetic sapphire or, occasionally, in diamond, and it is housed with a centering seal in the orifice body as shown for example in Figure 8.1b.

Capillary: this is the small cylindrical hole machined in the orifice insert and namely the core of the jet creation.

Exit tube: this is the wider hole of the orifice body downstream the capillary.

The total length of the orifice is called L_{tot}, while the specific dimensions of the capillary are respectively d_o for the diameter (which is also the nominal value for the orifice) and L_o for the capillary length.

Finally, the geometric dimensions of the orifice tested and the domain of the model employed for numerical simulations are reported in Figure 8.3.

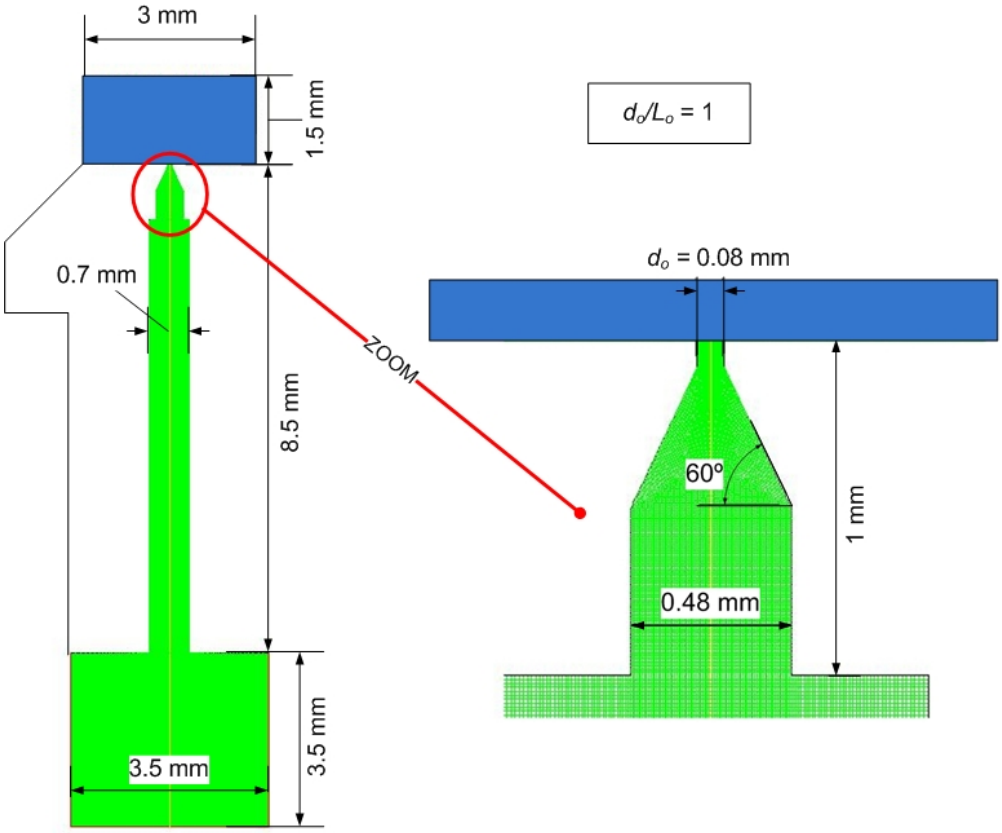

Figure 8.3: *Geometrical dimensions of the tested PWJ orifice model.*

Chapter 9

Jet Stability: single phase, cavitating and flipped nozzles

This is the first chapter giving a deep insight into the mechanisms of jet breakup and the conditions for its stability. Firstly, a theoretical background is presented and later, based on the former, an analysis is performed on the stability of a typical pure water jet in steady conditions.

9.1 Theoretical background

According to the traditional definition, the process of rupturing the liquid by a decrease of pressure at constant temperature is called cavitation. This is a crucial phenomenon in liquid jets breakup and a lot of works have been published in literature on this topic, especially relating it to spray and atomization theory in the field of injectors [3].

Theoretically, as general criterion, the initiation of cavitation happens when the pressure of the liquid goes below its vapor pressure, but it is not unusual to see this phenomenon starting at slightly higher pressures as well. Dabiri *et al.* [9] proposed a new method where the significant parameter in cavitation is the *total stress* which includes both pressure and viscous stresses: this parameter is able to explain the occurrence of cavitation even at pressures higher than the vapor pressure; anyway the relative difference between the first and the second criterion tends to decrease significantly as Reynolds number increases.

As resumed in Figure 9.1, depending on its geometry and working conditions, a sharp-edged plain orifice as the ones used in water jet applications, can basically undergo two different flow regimes, cavitating and hydraulic flipped, while the presence of a significant edge fillet radius r_{ed} can possibly lead to a single-phase

regime too [21].

Several studies have been performed on the breakup mechanisms of water jets produced by different types of orifices at relatively low pressures (up to 20 MPa): Ohnesorge [1] proposed a stability number named after him as Ohnesorge number *Oh*, able to determine the different modes of jet breakup depending on the characteristic *Re* of the flow under the hypothesis of rounded-edge orifice exhibiting a single-phase like flow regime (Figure 9.1). According to his analysis, these kinds of orifices working at high *Re* similar to the ones reached in water jet cutting, would produce a completely atomized jet [6] which is evidently not suitable for typical WJ applications. Furthermore, it is well known from the *spray and atomization theory* that spray cone angles in nozzles likely to cavitate are always wider than the ones in cavitation-free nozzles: in fact the cavitation enhances the mass flow rate fluctuations with the consequence of intensifying the unsteadiness of the jet and its atomization [8]. As a consequence, if the target is obtaining a coherent and stable jet, single-phase and cavitating regime must be avoided and a so called *constricted* or *flipped* [35] water jet must be obtained: the geometry of the nozzle and the operating conditions such as the upstream and downstream pressures are crucial parameters to achieve this condition. In the case of a constricted jet, the jet is a collimated beam of momentum as it is detached from the capillary walls and stays therefore laminar for a wider range of velocities exhibiting a much longer breakup length as compared to non-constricted water jet at the same conditions [7]. The cavitation number K is an essential parameter to predict the inception of cavitation:

$$K = \frac{p_{\mathrm{up}} - p_{\mathrm{v}}}{p_{\mathrm{up}} - p_{\mathrm{down}}} \tag{9.1}$$

where p_{up} is the upstream working pressure p_{down} is the pressure downstream the capillary and p_{v} is the vapor pressure of water. Defining the Reynolds

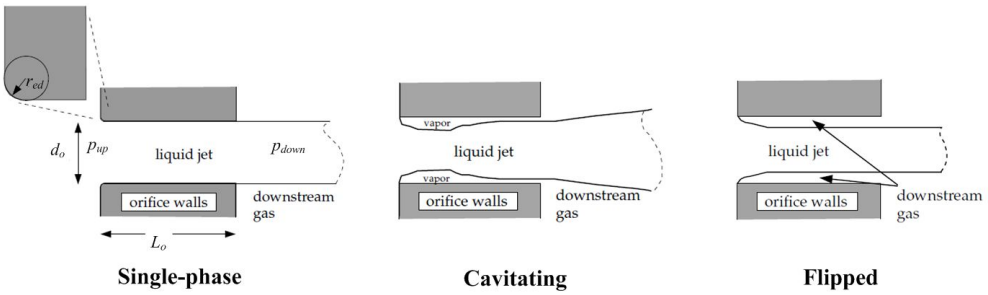

Figure 9.1: *Possible flow regimes in a plain orifice [21]*

number modified on hydraulic head as

$$Re_{\mathrm{h}} = \frac{d_{\mathrm{o}}\,\rho_{\mathrm{w}}}{\mu} \cdot \sqrt{\frac{2(p_{\mathrm{up}} - p_{\mathrm{down}})}{\rho_{\mathrm{w}}}}$$

the critical values for the inception of cavitation and hydraulic flip are respectively K_{cav} and K_{flip}, empirically defined as follows:

$$K_{\mathrm{cav}} = 1.9\left(1 - \frac{{r_{\mathrm{ed}}}^2}{d_{\mathrm{o}}} - \frac{1000}{Re_{\mathrm{h}}}\right) \tag{9.2}$$

$$K_{\mathrm{flip}} = 1 + \frac{1}{\left(1 + \frac{L_{\mathrm{o}}}{4d_{\mathrm{o}}}\right)\left(1 + \frac{2000}{Re_{\mathrm{h}}}\right)\mathrm{e}^{70\,r_{\mathrm{ed}}/d_{\mathrm{o}}}} \tag{9.3}$$

It is then possible to predict the flow regime inside the orifice by comparing K with K_{cav} and K_{flip} according to the following scheme [21] and Figure 9.2:

- $K > K_{\mathrm{cav}}$ and $K \geq K_{\mathrm{flip}}$: single-phase regime;
- $K_{\mathrm{flip}} \leq K < K_{\mathrm{cav}}$: cavitating regime;
- $K \lesseqgtr K_{\mathrm{cav}}$ and $K < K_{\mathrm{flip}}$: hydraulic flipped regime.

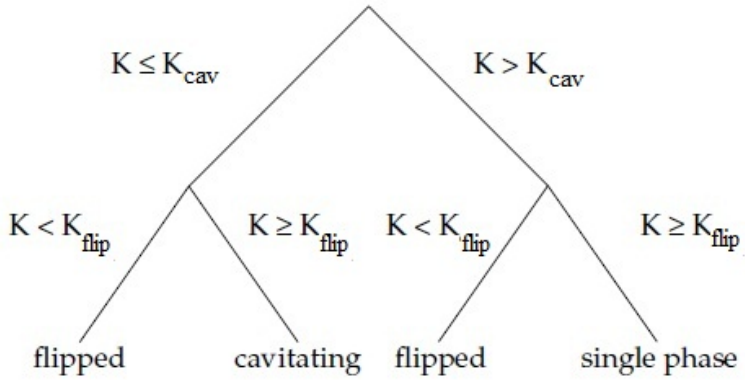

Figure 9.2: *Decision tree for the flow regime definition [21].*

As consequence, the coherence and stability of the jet produced by each orifice is strongly dependent on the evolving flow regime.

9.2 Analysis of the flow regime inside a pure water jet orifice

By exploiting Equations (9.1)(9.2)(9.3), it is possible to analyze the flow regime developing inside a typical orifice used in PWJ applications and point out the

influence of geometry and working conditions on the coherence of the jet. Firstly, in order to analyze the geometric effects, the working conditions are kept constant and just the geometrical dimensionless parameters r_{ed}/d_o and L_o/d_o are varied; Table 9.1 summarizes the employed parameters, while Table 9.2 and Table 9.3 report the obtained results.

d_o (mm)	p_{up} (MPa)	p_{down} (Pa)	p_v (Pa)	ρ_w (kg/m^3)	μ (kg/m $\cdot$ s)	r_{ed}/d_o (-)	L_o/d_o (-)
0.08	160	8.50E+04	2400	998.20	1.003E-03	0.05→0.63	0.5→15

Table 9.1: *Constansts employed to study the orifice geometry effects on jet flow regime.*

r_{ed} (mm)	r_{ed}/d_o (-)	L_o (mm)	L_o/d_o (-)	Re_h (-)	K (-)	K_{cav} (-)	K_{flip} (-)	Regime
4.00E-03	0.05	0.08	1	4.51E+04	1.00052	1.69256	1.02313	FL
4.80E-03	0.06	0.08	1	4.51E+04	1.00052	1.64773	1.00964	FL
6.40E-03	0.08	0.08	1	4.51E+04	1.00052	1.60350	1.00402	FL
8.00E-03	0.10	0.08	1	4.51E+04	1.00052	1.51681	1.00070	FL
8.80E-03	0.11	0.08	1	4.51E+04	1.00052	1.47436	1.00029	CAV
1.04E-02	0.13	0.08	1	4.51E+04	1.00052	1.43250	1.00012	CAV
2.00E-02	0.25	0.08	1	4.51E+04	1.00052	1.04656	1.00000	CAV
5.04E-02	0.63	0.08	1	4.51E+04	1.00052	0.24500	1.00000	S.P.
FL = Flipped, CAV = Cavitating, S.P. = Single Phase								

Table 9.2: *Results obtained with p_{up} =160 MPa, r_{ed}/d_o variable and L_o/d_o fixed to 1*

r_{ed} (mm)	r_{ed}/d_o (-)	L_o (mm)	L_o/d_o (-)	Re_h (-)	K (-)	K_{cav} (-)	K_{flip} (-)	Regime
6.40E-03	0.08	0.04	0.5	4.51E+04	1.00052	1.58597	1.00315	FL
6.40E-03	0.08	0.06	0.7	4.51E+04	1.00052	1.58597	1.00301	FL
6.40E-03	0.08	0.08	1.0	4.51E+04	1.00052	1.58597	1.00283	FL
6.40E-03	0.08	0.12	1.5	4.51E+04	1.00052	1.58597	1.00258	FL
6.40E-03	0.08	0.20	2.5	4.51E+04	1.00052	1.58597	1.00218	FL
6.40E-03	0.08	0.40	5.0	4.51E+04	1.00052	1.58597	1.00157	FL
6.40E-03	0.08	0.56	7.0	4.51E+04	1.00052	1.58597	1.00129	FL
6.40E-03	0.08	0.80	10.0	4.51E+04	1.00052	1.58597	1.00101	FL
6.40E-03	0.08	1.20	15.0	4.51E+04	1.00052	1.58597	1.00075	FL
FL = Flipped, CAV = Cavitating, S.P. = Single Phase								

Table 9.3: *Results obtained with p_{up} =160 MPa, L_o/d_o variable and r_{ed}/d_o fixed to 0.8*

Parameters d_o and p_{up} are set to typical values used in common PWJ cuttings and are kept the same along the whole present study; besides, the value of p_{down}

is taken from previous simulations and is set to a lower value than atmospheric pressure.

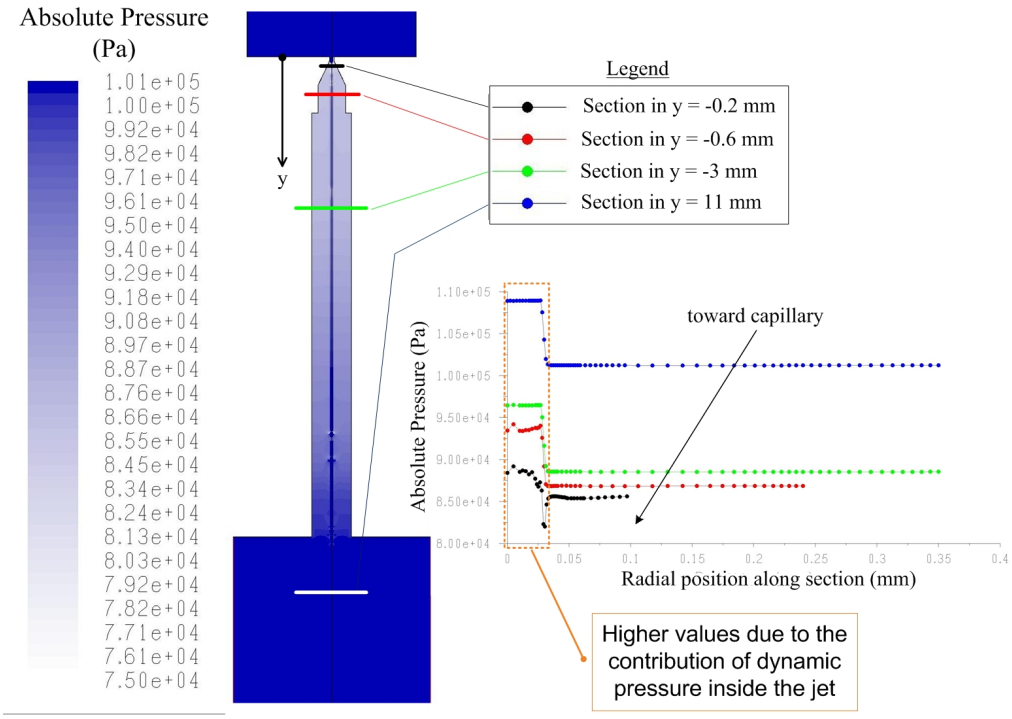

Figure 9.3: *Pressure drop inside orifice tube*

Figure 9.3 depicts clearly how pressure drops moving upward from the exit tube to the capillary due to the high velocity field created by the main jet: section closer to the capillary have a lower pressure value and the closest section considered (y = -0.2 mm) has a value of about 8.50E+04 Pa which is exactly the setup value for p_{down}. Note that the first part of the plot in Figure9.3 is characterized by higher values due to the contribution of the dynamic pressure of the jet (this part of the graph is in fact around 0.03 mm wide which is exactly the radius of the jet as it will be presented later); except for this part, the rest of the plot refers to pressure values around the jet. The ratios L_o/d_o and r_{ed}/d_o are subsequently kept constant to separately investigate on each one of them: respectively, L_o/d_o is fixed to 1 while r_{ed}/d_o to 0.08 which are common values in PWJ orifices. More precisely, Table 9.2 and Figure 9.4a show the influence of r_{ed}/d_o while $L_o/d_o = 1$ is fixed; on the contrary, in Table 9.3 and Figure 9.4b L_o/d_o is the variable and r_{ed}/d_o is fixed to a value of 0.08.

Within the ranges studied in the present work $K \leq K_{cav}$, with the only exception of the last row in Table 9.2 where $K > K_{cav}$ (this case will be later explained): in these conditions the hydraulic flipped regime s occurs when $K < K_{flip}$, as explained before and shown in Figure 9.2. The hydraulic flipped and cavitating

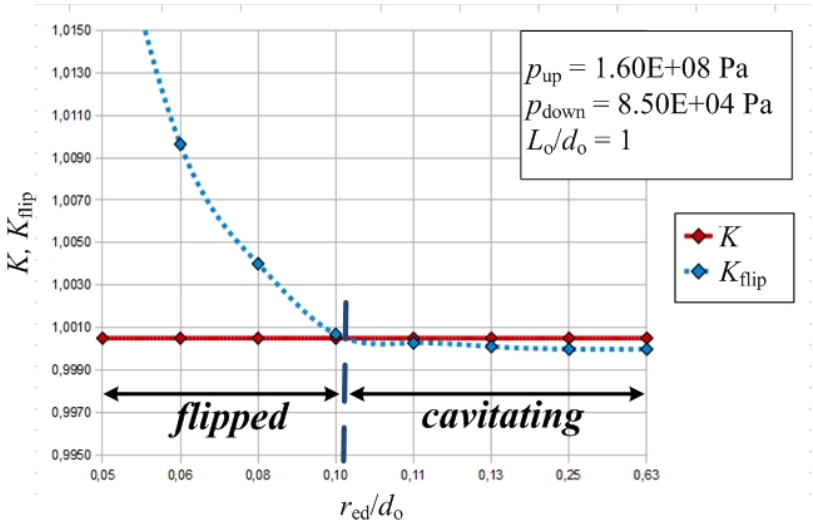

(a) *Influence of r_{ed}/d_o on K and K_{flip} with p_{up}=160 MPa*

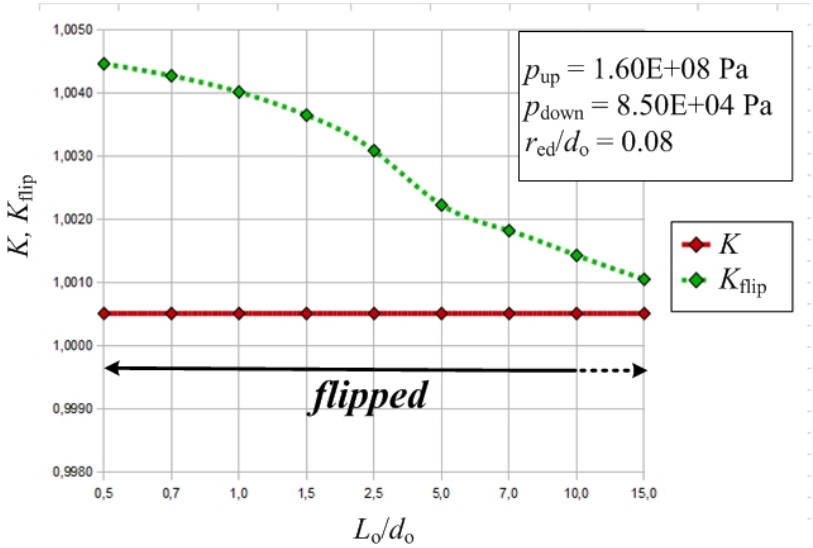

(b) *Influence of L_o/d_o on K and K_{flip} with p_{up}=160 MPa*

Figure 9.4: *Influence of orifice geometry on flow regime*

regions are marked directly on the graphs: it is possible to notice how cavitation only affects orifices with high r_{ed}/d_o and L_o/d_o ratios, namely orifices with large edge rounding and large capillary length compared to orifice diameter [11]. Referring to Figure 9.4b it is also noticeable that the regime still remains flipped, even with L_o/d_o up to 15: this fact happens because the relatively sharp edge forces the main water flow to follow a curved path and detach from the capillary walls creating a constricted jet, while the very high pressure transfers to the jet a huge amount of energy (converted in momentum) pushing the reattachment point responsible for cavitation further away, outside the capillary, and assuring the hydraulic flip anyway.

Moreover, the same analysis is done again with a lower upstream pressure p_{up} in order to analyze the effect of the working conditions; the new conditions are reported in Table 9.4 while Table 9.5 and Figure 9.5a together with Table 9.6 and Figure 9.5b show the results.

d_o (mm)	p_{up} (Pa)	p_{down} (Pa)	p_v (Pa)	ρ_w (kg/m^3)	μ (kg/m $\cdot$ s)	r_{ed}/d_o (-)	L_o/d_o (-)
0.08	2.00E+7	8.50E+04	2400	998.20	1.003E-03	0.05→0.63	0.5→15

Table 9.4: *Parameters employed to study working conditions effects on jet flow regime*

r_{ed} (mm)	r_{ed}/d_o (-)	L_o (mm)	L_o/d_o (-)	Re_h (-)	K (-)	K_{cav} (-)	K_{flip} (-)	Regime
4.00E-03	0.05	0.08	1	1.59E+04	1.00415	1.65187	1.02146	FL
4.80E-03	0.06	0.08	1	1.59E+04	1.00415	1.61596	1.01066	FL
6.40E-03	0.08	0.08	1	1.59E+04	1.00415	1.54528	1.00263	CAV
8.00E-03	0.10	0.08	1	1.59E+04	1.00415	1.47612	1.00065	CAV
8.80E-03	0.11	0.08	1	1.59E+04	1.00415	1.44211	1.00032	CAV
1.04E-02	0.13	0.08	1	1.59E+04	1.00415	1.37523	1.00008	CAV
2.00E-02	0.25	0.08	1	1.59E+04	1.00415	1.00587	1.00000	CAV
5.04E-02	0.63	0.08	1	1.59E+04	1.00415	0.19723	1.00000	S.P.

FL = Flipped, CAV = Cavitating, S.P. = Single Phase

Table 9.5: *Results obtained with p_{up} =20 MPa, r_{ed}/d_o variable and L_o/d_o fixed to 1*

Reducing the difference between upstream and downstream pressure by lowering p_{up} of about one order of magnitude, the situation dramatically changes: comparing Figure 9.5a to Figure 9.4a and Figure 9.5b to Figure 9.4b respectively, it is clear how the orifice is much more likely to cavitate as the cavitating range is much wider and occurs for lower values of r_{ed}/d_o and L_o/d_o. In particular, comparing Figure 9.4b to Figure 9.5b the effects are more evident: in case of high pressure p_{up} = 160 MPa (Figure 9.4b), the regime is always flipped within the considered range, while Figure 9.5b shows how reducing p_{up} to 20 MPa and

r_{ed} (mm)	r_{ed}/d_o (-)	L_o (mm)	L_o/d_o (-)	Re_h (-)	K (-)	K_{cav} (-)	K_{flip} (-)	Regime
6.40E-03	0.08	0.04	0.5	1.59E+04	1.00415	1.54528	1.00292	CAV
6.40E-03	0.08	0.06	0.7	1.59E+04	1.00415	1.54528	1.00280	CAV
6.40E-03	0.08	0.08	1.0	1.59E+04	1.00415	1.54528	1.00263	CAV
6.40E-03	0.08	0.12	1.5	1.59E+04	1.00415	1.54528	1.00239	CAV
6.40E-03	0.08	0.20	2.5	1.59E+04	1.00415	1.54528	1.00202	CAV
6.40E-03	0.08	0.40	5.0	1.59E+04	1.00415	1.54528	1.00146	CAV
6.40E-03	0.08	0.56	7.0	1.59E+04	1.00415	1.54528	1.00119	CAV
6.40E-03	0.08	0.80	10.0	1.59E+04	1.00415	1.54528	1.00094	CAV
6.40E-03	0.08	1.20	15.0	1.59E+04	1.00415	1.54528	1.00069	CAV

FL = Flipped, CAV = Cavitating, S.P. = Single Phase

Table 9.6: *Results obtained with p_{up} =20 MPa, L_o/d_o variable and r_{ed}/d_o fixed to 0.8*

keeping the same r_{ed}/d_o ratio as in the case of Figure 9.4b, the capillary is always in cavitating regime.

Moreover, the sharpness of the orifice edge is surely one of the most important and influent conditions in order to guarantee the hydraulic flip condition as the previous analysis has shown. Progressively increasing the radius of curvature of the orifice edge will inevitably lead to a cavitating flow regime first, and a single phase regime later. The very last rows of Table 9.2 and Table 9.5 refer to conditions of high r_{ed}/d_o ratio, i.e. relatively high r_{ed}, and it is noticeable that even with high upstream pressure, the regimes turns out to be single phase in any case.

A classical representation of the main breakup mechanisms which take place in rounded edge nozzles is based on the Ohnesorge-Reynolds diagram, shown in Figure 9.6. *Oh* is a dimensionless number also called "stability number" that relates the viscous forces to inertial and surface tension forces; jet velocity is not explicitly present, so *Oh* is an indicator of the jet stability taking into account orifice geomerty (d_o). It is defined as

$$Oh = \frac{\sqrt{We}}{Re} = \frac{\mu}{\sqrt{\rho\, d_o\, s}} \tag{9.4}$$

The first Ohnesorge classification of flow regimes [1] has been integrated by other researcher over the last decades [3, 36] who marked the different breakup regions (dripping, Rayleigth, first and second wind induced and atomization [36]) on the *Oh*-*Re* diagram represented in Figure 9.6.

M. Annoni *et al.* [6] showed that commonly employed WJ orifices stably lay in the "atomization region" according to Ohnesorge classification; the red dot in Figure 9.6 refers to the tested PWJ orifice, which is also representative of typical WJ orifices. Anyway, hydraulic flipped conditions in WJ orifices produce

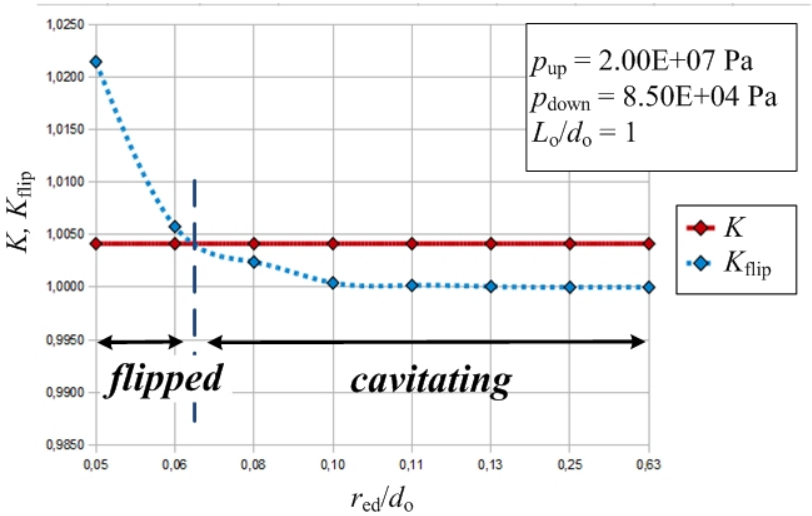

(a) *Influence of r_{ed}/d_o on K and K_{flip} with p_{up}=20 MPa*

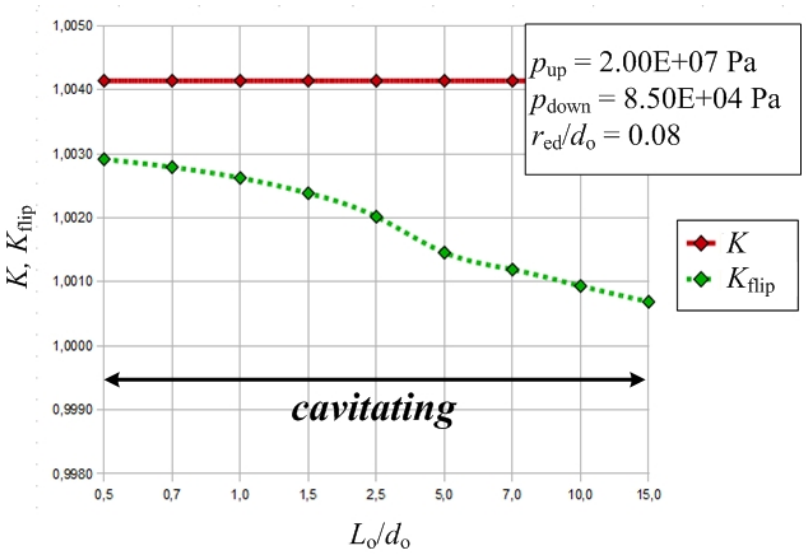

(b) *Influence of L_o/d_o on K and K_{flip} with p_{up}=20 MPa*

Figure 9.5: *Influence of working conditions on flow regime*

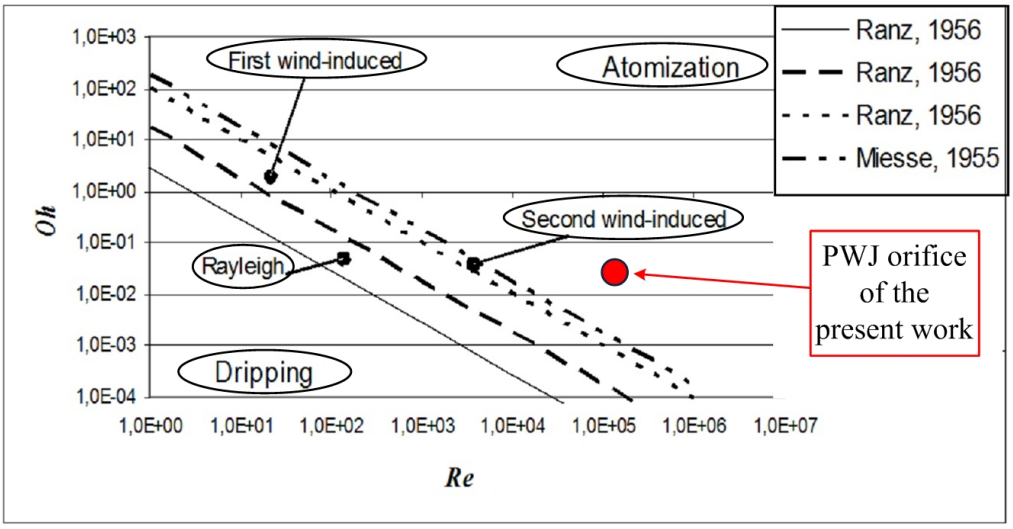

Figure 9.6: *Ohnesorge diagram [1, 3, 6]; tested orifice conditions are indicated by the red dot.*

constricted water jets which evidently are not atomized jets. As a consequence, it can be inferred that constricted water jets do not follow the classification proposed by Ohnesorge [37] and orifices can produce a highly coherent jet thanks to the sharp-edge.

In addition, the worst situation among the previously presented is the one referring to Table 9.6 and plotted in Figure 9.5b, since the regime is cavitating within all the studied range: to further underline the influence of edge sharpness, the same situation is now analyzed by lowering the ratio r_{ed}/d_o from 0.08 to 0.06 which means to consider a sharper edge. The results presented in Table 9.7 and

r_{ed} (mm)	r_{ed}/d_o (-)	L_o (mm)	L_o/d_o (-)	Re_h (-)	K (-)	K_{cav} (-)	K_{flip} (-)	Regime
4.80E-03	0.06	0.04	0.5	1.59E+04	1.00415	1.61596	1.01184	FL
4.80E-03	0.06	0.06	0.7	1.59E+04	1.00415	1.61596	1.01134	FL
4.80E-03	0.06	0.08	1.0	1.59E+04	1.00415	1.61596	1.01066	FL
4.80E-03	0.06	0.12	1.5	1.59E+04	1.00415	1.61596	1.00969	FL
4.80E-03	0.06	0.20	2.5	1.59E+04	1.00415	1.61596	1.00820	FL
4.80E-03	0.06	0.40	5.0	1.59E+04	1.00415	1.61596	1.00592	FL
4.80E-03	0.06	0.56	7.0	1.59E+04	1.00415	1.61596	1.00484	FL
4.80E-03	0.06	0.80	10.0	1.59E+04	1.00415	1.61596	1.00381	CAV
4.80E-03	0.06	1.20	15.0	1.59E+04	1.00415	1.61596	1.00280	CAV

FL = Flipped, CAV = Cavitating, S.P. = Single Phase

Table 9.7: *Results for sharpness influence with p_{up} =20 MPa, L_o/d_o variable and r_{ed}/d_o fixed to 0.6*

Figure 9.7 are clear: while in the previous homologous situation presented in

Figure 9.5b the regime is always cavitating, it is almost completely flipped in this case, because of the edge sharpening within the same range of magnitude; this fact demonstrates once more how having a sharp edge at the orifice inlet is crucial to create hydraulic flip and so a better quality jet.

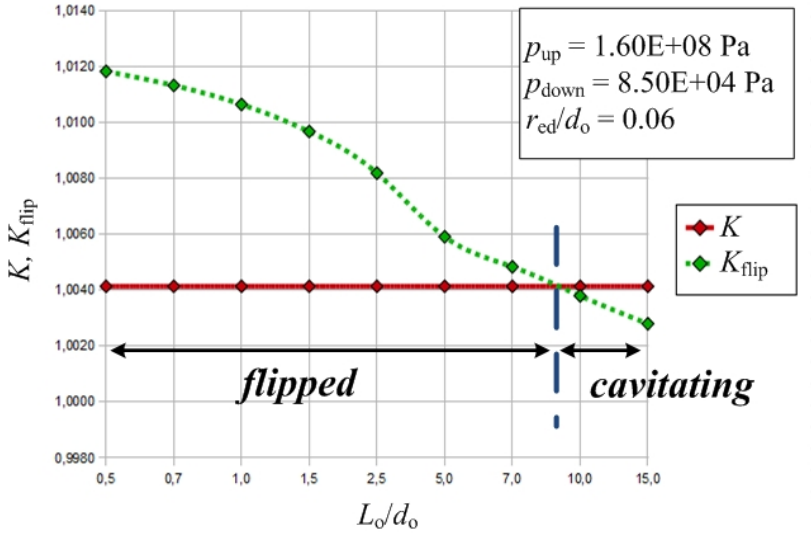

Figure 9.7: *Influence of* L_o/d_o *at* $r_{ed}/d_o = 0.06$ *and* $p_{up} = 160$ MPa

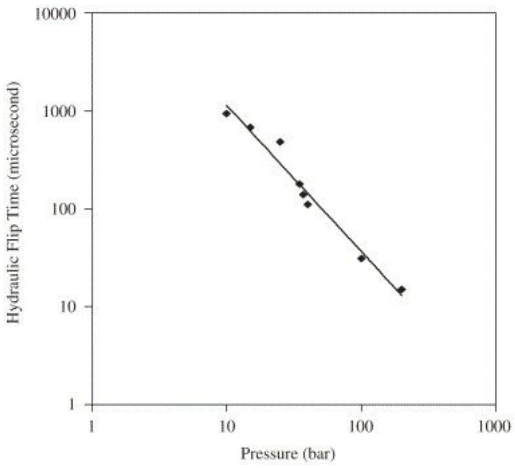

Figure 9.8: *Hydraulic flip time as a function of* p_{up}

Besides, in the very first instants of its creation, it is possible that the forming jet temporary reattaches to the capillary walls enhancing cavitation: this generally happens in orifices with an aspect ratio $L_o/d_o > 0.7$ as it is well described by Basha *et al.* [11] and Anantharamaiah *et al.* [10]. Anyway, this phenomenon is related just to the initial transient of the jet which later develops and reaches its steady flow regime depending on the inner geometry of the capillary and the specific working conditions, as presented before. It is therefore possible that an orifice, initially reattaching or cavitating, later loses this condition switching to a stable hydraulic flip regime, as it exactly happens with pure water jet orifices; Figure 9.8 shows the time taken by the jet to reach the hydraulic flip condition as a function of the upstream pressure [7]: it is evident that the higher the pressure the more rapid the jet is in reaching hydraulic flip since a higher amount of energy and momentum is provided to it.

As a conclusion, this analysis demonstrates that sharp-edged orifices with L_o/d_o close to unit and supplied by very high pressures like the ones commonly used in water jet cutting applications lay in a stable condition of hydraulic flip, which guarantees a constricted jet with high coherence and long breakup lengths. This study exploits consolidated literature spread used in the field of sprays and injectors, but it has never been proposed in literature regarding WJ applications.

Chapter 10

High-Speed Camera analysis

Results reported in Section 9 are generally correct even if they refer to "ideal" steady-state conditions, while the jet is affected also by disturbances in the reality: naked-eye watching a pure water jet, it is possible to notice that it actually stays coherent for most of the time, but sometimes it pulsates, temporarily losing its coherence spreading wider at the exit of the orifice tube and being surrounded by small droplets and vapor; after some whiles, the jet comes back again to a stable condition.

By means of a high speed camera it is possible to dynamically capture the evolving structure of the jet, even if the high velocities and the small dimensions typical of the process often prevent the equipment from getting well focused snapshots capable of catching the inner structure in high-resolution.

10.1 Camera setup and settings

The used model of camera is "FASTCAM-APX RS" by Photron and the setup is presented in Figure 10.1.

Since the camera needs a physical time to save images in memory, rising up the frame rate (i.e. the frequency at which the camera save images), the maximum allowed resolution for a single frame reduces [38]: in the present case, in order to catch important jet dynamics with the highest possible frequency, the frame rate is set to 20000 frames/sec and the resulting maximum allowed resolution is 512x256 pixels which was considered the best compromise. This area is not so big and, as a consequence, the camera is directed so as to allow grabbing images just at the very exit of the orifice tube. Moreover, the higher is the frame rate, the shorter the photographic sensor of the camera stays open, hence at high frame rates the illumination provided to the recording area must be very strong: two powerful halogen lamps on the sides of the jet and a gas

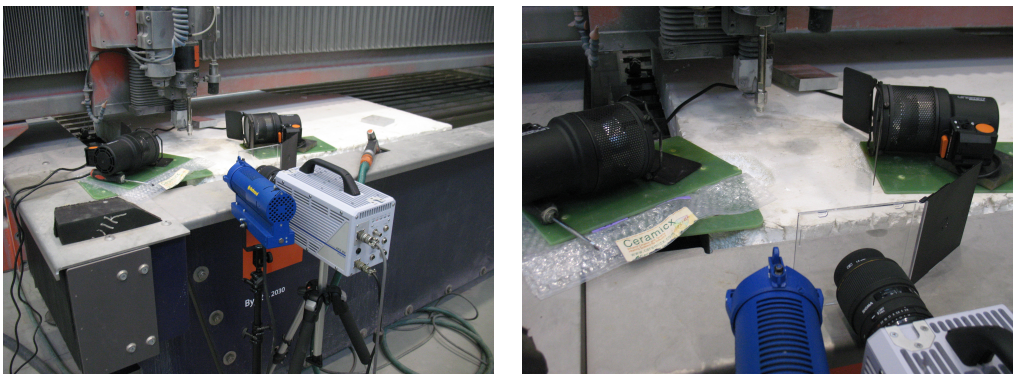

(a) (b)

Figure 10.1: *High Speed Camera setup*

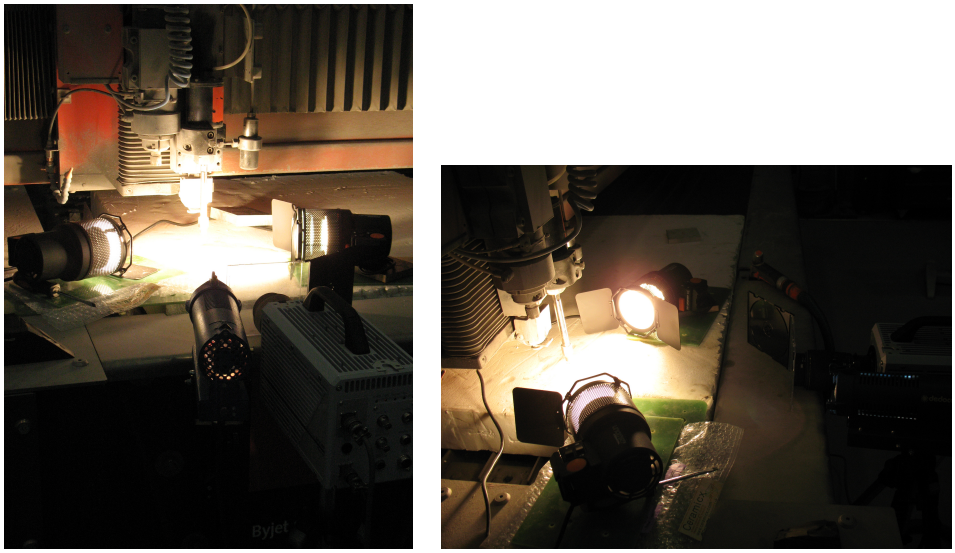

(a) (b)

Figure 10.2: *High Speed Camera in working conditions*

lamp behind the camera are positioned to ensure a correct illumination in this case. Figure 10.2 shows the equipment in working conditions and it is possible to notice that this way, a huge amount of light is provided to the region around the jet.

The PWJ orifice mounted on the cutting head has the same characteristic of the one previously presented in Section 8 with the exception that the total length L_{tot} is 10 mm instead of 8.5 mm.

10.2 High-Speed Camera results

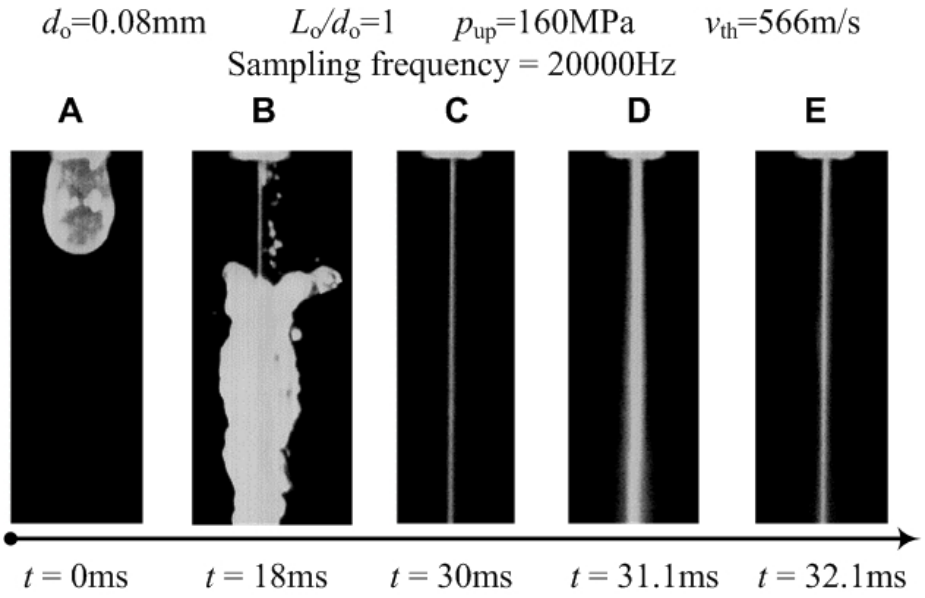

Figure 10.3: *Images of the initial transient acquired by HSC*

One of the most interesting sequence captured with the HSC is reported in Figure 10.3, where it is possible to analyze the evolution of the jet since its creation and point out the phenomenon of "jet pulsation" explained at the beginning of this section: when the jet is off, the inner tube of the orifice is filled with water which remains stuck inside from previous usages and possibly forms drops at the very exit of it (A); as the jet switches on, the air pushed outside by the incoming water flow and the jet itself blows outside the already present water breaking it into smaller droplets (B); later on, the constricted jet is completely formed and stable (C) until suddenly it loses its coherence opening wider in a spray-like manner (D); after some whiles (around 1ms) the jet recovers its stable flipped condition (E). This last phenomenon occasionally happens at irregular frequencies and then it seems not related to systematic irregularities like upstream pressure fluctuations or orifice wear.

However, the analysis made by HSC shows that there is a large presence of still water and droplets inside the orifice tube, especially in the first instants of the jet formation when the jet has not reached steady conditions yet. Furthermore, condensed humidity, jet breakup or jet disturbances can increase the presence of droplets inside the tube during working conditions. The presence of water and droplets inside the orifice tube is identified as a possible cause of jet instability and will therefore be deeper examined.

Chapter 11

Preliminary considerations on the numerical model

The present section will present a series of considerations which have been collected from literature or directly deduced by previous trials, with the aim of developing and designing a coherent numerical model, able to correctly represent all the most important features of a PWJ process.

11.1 Important WJ features to be modeled

When a PWJ process need to be modeled, there are some important physical features to take into account:

Presence of two phases: the PWJ process is characterized by a high velocity jet of water immersed in air as shown in Figure 11.1a. The problem therefore involves two phases and a multiphase model (see Section 6 for details) is necessary.

High *Re***:** characteristic velocities in WJ applications are always very high; in the case of present work, being $d_o = 0.08$ mm and $p_{up} = 160$ MPa, the Reynolds number is:

$$Re = \frac{\rho\, v_{th}\, d_o}{\mu} = \frac{\rho\, \sqrt{\frac{2\, p_{up}}{\rho}}\, d_o}{\mu} = 4.51\ \text{E+04}$$

which is a high value, characteristic of a fully turbulent flow. Even if the jet stays coherent for a longer length despite of the high *Re* (see Section 9), the process must take into account turbulence. A turbulence model (see Section 4.4 for details) must therefore be added to the model.

Surface tension: when considering breakup phenomena and tracking of interfaces, as shown in Figure 11.1b, surface tension is a crucial parameter to take into account in order to properly predict all the forces acting across the surface. Surface tension (see Section 3.1.1 and 7.4.1 for more details) must therefore be considered in the numerical model.

Body forces: as in the present numerical model jet breakup together with creation and motion of droplets inside the orifice are monitored, body forces (i.e. gravity) must be added in order to correctly predict all the forces acting on the fluid.

11.2 Considerations on the time step

When solving an unsteady problem, the choice of the *time step* is crucial for the convergence of the calculations and the correctness of the solution. The time step Δt is the elapsed time between two subsequent calculated instants and generally must be small enough to allow the resolution of the smallest characteristic time scales of the phenomena we are interested in. Moreover, a smaller time step obviously implies smoother variations of the flow field variables which help stability and convergence. Briefly summarizing, on one hand a smaller time step speeds up convergence and improves stability and precision, but on the other hand it leads unavoidably to solve a higher amount of time steps in order to reach the same final flow time. A wise way to judge the choice of Δt is to observe the number of iterations that the solver needs to converge at each time step: the ideal number of iterations per time step is 5-10 [21]. If much more

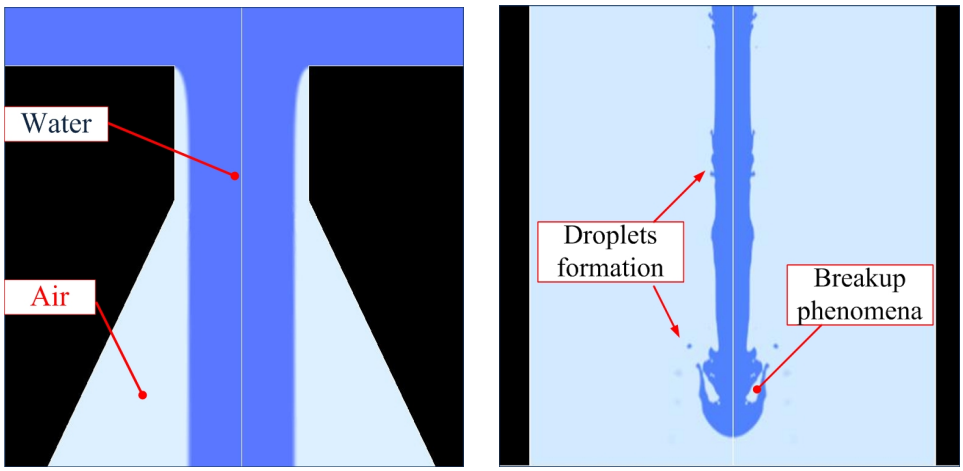

(a) *Two-phase flow in PWJ numerical model.* **(b)** *Jet breakup and droplet formation in PWJ numerical model.*

Figure 11.1: *Important features in PWJ process.*

iterations are needed, the time step is too large, while if the solver needs only a few iterations per time step, Δt may be increased. Frequently a time-dependent problem has a very fast startup transient that decays rapidly. Therefore, it is often wise to choose a conservatively small Δt for the first time steps and later gradually increase it as the calculation proceeds [21].

Anyway, to optimize the choice of the time step it is possible to use one of the *adaptive time stepping* methods implemented in the solver, which allow to have the size of the time step changing as the calculation proceeds, rather than specifying a fixed time step for the entire calculation.

In case of VOF calculations using the "explicit scheme" as in the case of the present study, FLUENT®allows you to use "variable time stepping" based on the definition of Courant number in order to automatically change the time step when an interface is moving through dense cells or if the interface velocity is high. Referring to Figure 11.2 the Courant number Co is a dimensionless number that compares the time step in a calculation to the characteristic time of transit of a fluid element across a control volume:

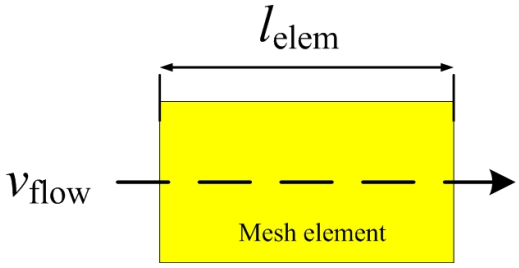

Figure 11.2: *Scheme for the definition of Courant number*

$$Co = \frac{\Delta t}{\frac{l_{\text{elem}}}{v_{\text{flow}}}}$$

In the region near the fluid interface, the solver divides the volume of each cell by the sum of the outgoing fluxes. The resulting time represents the time it would take for the fluid to empty out the cell. The smallest calculated time is used as the characteristic transit time for a fluid element across a control volume, as described below:

$$\Delta t_{\text{global}} = \frac{Co}{\max\left(\sum_{cell} \frac{\text{Outgoing fluxes}}{Cellvolume}\right)} \tag{11.1}$$

Based upon this time and the user-defined input for the maximum allowed Courant number, a time step is computed for using in the VOF calculation. For example, if the maximum allowed Courant number is 0.5, the time step will be

chosen to be at most one-half the minimum transit time for any cell near the interface.

Referring to Figure 11.3, when the "Variable time stepping" option is activated, a control panel allows to adequately setup the process by means of the following options [21]:

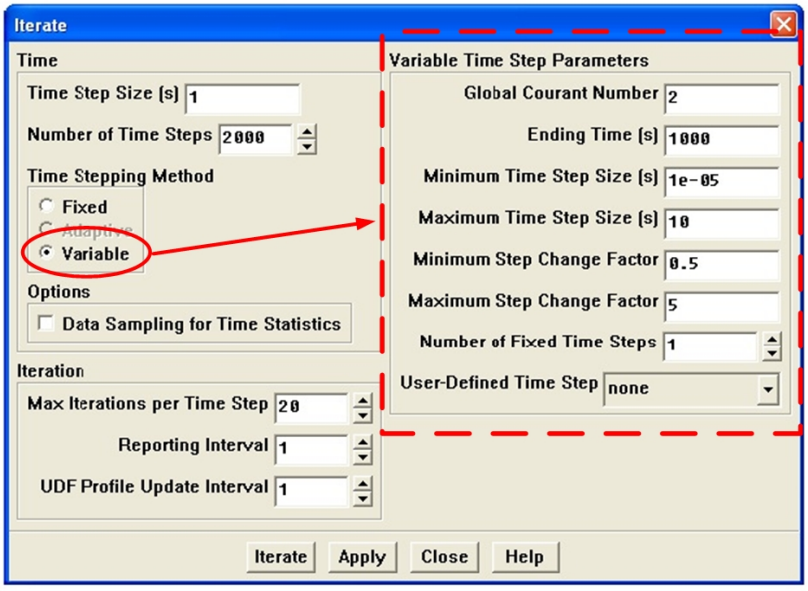

Figure 11.3: *Variable time stepping control panel.*

Courant Number: this is the parameter directly used to determine the actual time step as shown in Equation (11.1).

Ending Time: this specifies explicitly an ending time for the calculation, since the ending time cannot be simply determined by multiplying the number of time steps by a fixed time step size.

Minimum/Maximum Time Step Size: this allows the user to appropriately specify the upper and lower limits for the size of the time step. As already mentioned, if the time step becomes very small, the computational expense may be too high; while if the time step becomes very large, the solution accuracy may not be acceptable.

Minimum/Maximum Step Change Factor: this limits the degree to which the time step size can change at each time step. Limiting the change results in a smoother calculation of the time step size, especially when high-frequency noise is present in the solution.

Number of Fixed Time Steps: this specifies the number of fixed-size time steps that should be performed before the size of the time step is changed. The

size of the fixed time step is the specified value for "Time Step Size" in the "Iterate" panel. It is common to perform a few fixed-size time steps before switching to the variable time stepping: sometimes spurious discretization errors can be associated to an impulsive start. These errors are dissipated during the first few time steps, but they can adversely affect the variable time stepping and result in extremely small time steps at the beginning of the calculation.

In the present model a "variable time stepping" method will be used, as reported in Section 12.2.

11.3 Considerations on the mesh generation

Mesh quality is the crucial parameter for spatial resolution as much as time step is crucial for time resolution. Without any doubts, mesh generation is one of the most important factors to obtain a stable and convergent solution and, above all, correct numerical results. Some basic guidelines on mesh generation have been presented in Section 5.1.1, while this paragraph is added in order to present the main problems encountered during simulations of the present work and the consequent possible adopted solution.

A clear example is reported in Figure 11.4 which shows a typical mesh-dependent inaccuracy encountered during preliminary simulations carried out in the first phases of experimentation. The first developed model has a coarse mesh (Figure 11.4a) and the obtained results show a high-turbulent region concentrated at the exit of the capillary, characterized by high values of turbulent kinetic energy k (maximum value: 1.70 E+06 m^2/s^2), as shown in Figure 11.4b.

Keeping the same geometry and numerical settings, a new model is developed employing adaptive mesh refining in the region of interest (i.e. close to the capillary and around the jet), as shown in Figure 11.4c. The situation dramatically changes in this case, showing a completely different behavior (Figure 11.4d): the turbulent region is now spread around the jet, forming a wake characterized by smoother changes and lower values of k (maximum value of 4.93 E+04 m^2/s^2).

This fact clearly demonstrate how the generated mesh can heavily influence the numerical results obtained from the model. Hence, it is very important to guarantee an adequate mesh density at least in the region of interest assuring solutions which are not mesh-dependent.

Anyway, increasing the mesh element number is not always straightforward since rising up the total amount of elements means dramatically increasing the computational time as well: as always, a compromise must be set between precision and computational effort.

A powerful mean to solve this problem is represented by the possibility of employing *adaptive mesh*.

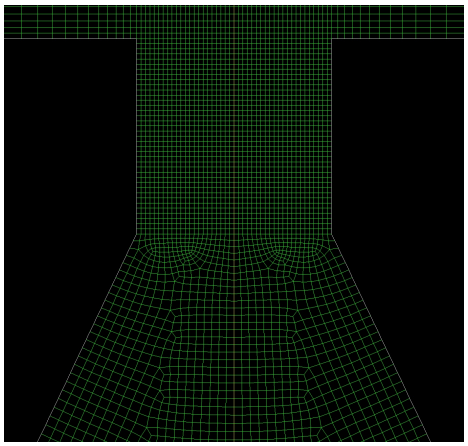

(a) *First model with coarse mesh.*

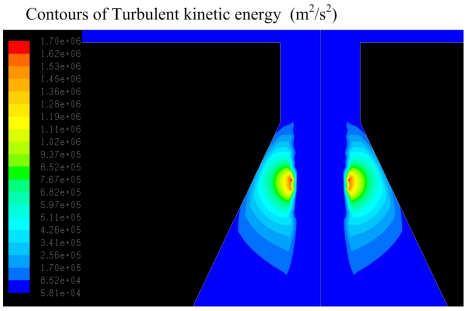

(b) *Contours of k (m^2/s^2) in the model with coarse mesh.*

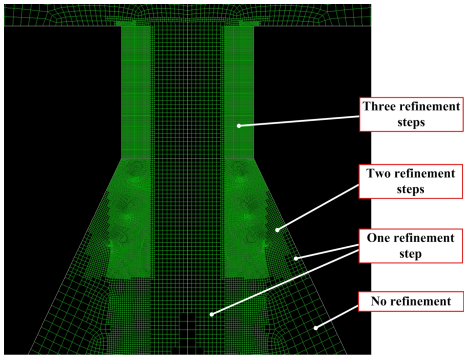

(c) *New model with refined mesh in the region close to the capillary and around the jet.*

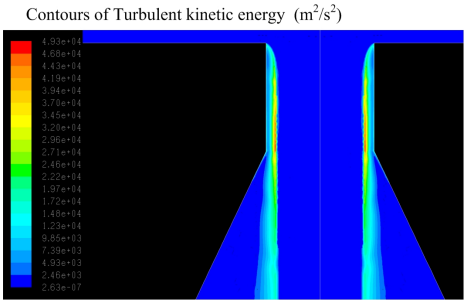

(d) *Contours of k (m^2/s^2) in the model with refined mesh.*

Figure 11.4: *Comparison between the results obtained from the same numerical model, respectively with coarse **(a, b)** and refined **(c, d)** mesh.*

11.4 Adaptive mesh

The solution-adaptive mesh refinement feature implemented in FLUENT®solver allows refining and/or coarsening of the grid, basing on geometric and numerical solution data: cells can be added just where they are needed in the mesh, thus enabling the features of the flow field to be better resolved. When adaption properly is used, the resulting mesh is optimal for the flow solution because the solution itself is used to determine where more cells need to be added. As a consequence, computational resources are not wasted by the inclusion of unnecessary cells.

Several different adaptive meshing methods are available, but they can be summarized into two main categories:

- **Static adaption process**: mesh adaption is performed just once.

- **Dynamic adaption process**: mesh adaption is periodically and automatically performed by the solver every fixed number of time steps.

Both this methods have been employed during the present work, therefore a brief introduction to each one of them is presented below.

11.4.1 Static adaption process

The static adaption process consists of two subsequently tasks:

1. The individual cells to be refined/coarsened are marked based on the adaption function, which is generated from geometric and/or solution data.

2. The cell is refined or considered for coarsening based on the previously performed adaption marks.

An "adaption function" is simply a list of user-defined parameters which the solver employs to mark cells for coarsening or refining; many adaption functions are available in the solver depending on the criteria adopted to mark the cells.

During the present work, the following adaption functions are used:

Region adaption function: this function marks or refines cells inside or outside a region user-defined by text (typing the coordinates of the region extents) or mouse input. Presently, a 2D mesh can be refined or marked inside or outside a quadrilateral or a circle. The region-based marking/adaption feature is particularly useful for refining regions that intuitively require good resolution: e.g., in the case of a PWJ, the capillary and the region surrounding the jet.

Iso-value adaption function: This function allows you to mark or refine cells inside or outside a specified range of a selected field variable function. The approach used in iso-value adaption function is to compute the specified user-defined variable of interest (such as x-velocity, k, ε, volume fraction,...) for each cell and then visit each cell, marking for refinement the cells that have values inside (or outside) the specified ranges.

Once the cells have been marked by the appropriate adaption function, the mesh is ready to be adapted (i.e. refined or coarsened) by means of *conformal* or *hanging node* adaption methods [21]. Since the model developed in the present work employs just quadrilateral mesh elements, the only available method in this case is the hanging node adaption, which is briefly presented below.

Hanging node adaption method

Adapted grids produced by the hanging node adaption procedure are characterized by nodes on edges and faces that are not vertexes of all the cells sharing those edges or faces, as shown in Figure 11.5a. Precisely, in case of 2D elements refinement, a triangle is split into 4 sub-triangles and a quadrilateral into 4 sub-quadrilateral, as shown in Figure 11.5b.

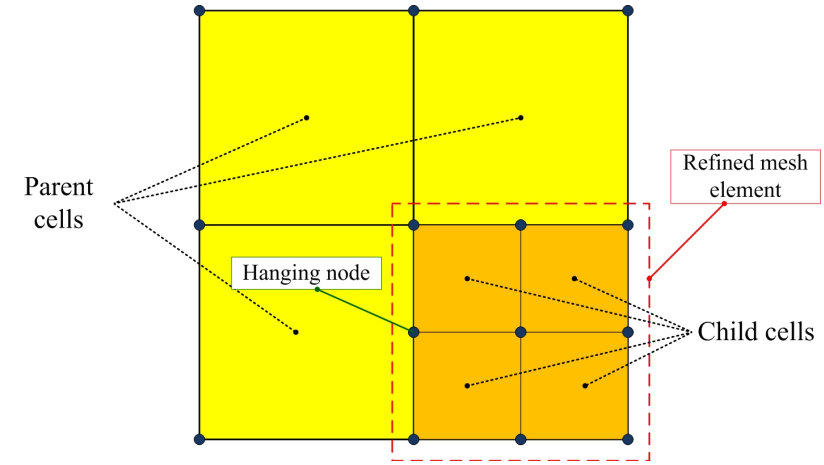

(a) *Example of a hanging node.*

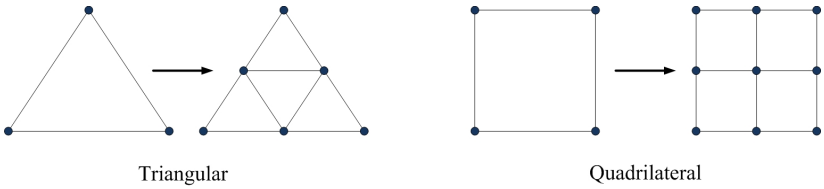

(b) *Hanging node adaption for 2D cell types.*

Figure 11.5: *Hanging node adaption procedure [21].*

In order to maintain accuracy, neighboring cells are not allowed to differ by more than one level of refinement: this prevents the adaption from producing excessive cell volume variations (reducing truncation error) and ensures that the positions of the parent (original) and child (refined) cell centroids are similar, reducing errors in the flux evaluations.

In case of coarsening, the mesh is coarsened by reintroducing inactive parent cells (uniting the child cells to reclaim the previously subdivided parent cell). An inactive parent cell is reactivated if all its children are marked for coarsening. It is eventually possible to get back the original grid with repeated application of the hanging node coarsening. As a consequence, using the hanging node adaption process, you cannot coarsen the grid further than the original grid.

11.4.2 Dynamic adaption process

Dynamic adaption process employs the same procedure of any static adaption process with the exception that it is not performed just once, but it is periodically repeated during calculations: in this way, the mesh can continuously adapt to the evolving flow field optimizing the mesh distribution. In the case of the present study, a dynamic adaption process based on a iso-value adaption function is performed.

Figure 11.6 shows the control panel for dynamic adaption with the setting used in the presented model. The settings are explained below:

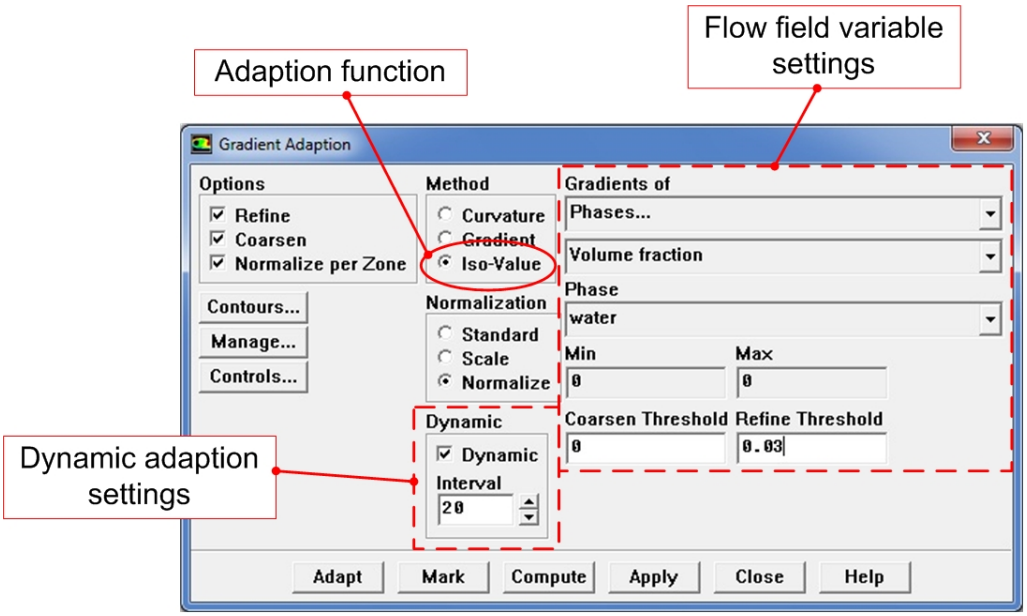

Figure 11.6: *Dynamic adaption control panel: settings used in the present work.*

Option "Refine" and "Coarsen" are both selected in order to allow the solver either to refine or coarse the mesh.

Dynamic adaption settings The option "Dynamic" is selected in order to activate the dynamic adaption and the number of time steps passing between two subsequent adaption is set in "Interval".

Adaption function The appropriate adaption function method is selected; as explained before, an iso-value adaption is performed in this case.

Flow field variable settings This parameters allow to select the flow field variable to be checked by the solver: in this case the chosen variable is the volume fraction of water. "Refine threshold" and "Coarsen threshold" values are the limits that the solver uses to discriminate whether to coarsen, refine, or do nothing.

Normalization No normalization is needed in this case, since the volume fraction already has values in the range [0-1].

Summarizing, with the presented settings, the solver performs mesh adaption every 20 time steps based on iso-value adaption function; for every adaption, the solver compares the value of the water volume fraction of each cell to the threshold values and, if the cell value is higher than the "Refine threshold" value, the cell is refined, while if cell value is lower than "Coarsen threshold" value, the cell is coarsen, otherwise it does nothing.

In the present study, adaptive mesh methods have been heavily employed, saving a lot of computational time without sacrificing too much precision, as it will be pointed out in Section 12.4.

Chapter 12

Numerical Settings

According to what presented in previous Sections 5 and 11, the present chapter lists and explains solution strategies for the numerical model developed in the present work and the main numerical settings employed in the FLUENT®solver.

12.1 Model geometry and boundary conditions

The geometry of the model is presented in Section 8 Figure 8.3, while Figure 12.1 shows the applied boundary conditions, which are also specified below:

PRESSURE INLET: the total pressure at the inlet is set to 160 MPa, which is exactly the working pressure; Figure 12.2a shows a snapshot of the related control panel in the solver with the employed settings.

Since a turbulent model is also added, setting input values for the definition of turbulence at the inlet are required by the solver; different methods are available in order to define turbulence at a boundary, the chosen one is "Intensity and Hydraulic Diameter" in this case.

Turbulent intensity I is defined as

$$I \equiv \frac{U'}{U} = \frac{\sqrt{1/3\,(u'^2 + v'^2 + w'^2)}}{\sqrt{u^2 + v^2 + w^2}} \tag{12.1}$$

where U' is the root mean square of the turbulent components of velocity vector and U the Reynolds averaged mean velocity.

To estimate accurately I, it is suggested to have some form of measurements or previous experience to base the estimation on, although experimental data are often hard to collect. Otherwise, there are some commonly used guidelines which can help the user to coherently guess incoming turbulence intensity:

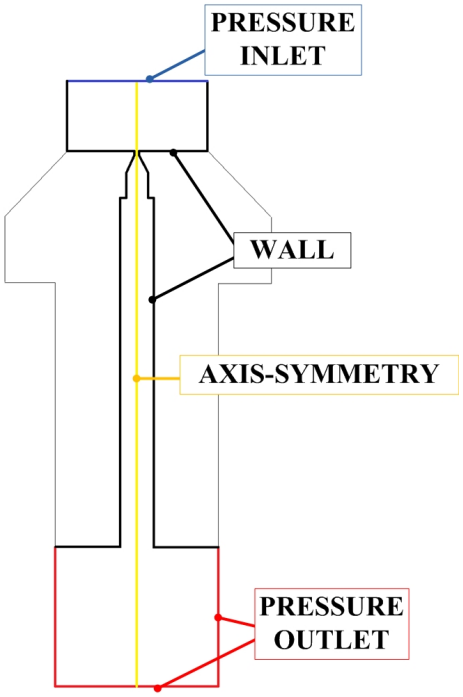

Figure 12.1: *Boundary conditions applied to the model.*

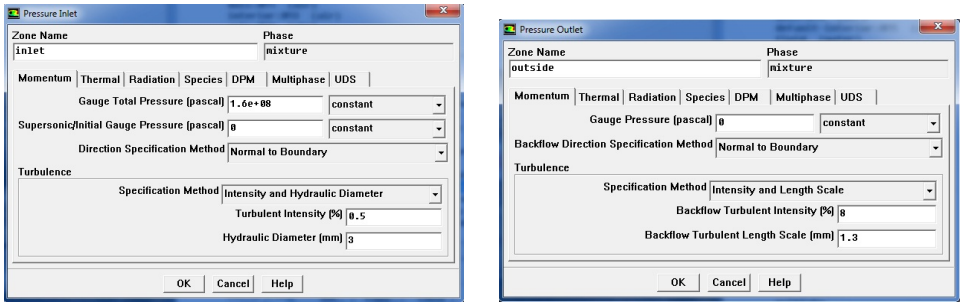

(a) *Pressure inlet control panel.* **(b)** *Pressure outlet control panel.*

Figure 12.2: *Pressure inlet **(a)** and pressure outlet **(b)** control panels showing the present employed settings.*

- common values are in the range of 5-20 % for high-turbulent flows.
- the range is between 1-5 % for medium-turbulent flows.
- the values are less than 1 % for low-turbulent or laminar flows.

Parameters set up for pressure inlet are summarized in Table 12.1.

PRESSURE OUTLET: the pressure along the "outside" boundary is set as atmospheric (i.e. 101325 Pa). Pressure measurements show that this value

PRESSURE INLET		
Gauge total pressure (Pa)	→	160 E+06
Turbulence specification method	→	Turbulent Intensity and Hydraulic Diameter
Turbulent Intensity I (%)	→	0.5
Hydraulic Diameter (mm)	→	3

Table 12.1: *Pressure inlet settings.*

is consistent with reality, as presented in Section 14.3. Note that the input in pressure outlet control panel (Figure 12.2b) is required in terms of "Gauge Pressure" which is the difference between the actual pressure on the boundary and the reference pressure (set as atmospheric in the present work): as a consequence, inserting a value of 0 means that this difference is null, and so the pressure is atmospheric at the boundary.

Similarly to what explained before for pressure inlet, a specification for turbulence for the possible backflow (flow possibly entering the domain through the boundary) is necessary as well; in this case, the chosen method is "Turbulent Intensity and Length Scale". Since the boundary is close to the orifice exit where the air flows at high velocities, the backflow is hypothesized as medium-turbulent and a value of 8% for I is guessed. The turbulent length scale l_{eddy} is the biggest possible size of the eddy which can be simulated, and it is usually considered as the 70 % of the smallest characteristic length of the domain [19]. Referring to Figure 12.3, the smallest characteristic length of the outside domain is L_c = 1.75 mm and so the length scale becomes l_{eddy} = 0.7 L_c ≅ 1.3 mm. Figure 12.2b and Table 12.2 summarize the employed settings for the pressure outlet boundary conditions.

PRESSURE OUTLET		
Gauge pressure (Pa)	→	0
Turbulence specification method	→	Turbulent Intensity and Length Scale
Turbulent Intensity I (%)	→	8
Length scale l_{eddy}(mm)	→	1.3

Table 12.2: *Pressure outlet settings.*

WALL: the walls are considered as stationary with "no slip" shear condition (i.e. zero velocity of the fluid in contact with the wall), while the rest of the settings are kept at default values. Moreover, it is added the "wall adhesion" model (see Section 7.4.2 for more details) in order to better simulate the

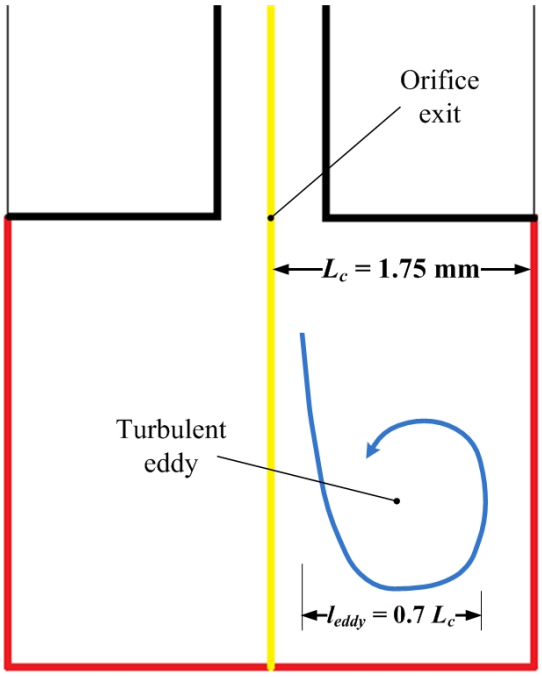

Figure 12.3: *Turbulent length scale l_{eddy} definition for pressure outlet backflow.*

shape of water droplets stuck on the walls. The contact angle is set to 76° [34], as previously precised (Section 7.4.2).

AXIS-SYMMETRY: the problem was considered axis-symmetric in order to solve just for one half of the 2D model and save computational time. Considering the problem as axis-symmetric is well-advised and it has been commonly done in almost all previous literature [7][11][8][10].

12.2 Added physical models

As precised in Section 11.1, physical models need to be added in order to properly simulate the PWJ process. Table 12.3 summarizes all the implemented models which are also described below:

TIME DEPENDENCE: the problem is considered unsteady. Time discretization is performed employing "variable time stepping" method, as already explained in details in Section 11.2. The employed settings are shown in Figure 12.4. The average time step is around 1 E-09 s and convergence at each time step is reached in about 20 iterations with no troubles, which although sligthly higher than the suggested value (Section 11.2) it guarantees good stability and relatively fast convergence without lowering too much the time step value.

MODEL PARAMETERS		
Time dependence	→	Unsteady
Viscous model	→	Turbulent
Turbulent model	→	$k-\varepsilon$ Realizable
Multiphase model	→	VOF
VOF scheme	→	Explicit
Body forces	→	Yes
Surface tension water-air	→	7.3E-02 N/m

Table 12.3: *Model parameters employed*

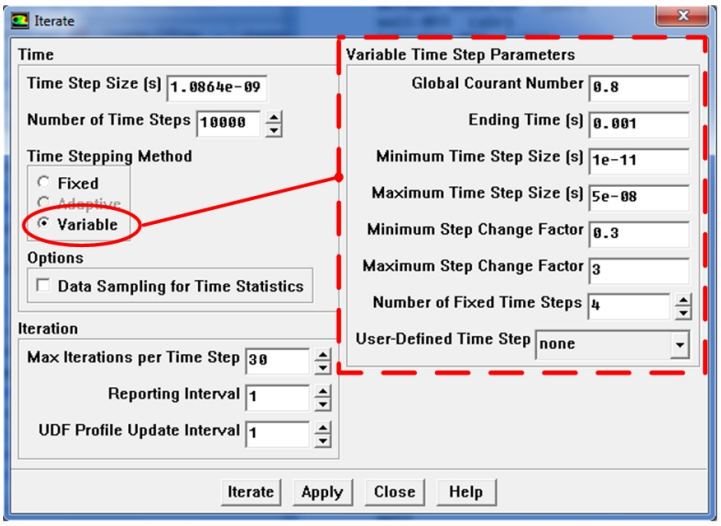

Figure 12.4: *Variable time stepping settings employed in the present model.*

VISCOUS MODEL: a model for turbulence is added to the model. More precisely, the selected model is "$k-\varepsilon$ model realizable" (see Section 4.4.4),since it is more precise than the standard $k-\varepsilon$ model and it does not require much more CPU time: it is therefore a good compromise between precision and required computational effort, see Section 4.4.2 for more details.

MULTIPHASE MODEL: since the problem involves water and air, a multiphase model is necessary.

Among all the multiphase models, VOF method is particularly suited for the purposes of the present work, since it provides a simple and economical way to track free surfaces (see Section 7 for more details). Both phases are considered incompressible and air is chosen as primary phase.

Moreover, the scheme employed to solve for volume fraction is the "Explicit

scheme" which, together with geometric reconstruct (see Section 12.3) is recommended to simulate jet breakup [21], as already noticed in Section 7.3.1.

BODY FORCES: these forces are basically the gravity force which is taken into account by adding a downward constant acceleration vector equal to g = 9.81 m/s^2.

SURFACE TENSION: as already mentioned, addition of surface tension is crucial to get precise results in surface tracking and breakup simulation. The employed value for water-air interaction is 7.30 E-02 N/m. See Section 7.4.1 for more details.

12.3 Solver settings

The present section collects all the settings related to the numerical methods employed by the solver. Table 12.4 summarizes the solver settings which are also listed below:

SOLVER SETTINGS		
Pressure-Velocity coupling	→	PISO
Neighbor correction	→	3
Skewness correction	→	0
Skewness-Neighbor coupling	→	No
Discretization schemes		
Pressure	→	PRESTO!
Momentum	→	2nd order
Volume Fraction	→	Geo reconstruct
Turbulent kinetic energy (k)	→	2nd order
Turbulent dissipation rate (ε)	→	2nd order

Table 12.4: *Employed solver settings.*

PRESSURE-VELOCITY COUPLING: the employed algorithm is PISO since it offers higher stability and speeds up convergence if compared to other algorithms such as SIMPLE. Model mesh is very low skewed and so it is not necessary to perform any "skewness correction" or "skewness-neighbor coupling", while 3 iterations are set up for "neighbor correction" in order to have a better convergence. PISO algorithm is presented more in detail in Section 5.2.1.

DISCRETIZATION SCHEMES: after the first time steps where "1st order upwind" is employed, all the schemes are later changed into "2nd order upwind" which guarantees much better results and reduces numerical diffusion, as mentioned in Section 5.1.3.

The "geometric reconstruct" scheme is selected for volume fraction since it allows to trace more precisely the water-air interface (see Section 7.3.5).

Pressure discretization scheme is set to "PRESTO!" since it is the one giving better results and higher rate of convergence.

UNDER-RELAXATION FACTORS: as suggested by FLUENT® user guide [21], when using PISO algorithm, the URFs can usually be raised up close to unit; anyway, URF for density, body forces and momentum are lowered to 0.5 since this gives much better stability and no problems in convergence at all. Table 12.5 collects all the URFs employed.

Variable	URF
Pressure	0.9
Density	0.5
Body force	0.5
Momentum	0.5
Turbulent kinetic energy k	0.9
Turbulent dissipation rate ε	0.9
Turbulent viscosity	0.9

Table 12.5: *Employed under-relaxation factors.*

12.4 Mesh generation

As underlined in Section 11.3 and 5.1.1, mesh generation is crucial to get a final precise solution. Several trial simulations have been carried out in order to optimize mesh distribution coherently to the more interesting regions in the flow field and finally setup a numerical model that does not require too much computational effort.

A clear example is presented in Figure 12.5. Figures 12.5a and 12.5b refer to a previous trial model where no mesh adaption is performed: here, higher mesh density is concentrated in the region close to the capillary (Figure 12.5a) and this inevitably results in stretched elements (very high aspect ratio) in the bottom part of the domain, close to the orifice exit, since the total number of elements must be limited to avoid exceeding a reasonable computational time.

On the other hand, the mesh is generated in a more uniform way and it is characterized by slightly coarser dimensions in the final model. Where needed,

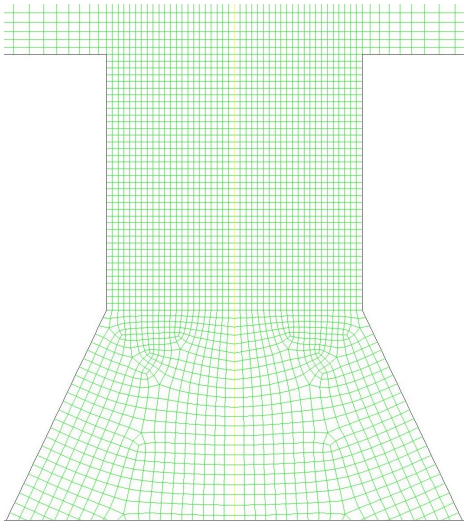

(a) *Trial model: capillary region.*

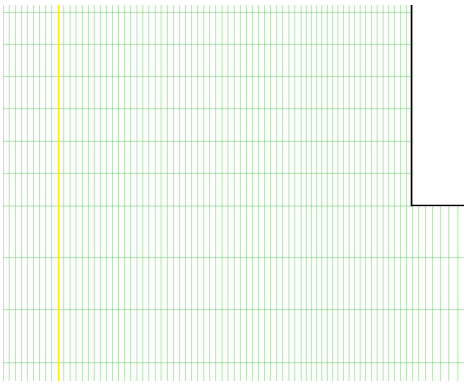

(b) *Trial model: orifice exit.*

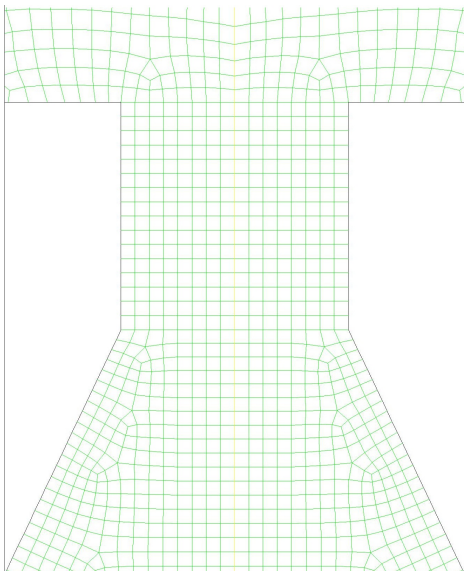

(c) *Final model: capillary region.*

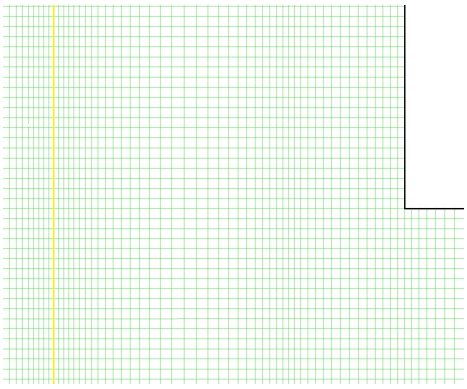

(d) *Final model: orifice exit.*

Figure 12.5: *Comparison of mesh distribution between a previous trial model **(a, b)** and the final model **(c, d)**.*

more precision is eventually achieved by later refining mesh with mesh adaption methods. This results in a higher quality mesh, characterized by low aspect ratio as well. Note that since adaptive mesh methods refine each element just by splitting it into four equal sub-elements (see Section 11.4), the aspect ratio is kept constant and so refining does not significantly affect mesh quality; the only drawback is the sudden change in elements dimensions which sometimes can determine erroneous results due to local higher truncation error. See Section 11.3 for advices and considerations on mesh generation.

The final mesh setup for the present numerical model is summarized in the following sections.

12.4.1 Basic mesh

As previously mentioned, the strategy adopted to generate mesh for the final numerical model consists in employing slightly coarse but more uniform elements throughout the whole domain, and later refining the more significant regions by means of adaptive mesh methods. Snapshots of the basic mesh are shown in Figure 12.6.

It is possible to notice that the elements are almost all rectangular quadrilateral (producing very low value of skewness) with very low aspect ratio (AR) as well. AR values are always below 2.3 in the capillary region, the whole exit tube and the region close to the symmetry axis in the outside domain, which are indeed the most important regions where higher precision is needed. Figure 12.7 shows how aspect ratio varies going from the axis toward the lateral outside boundary: elements closer to the axis have very low values of AR which progressively increases moving toward the boundary where AR reaches the maximum value of 10. Anyway, this is acceptable since a loss of mesh quality in that region is not affecting the main interesting results. More details on mesh quality evaluation are in Section 5.1.1.

The resulting mesh has therefore a good quality, but it is still not fine enough to adequately track the interface shape: mesh coincides to the spatial discretization which is the resolution of the flow features which can be resolved: it is therefore necessary to increase mesh density (ans so spatial resolution) in the regions where the jet flows in order to capture with high precision the shape assumed by the interface and the possible small droplets detaching from it.

To achieve this, adaptive mesh is employed.

12.4.2 Mesh adaption steps

The purpose of mesh adaption is refining the mesh in the regions of the domain where important flow features take place (see Section Chapter:Cons:Section:AdaptMesh). In this case, the most interesting regions to be adapted are the capillary region

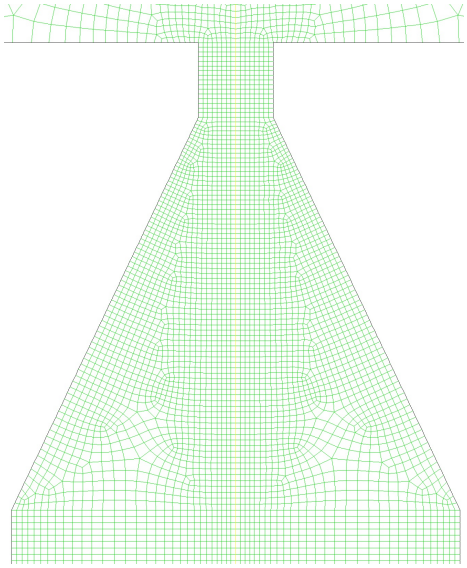

(a) *Model mesh close to the orifice capillary.*

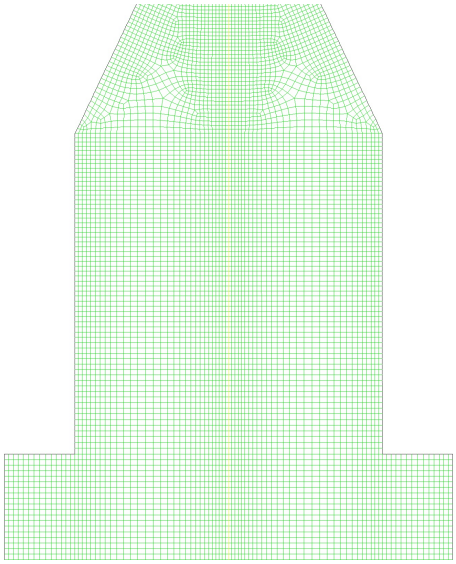

(b) *Model mesh at the beginning of the orifice exit tube.*

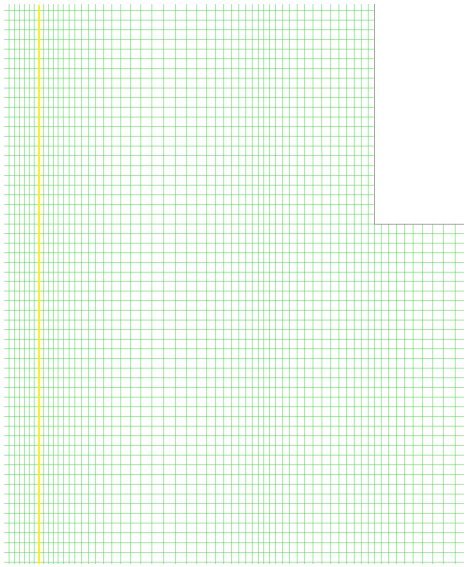

(c) *Model mesh at the exit of the orifice exit tube.*

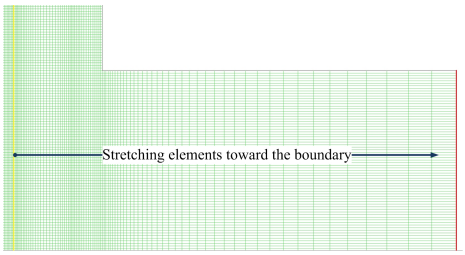

(d) *Model mesh close to the outside boundary.*

Figure 12.6: *Zoomed views of model mesh.*

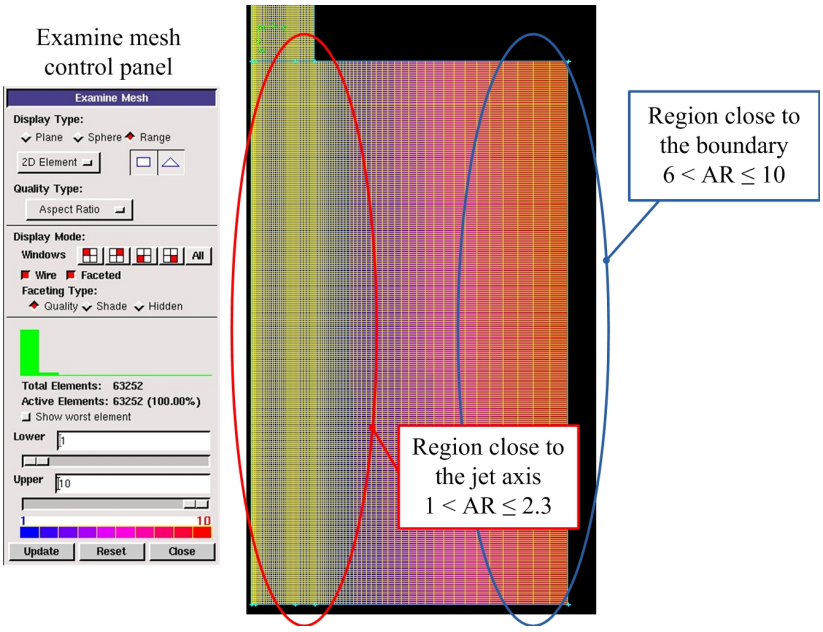

Figure 12.7: *Aspect ratio check in Gambit®.*

MESH SUMMARY		
Number of total elements	→	63252
Minimum cell volume (m^3)	→	3.72 E-16
Maximum cell volume (m^3)	→	2.02 E-10
Number of total elements	→	63252
Max aspect ratio value close to outside boundary	→	10
Max aspect ratio value close to jet axis	→	2.3

Table 12.6: *Basic mesh quality summary.*

and the regions surrounding the jet.

Mesh adaption has been made in three different phases, as reported below:

Phase 1 Before starting calculations, the region close to the orifice is manually refined by means of a "static adaption" based on "region adaption function" (see Section 11.4.1 for details). Important phenomena take place close to the capillary and it is therefore crucial to adequately refine this area.

Results are summarized in Table 12.7 and Shown in Figure 12.8.

The minimum cell volume has decreased of two order of magnitude (compare it to Table 12.6) resulting in a much higher spatial resolution. Besides,

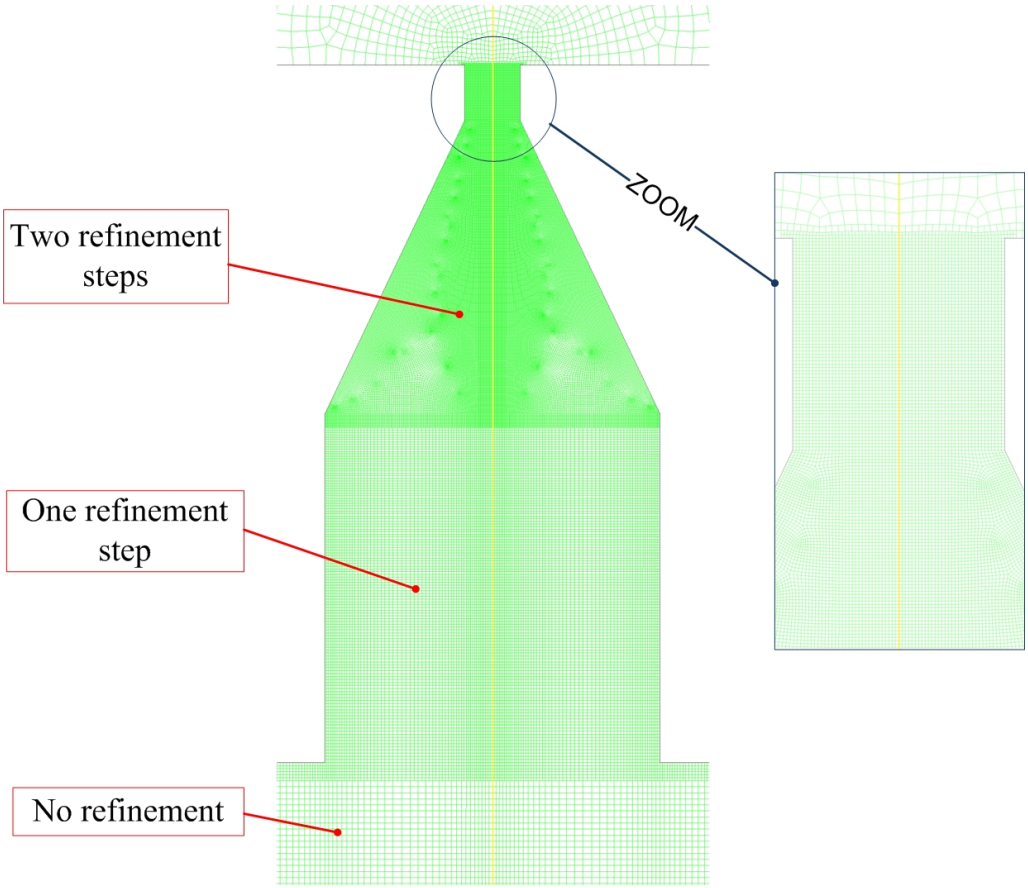

Figure 12.8: *Mesh adaption-Phase1: refining close to the capillary.*

MESH SUMMARY AFTER THE FIRST REFINING STEP		
Number of total elements	→	95802
Minimum cell volume (m^3)	→	5.68 E-18
Maximum cell volume (m^3)	→	2.02 E-10

Table 12.7: *Mesh adaption-Phase 1: mesh summary.*

total cell number has also greatly increased causing a much higher computational effort and a slowdown of calculations.

Phase 2 Before the jet exits the refined region presented before, a dynamic adaption process is enabled. The aim is to automatically refine the region surrounding the jet as the created jet itself advances through the domain. The employed settings are shown in Figure 12.9.

With the presented settings, the solver performs mesh adaption every 2 time steps basing on the iso-value adaption function (see Section 11.4.1); for

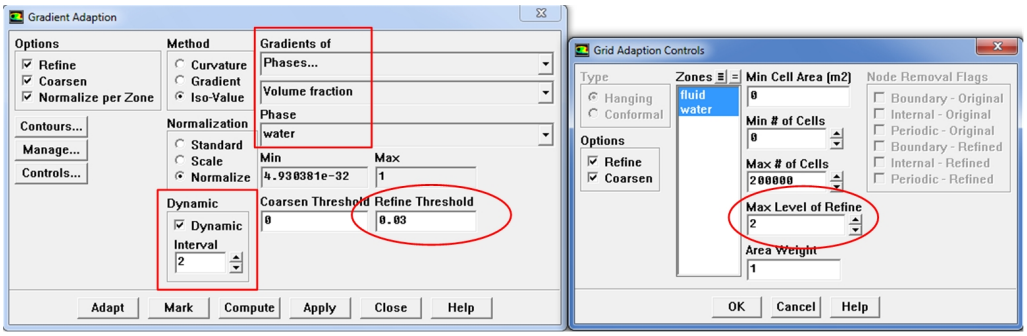

Figure 12.9: *Mesh adaption-Phase 2: control panel.*

every adaption, the solver compares the value of the water volume fraction of each cell to the threshold values and, if the cell value is higher than the "Refine threshold" (i.e. 3%), the cell is refined, while if cell value is lower than "Coarsen threshold", the cell is coarsen, otherwise it does nothing. See Section 11.4.2 for further explanation of the settings parameters.

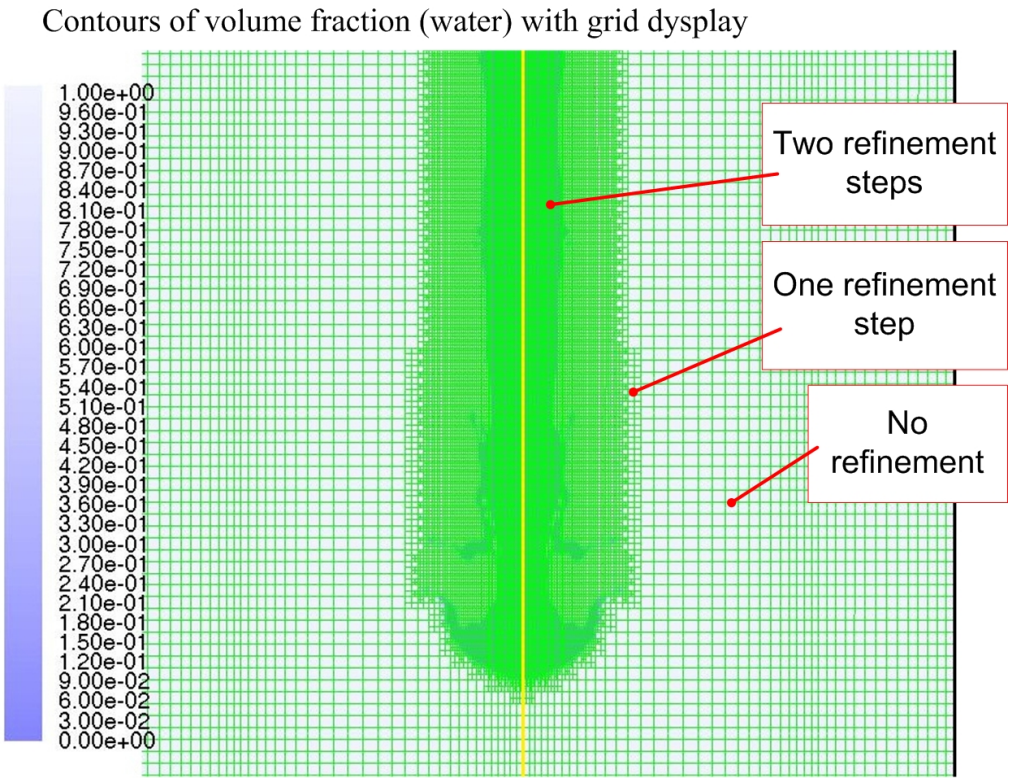

Figure 12.10: *Mesh adaption-phase 2: dynamic mesh adaption.*

Figure 12.10 shows the result of the automatic adaption where it is possible to notice how effectively the region is well refined where the jet flows.

Phase 3 Available computational resources to run the present simulations are pretty limited and it is therefore necessary to limit the number of total mesh elements in order to complete calculations in a reasonable time. As a consequence, once the jet has reached half of the exit tube, the dynamic mesh refinement is disabled and since then on, the mesh adaption is manually performed again. The same procedure of phase 1 is performed (i.e. manual "static adaption" based on "region adaption function") according to the following criteria:

- mesh elements are added in front of the flowing jet head so that it always encounters refined regions and its surface is properly tracked, as shown in figure 12.11a.
- mesh elements are manually removed from the region where they are no more necessary, especially in the core of the jet, since the important area is the one close to the surface of it, as shown in Figure 12.11b.

Acting this way, it is possible to limit the total number of elements and guarantee at the same time enough precision in the regions where this is needed.

The total amount of mesh elements at the end of the simulation is around 18000, which is almost the triple than the elements of the first original mesh. This obviously results in a long CPU time which is however unavoidable in order to obtain precise enough solutions.

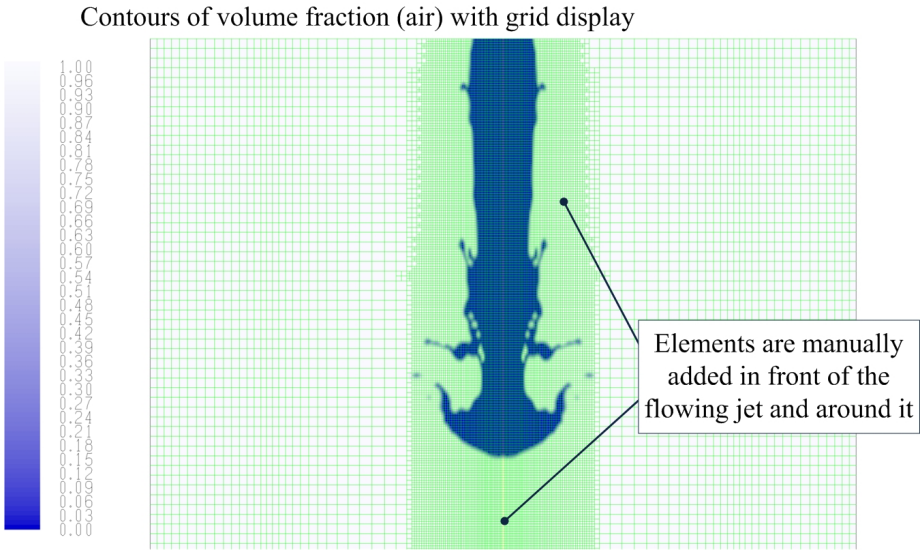

(a) *Addition of mesh elements in front of the flowing jet head.*

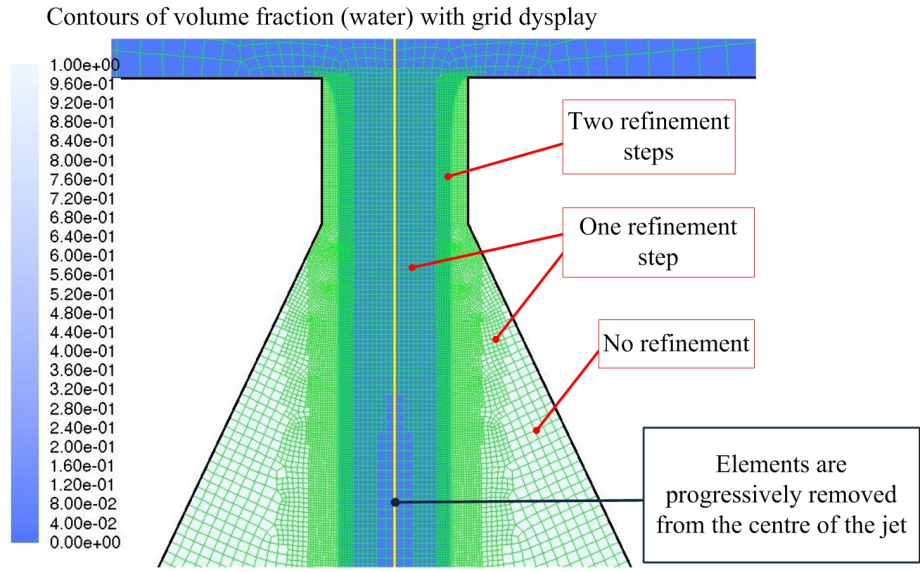

(b) *Removing elements from the already-formed jet core.*

Figure 12.11: *Mesh adaption-Phase 3: manual addition and removal of mesh elements.*

Chapter 13

Numerical results

The present chapter collects the most significant results from the developed numerical model. The efforts have been concentrated in understanding the main causes of the disturbances affecting jet stability and the effects that the presence of water inside the tube can produce.

13.1 Jet creation

The first instants of jet creation are important because, depending on the geometry of the orifice and the working conditions, reattachment of the fluid to the walls and cavitation could occur. As previously mentioned, this is just a temporary condition since a pure water jet in steady conditions reaches a stable flipped regime in any case, but these phenomena could damage the integrity of the jet and its quality [11].

A numerical simulation is carried out in order to investigate the mechanisms of jet creation and their dependence on the orifice inner geometry; the results are reported in Figure 13.1: it is possible to notice that the jet hardly reattaches to the bottom corner of the capillary ((A) and (B)) and this fact produces a small perturbation of the jet (C) which later breaks into several droplets (D). These results are in accordance to what found in literature.

To highlight the importance of orifice geometry on jet creation, the same numerical analysis is performed for an orifice equal to the previous one excepting for the bottom edge of the capillary which is rounded instead of sharp. It is evident, as shown in Figure 13.2, that no reattachment occurs in this case and the jet front stays more compact and coherent than before without creating any droplets.

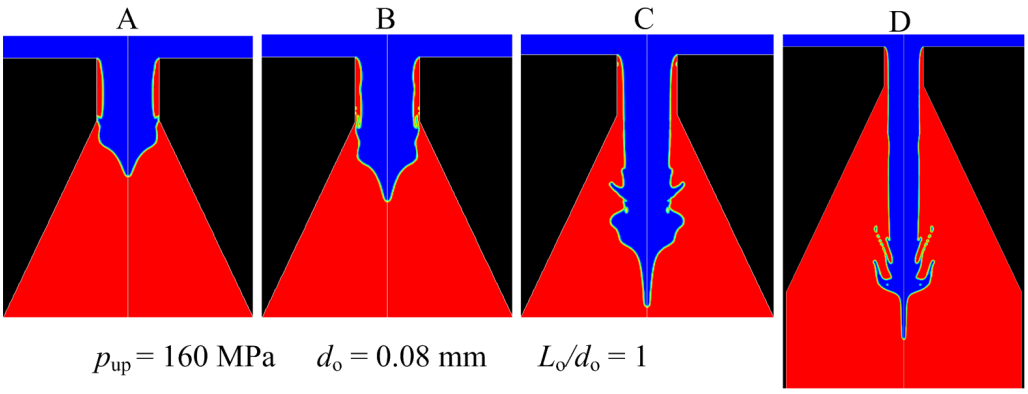

Figure 13.1: *Numerical simulation of the first instants of jet creation.*

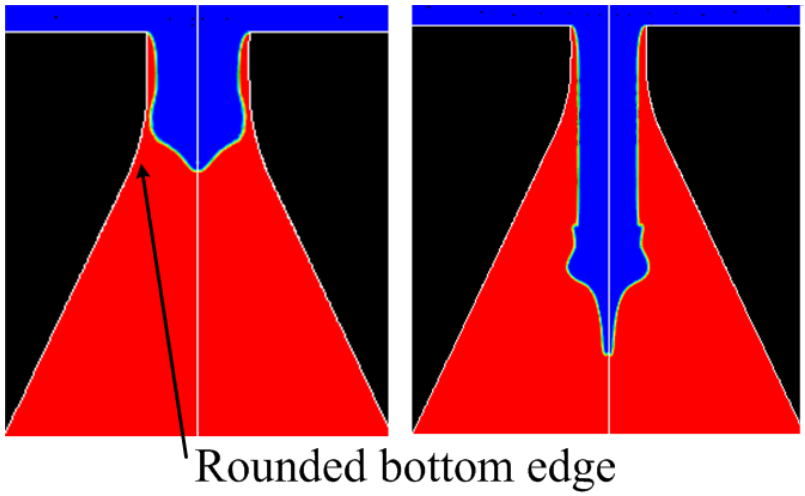

Figure 13.2: *Jet creation in an orifice with rounded bottom edge.*

13.2 Recirculation inside the orifice and droplets dragging

The main water jet flows inside the orifice tube at high velocity and carries away the air close to its interface due to "no slip" condition. As there is a flux of air surrounding the jet exiting the orifice there is some fresh air entering from the bottom opening of the tube in order to guarantee the mass balance: recirculation takes place inside the orifice tube with air moving upward close to the external orifice walls, and air dragged downward close to the main jet: Figure 13.3 clearly shows this behavior representing the pathlines colored by the velocity magnitude in the upper region of the orifice and at the very exit of the orifice tube.

This air velocity field affects the behavior and the motion of the droplets which are not completely pushed outside the tube: the interaction among droplets and moving air is strong as the air moves upward at high speeds (up to

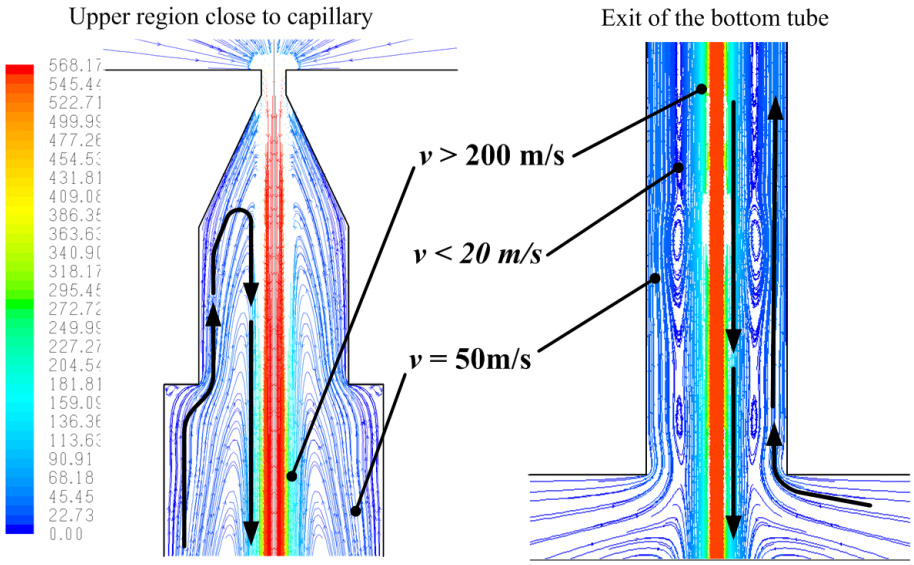

Figure 13.3: *Pathlines colored by velocity magnitude (m/s) inside the orifice tube.*

50 m/s) inside the tube causing high drag forces lifting the drops up.

It is therefore possible to evaluate the balance of the forces acting on a droplet, as shown in Figure 13.4. Assuming the droplet to be a perfect smooth sphere the

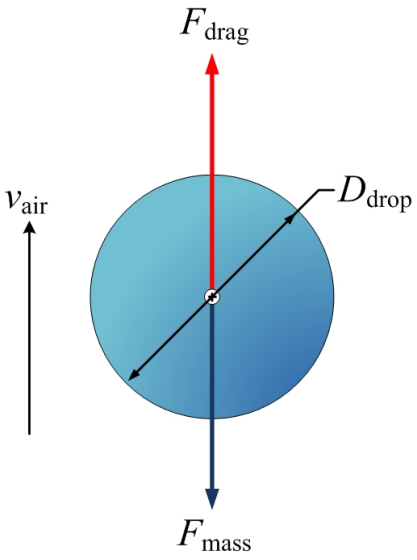

Figure 13.4: *Force acting on a spherical droplet immersed in an air flow.*

drag force can be determined with the following expression:

$$F_{drag} = C_D \, \rho_{air} \, v_{air}^2 \, \frac{\pi}{4} \, D_{drop}^2$$

where C_D is the *coefficient of drag*, which is basically dependent on *Re* and it is experimentally determined as reported in Figure 13.5.

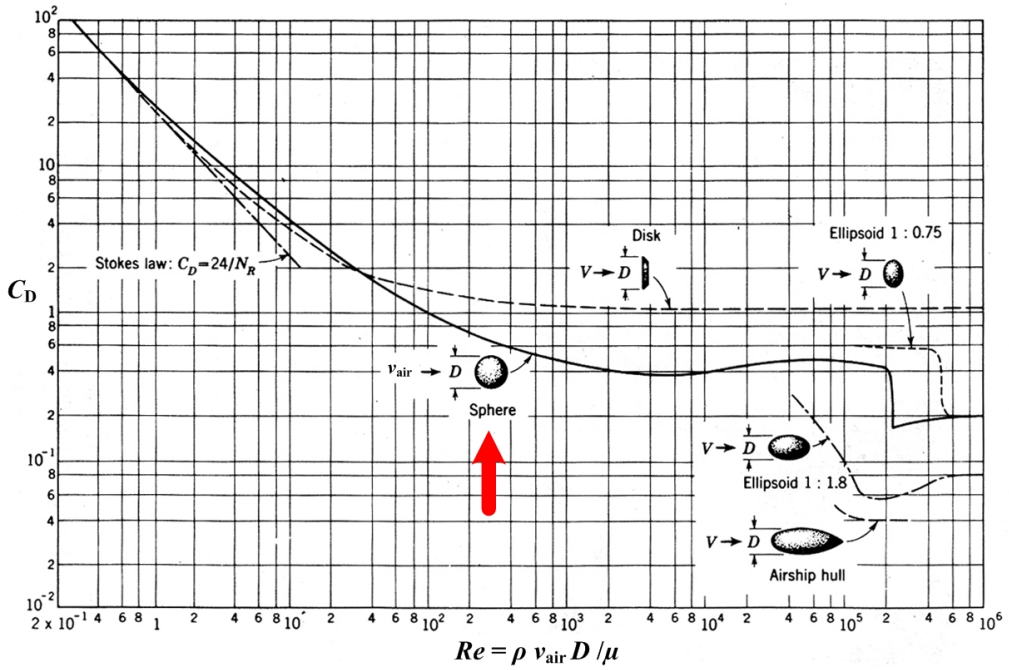

Figure 13.5: *Coefficient of drag as a function of Reynolds number (www.me.utexas.edu).*

While the mass force acting downward is

$$F_{\text{mass}} = \rho_w \frac{4}{3}\pi \frac{D_{\text{drop}}^3}{8} \tag{13.1}$$

Constants employed are collected in Table 13.1. Varying the velocity of the

D_{drop} (μm)	ρ_{air} (kg/m^3)	μ_{air} (kg/m $\cdot$ s)	ρ_w (kg/m^3)
5	1.23	1.79 E-05	998.20

Table 13.1: *Employed constants in force balance.*

air flow around the water droplet, *Re* and so C_d vary as well (Figure 13.5), and consequently also the resulting drag force.

Results are summarized in Table 13.2: it is evident how even for low values of v_{air} the drag force is constantly higher than the mass force, and this results obviously in a net force acting upward and lifting the drop up.

As depicted in Figure 13.6, both droplets marked with number **1** and **2** are accelerated upward by aerodynamic drag forces, even if droplet **1** is faster as it is

v_{air} (m/s)	Re (-)	C_d (-)	F_{drag} (N)	F_{mass} (N)
2	0.68	35	1.68 E-09	6.41 E-13
10	3.42	10	1.20 E-08	6.41 E-13
20	6.85	7	3.37 E-08	6.41 E-13
50	17.11	3	9.02 E-08	6.41 E-13

Table 13.2: *Force balance on a spherical droplet immersed in air at different velocities.*

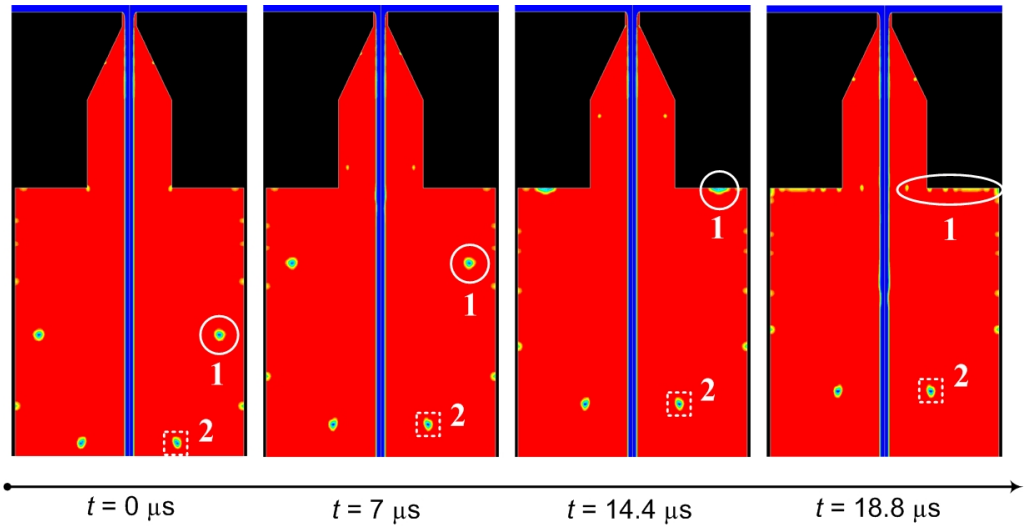

Figure 13.6: *Drop motion due to aerodynamic drag inside the orifice tube.*

closer to the external wall where the air moves at higher velocities. Moreover, it is noticeable how droplet **1** hits the upper wall of the tube breaking up into several smaller droplets: such mechanisms are further sources of droplet production.

13.3 Effects of droplets collisions

As previously hypothesized, the presence of water droplets can be a source of disturbances because they move inside the orifice tube and can eventually collide with the main water jet. There are two different mechanisms of interaction between a droplet and the main jet: one regarding the downstream region along the exit tube while a second one regarding the upper region close to the orifice capillary.

13.3.1 Interaction along the exit tube

As reported in Figure 13.3, the main water jet drags air forming a high-velocity air stream all around it: this layer acts like a protection for the jet. Figure 13.7

clarifies this phenomenon: as a droplet approaches the water, the rapid flux of air generally deflects the trajectory of the droplet pushing it away.

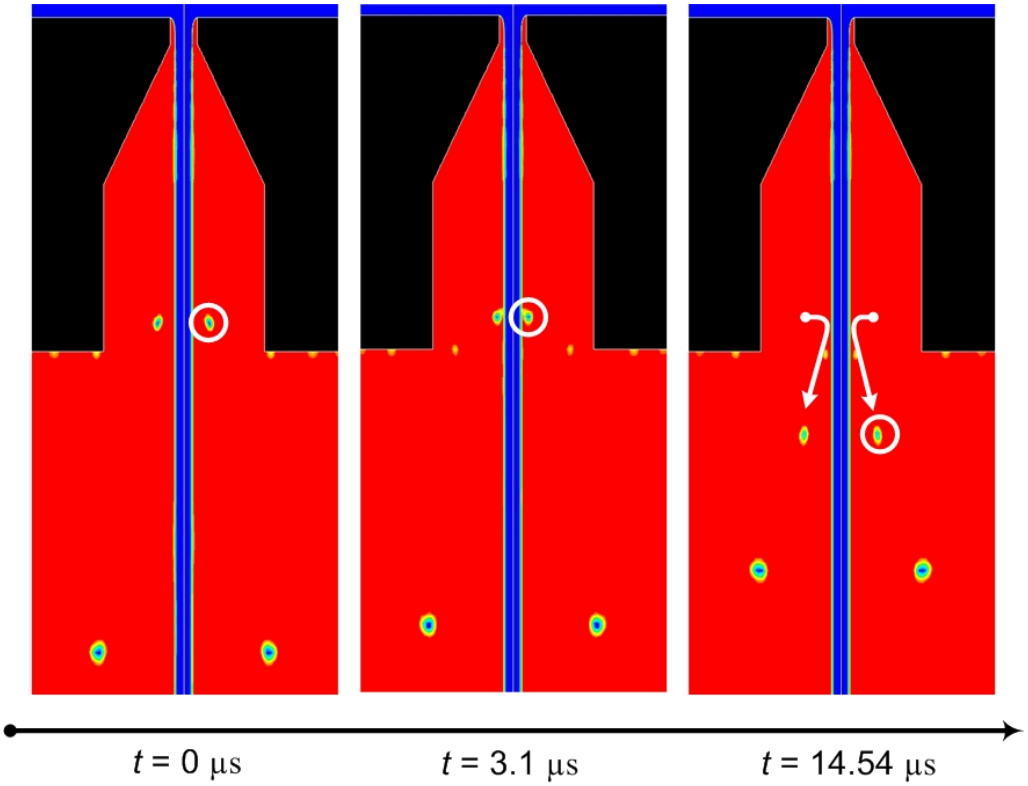

Figure 13.7: *Interaction between droplets and main water jet along the orifice tube.*

Only droplets with high inertia can collide effectively with the water jet causing a local perturbation in form of a bulk which is transported downstream by the main flow.

13.3.2 Interaction close to the capillary

Droplets can be sometimes lifted up and reach the capillary: this is the worst situation which can cause a stronger loss of coherence like the one reported in Figure 10.3-D.

As shown in Figure 13.8, when a droplet reaches the capillary (A-B), it can overfill the section by adhesion creating a bridge between the jet and the wall and consequently an air bag inside the capillary (C-D): this condition can later switch the orifice flow regime from flipped into cavitating, which produces a poor jet in terms of coherence as previously explained (Section 9).

Furthermore, if the droplet is big enough or the disturbance caused by previous droplets is consistent (E-F), the whole capillary can be completely filled

producing a situation similar to a single-phase jet (G); this regime as well is characterized by bad coherence compared to the flipped regime.

Weather the droplet switches the regime into cavitating or single-phase, the result is a loss of quality of the jet which temporary loses the constricted configuration.

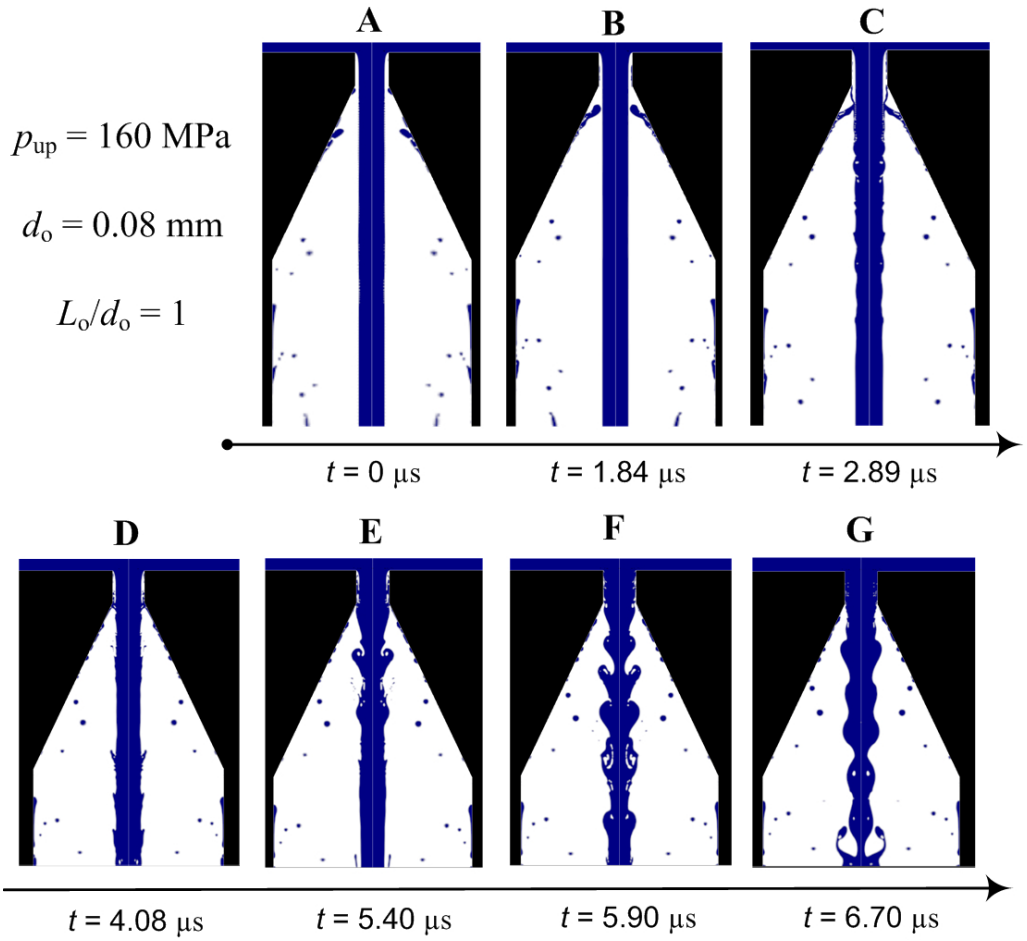

Figure 13.8: *Disturbances caused by droplets reaching the orifice capillary.*

Anyway, as mentioned in Section 9.2, this perturbation is lost and the constricted jet condition is soon recovered as the steady-state jet can count on a stable flipped regime and the cavitating or single phase flow regime cannot be maintained for long time.

As a conclusion of the present analysis, it is possible to infer that the mechanisms causing a more evident loss of coherence of the jet are localized in the region close to the capillary, while along the exit tube the jet seems "protected" by the dragged high-velocity layer of air surrounding it, with the only exception of some occasional bulks formed by high-inertia impacting droplets which, anyway, do not cause an actual breakup of the jet.

13.4 Turbulence analysis

Due to the high-velocity flow regimes developing inside the orifice, turbulence is expected to have great importance.

Turbulent kinetic energy k can be considered as a characteristic parameter of the turbulent energy of the flow, since it is expressed as $\frac{m^2}{s^2} = \frac{J}{kg}$.

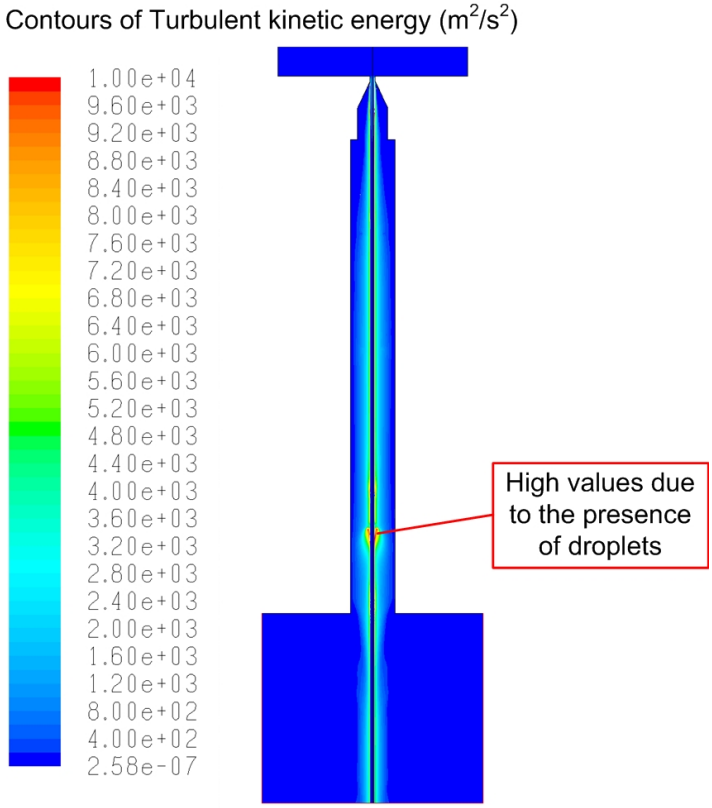

Figure 13.9: *Contours of turbulent kinetic energy k throughout the domain.*

Figure 13.9 shows the contours of k throughout the domain: with the exception of the two marked spots caused by the presence of droplets which induce localized turbulence, the values of k around the jet keep constant from the capillary to the exit. The turbulent area inside the orifice exit tube is slightly wider than the one outside the orifice, where turbulence dissolves more rapidly moving away the jet: this is reasonable since the flow inside the orifice is constricted between the walls with high velocities.

Anyway, the higher values of k are reached inside the capillary, as pointed out in Figure 13.10: due to the very narrow space, the air flowing between the jet and the capillary wall reaches higher velocities with consequently produce higher turbulence values.

Although there is no certain correspondence between high values of turbulent

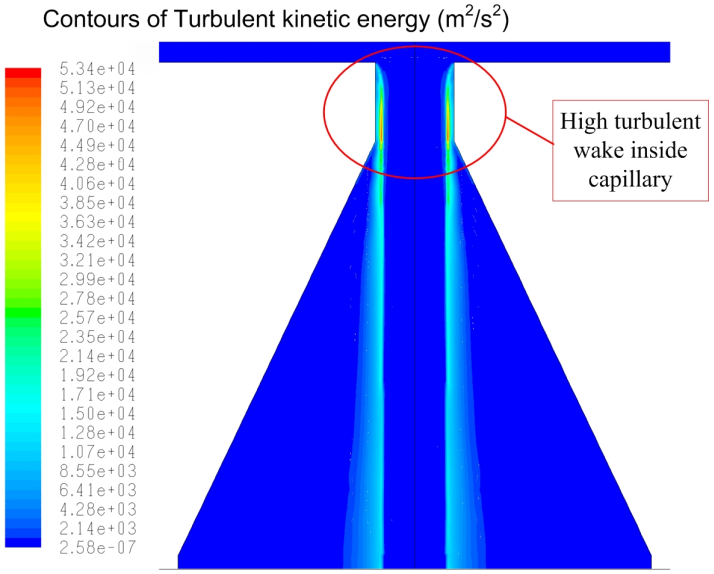

Figure 13.10: *Contours of turbulent kinetic energy k inside the capillary.*

kinetic energy and jet disturbance, the relation seems reasonable. Turbulent phenomena are characterized by local random variations in velocity magnitude and direction: the presence of a concentrated turbulent area in the surrounding air close to the jet (Figure 13.10) could imply also the presence of some random velocity components incident on the jet and causing local disturbances, droplets creation or vaporization of the jet external skin due to the high involved energies.

Moreover, the presence of a high turbulent wake inside the capillary could further enhance breakup, spreading of droplets and jet vaporization when disturbing phenomena like the one previously presented (Section 13.3.2) occur.

13.4.1 Influence of capillary geometry on turbulence

To determine whether the capillary geometry can affect the high-turbulent wake inside it, two more numerical simulations (with identical numerical settings and mesh comparing to the previous one) are carried out on models with different capillary geometries. Referring to Figure 13.11 where the behavior of the three capillaries are compared, the three different geometries are called respectively:

- **Normal**: the same as the previously presented model;
- **Rounded**: the bottom edge of the capillary is rounded;
- **Conical**: the capillary walls are not vertical but slightly inclined (so that the capillary has a conical shape) and the bottom edge is still rounded.

The comparison between the behavior of the three capillaries is presented in Figure 13.11 and Table 13.3: compared to the **normal** geometry, the **rounded** and

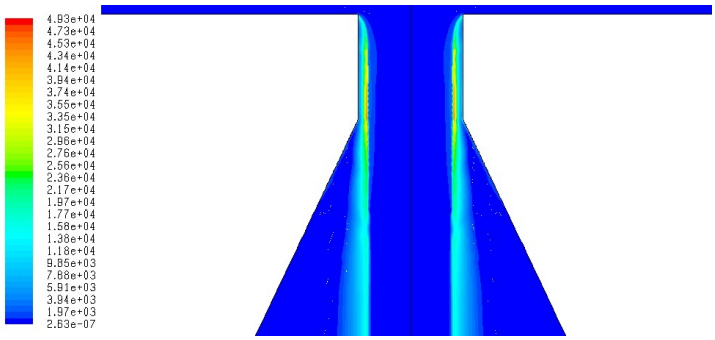

(a) *Capillary with normal geometry.*

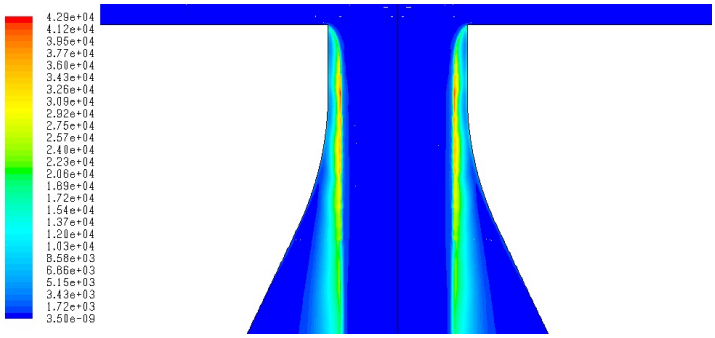

(b) *Capillary with rounded bottom edge.*

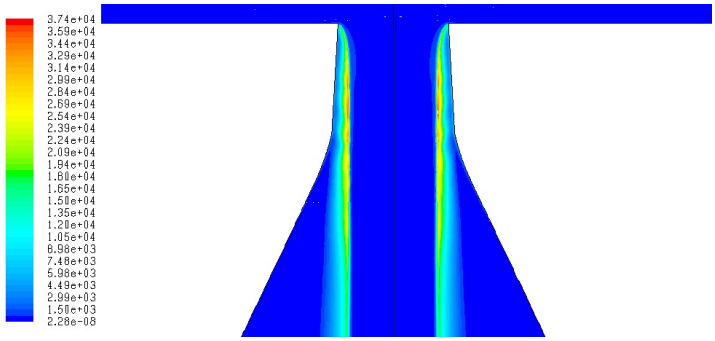

(c) *Conical capillary walls with rounded bottom edge.*

Figure 13.11: *Influence of different capillary geometries on k* (m^2/s^2).

the **conical** capillary produce effectively lower values of turbulent kinetic energy k, with a percentage reduction which is respectively around 13% and 24%.

Capillary geometry	Maximum value of k (m^2/s^2)	Percentage variation (%)
Normal	4.93 E+04	-
Rounded	4.29 E+04	-13.06
Conical	3.79 E+04	-24.26

Table 13.3: *Influence of capillary geometry on the maximum value of k.*

As previously mentioned, this fact does not directly implies that **rounded** and **conical** geometry produces a higher quality jet, but at least further investigations on this point are recommended since could lead to interesting results. The best way to prove it would be producing orifices with capillaries of the previously specified geometries and test them in working conditions: the modified geometries have been chosen on purpose, so that they could possibly be machined. Although manufacturing sapphires with such a geometries is not that straightforward for sure, a concrete possibility could be machine orifice inserts medo of poly-crystalline diamonds by means of EDM.

Chapter 14

Validation

Validation of numerical models is always challenging when dealing with WJ applications: experiments on this subjects are very rare and, if existing, very limited concerning detailed quantitative data. Quantitatively correct experiments are almost impossible since the physics and the dynamics inside a WJ orifice involve phenomena characterized by small length scales (in the order of few millimeters or less) together with very high velocity scales (from 500 up to 900 m/s) and rapid time scales (in the order of milliseconds). As a consequence, quite often numerical data are not directly compared to their physical quantities, but rather to macroscopic effects; as instance, the occurrence of cavitation is not validated with the direct measure of pressure inside the nozzle, but rather with the production of a non-coherent jet.

Anyway, the more validations are made, the more reliable the model is. The following sections will present some "alternative" validation which have been carried out in the present study.

14.1 Theoretical vs simulated velocity

Since water is considered incompressible in the numerical model developed, the theoretical velocity of the formed water jet can be calculated from Bernoulli's equation [39]:

$$v_{\text{th}} = \sqrt{\frac{2\,p_{\text{up}}}{\rho}} = \sqrt{\frac{2 \cdot 160\text{E+}06}{998.20}\frac{\text{Pa}}{\text{kg/m}^3}} = 566.20 \text{ m/s} \tag{14.1}$$

Referring to Figure 14.1, the numerical model gives a simulated velocity v_{sim} of 567 m/s . The percentage error is around 0.14% which means that the two data seem to be in perfect accordance.

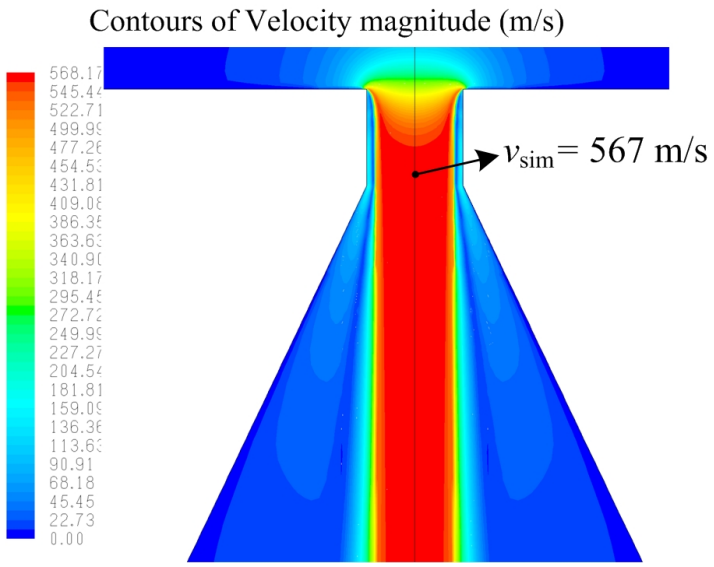

Figure 14.1: *Contours of velocity magnitude extrapolated from the numerical model*

14.2 Coefficient of contraction

Analyzing the contours plot of volume fraction of the different phases, it is possible to get the actual section of the formed water jet and so derive the coefficient of contraction C_c .

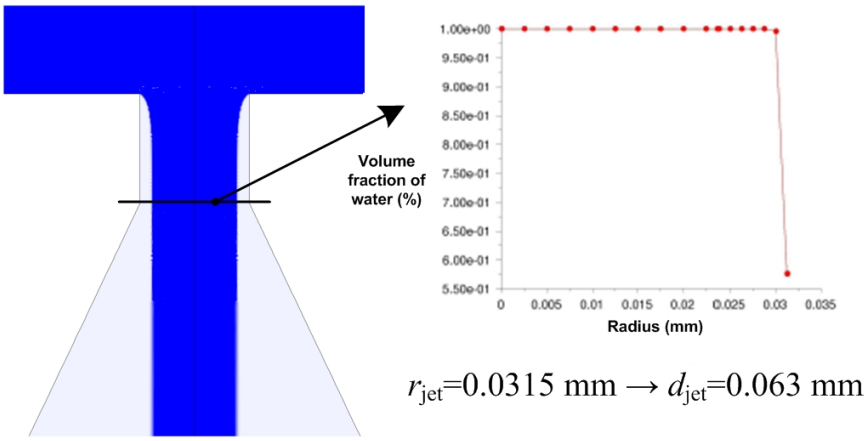

Figure 14.2: *Plot of volume fraction of water extrapolated from the numerical model*

Figure 14.2 report the plot of volume fraction (VF) of water along the radial coordinate at the exit of the capillary: water VF drops at around 0.315 mm which can then be considered as the radius of the formed jet; naming A_o the nominal section area of the capillary and A_{jet} the actual area of the jet, C_c is easily

determined:

$$C_c = \frac{A_{jet}}{A_o} = \frac{\frac{\pi\, d_{jet}^2}{4}}{\frac{\pi\, d_o^2}{4}} = \frac{0.063\ \text{mm}^2}{0.080\ \text{mm}^2} = 0.62$$

This value is in perfect accordance with the values found in literature [21].

Actually, remaining within the field of sharp-edge orifices, the value of C_c is strongly dependent on the radius of curvature of the capillary edge r_{ed}: the higher r_{ed}, the higher the coefficient of contraction C_c. It is therefore not unusual to find in literature C_c for sharp-edge plain WJ orifices in the range of $0.62 \rightarrow 0.67$ depending on this parameter. The capillary edge in the numerical model proposed is completely sharp (90° angle) and the value of 0.62 is consistent with this case.

14.3 Pressure measurements at the tube exit

Comparing direct measurements of a physical parameters to the relative simulated parameter is surely the best way of validating a model. The easiest feasible way to do so in our case is measuring air pressure at the very exit of the orifice exit tube, a region which has been taken into account in our numerical model domain.

The employed pressure sensor the model 24PCB-A1D by Honeywell (provided by RS) which belongs to the *differential uncompensated pressure transducer* family (Figure 14.3): this kind of sensors give as output a voltage (in mV) proportional to the difference between a reference pressure p_{ref} (equal to atmospheric pressure p_{atm} in this case) and a measured pressure p_{meas}.

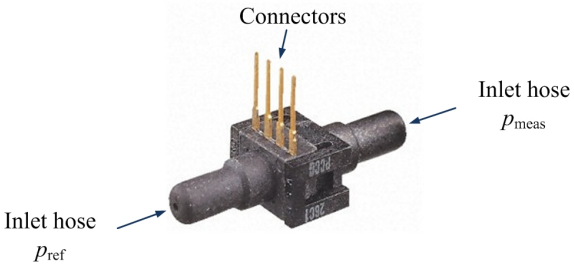

Figure 14.3: *Differential uncompensated pressure transducer*

$$\Delta V_{meas} \propto \Delta p = p_{meas} - p_{ref}$$

Appendix A reports the documentation of the "24PC Series" sensors: the model employed in the present work is the 24PCB differential.

The setup of the used equipment is shown in Figure 14.4: a specifically designed articulated support is used to properly position the sensor; a blue tube

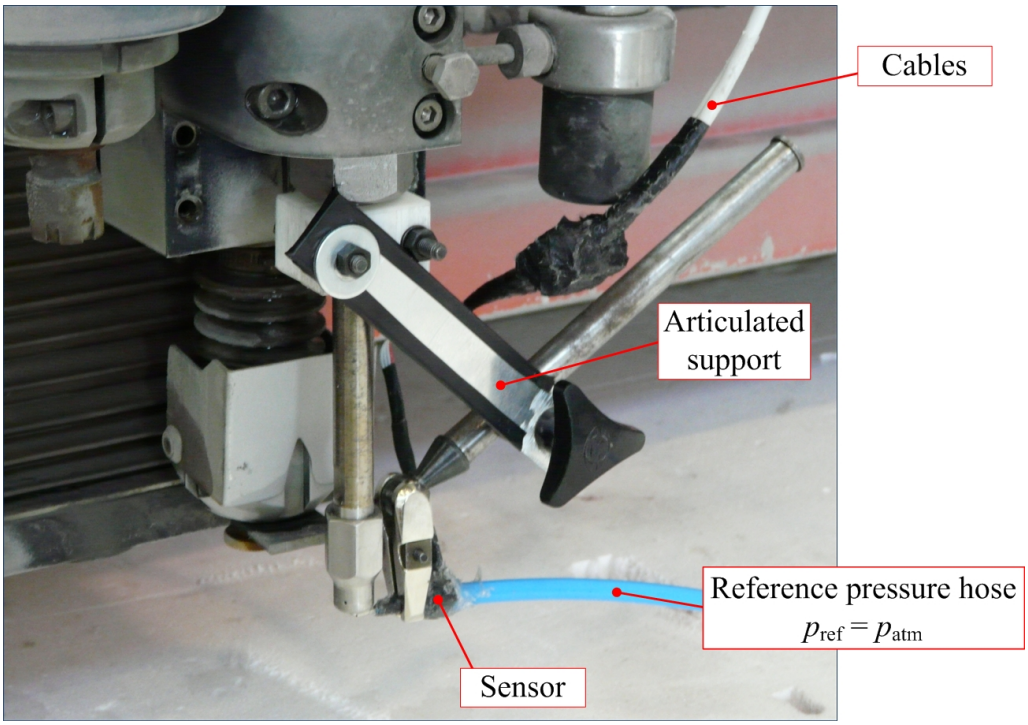

Figure 14.4: *Equipment setup for pressure measurements at the very exit of orifice exit tube*

is linked to the reference pressure inlet hose of the sensor, avoiding the reference pressure p_{ref} to be affected by possible pressure fluctuation close to the working area; electric circuit connections and cables are protected from water by a layer of sealing tape and silicone. Figure 14.5 shows a zooming on the positioning of the sensor and the measured pressure inlet hose: a specifically home-made section-reduced extension of the measured pressure inlet hose allows to reach precisely the interested area for the measurements and to get a precise pressure measurement.

Since we are not interested in capturing the dynamical behavior of the pressure, but just its stationary value, the output signal has been simply read on a voltmeter connected to the electrical circuit (Figure 14.6).

The results of the measurements are depicted in Figure 14.6, where the output voltage values with the jet switched off and on are reported.

$$\Delta V_{meas} = \text{sens}\ (p_{meas} - p_{ref}) = 0.1\ \text{mV} \tag{14.2}$$

where sens is the sensibility of the sensor equal to 23 mV/psi as reported in Appendix A. It is than possible to infer:

$$p_{meas} - p_{ref} = \frac{\Delta V_{meas}}{\text{sens}} = \frac{0.01\ \text{mV}}{23\ \text{mV/psi}} = 4.35\text{E-}04\ \text{psi} = 3\ \text{Pa}$$

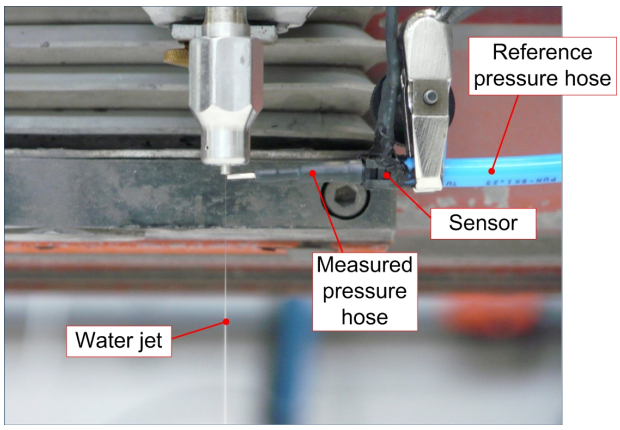

Figure 14.5: *Zoom on the measured pressure sensor hose positioning.*

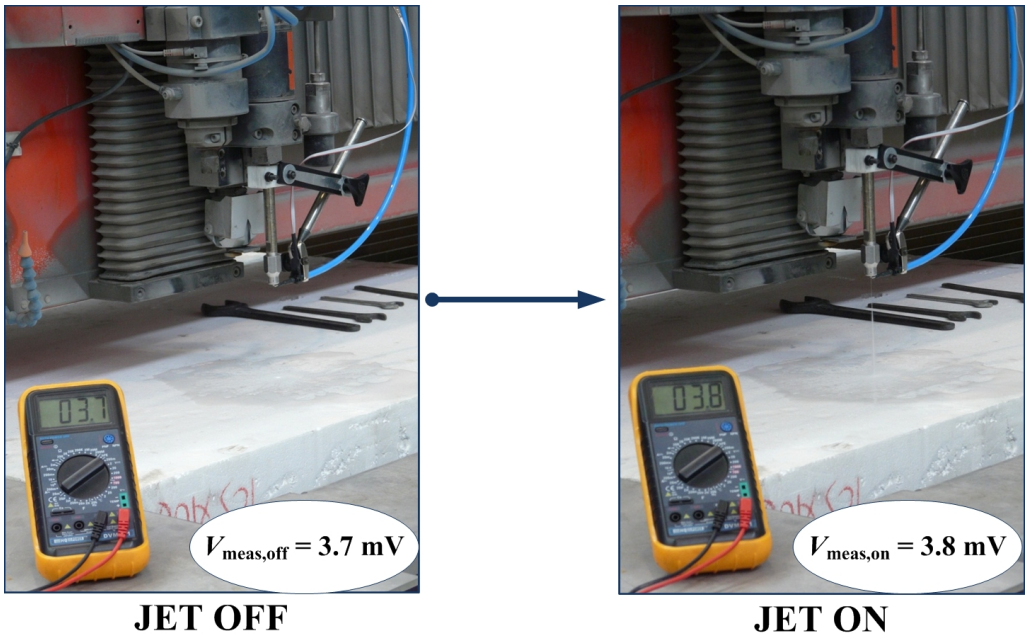

Figure 14.6: *Comparison between the voltage output at jet switched off and on.*

and so

$$p_{meas} = p_{ref} + 3\ \text{Pa} = p_{atm} + 3\ \text{Pa} \cong p_{amb}$$

The pressure measured at the very exit of the exit tube is therefore basically atmospheric which is consistent with the results of the numerical simulation as reported in Figure 14.7: in the measuring area, the numerical model calculates a simulated pressure p_{sim} in the range 101280 Pa $< p_{sim} <$ 101360 Pa.

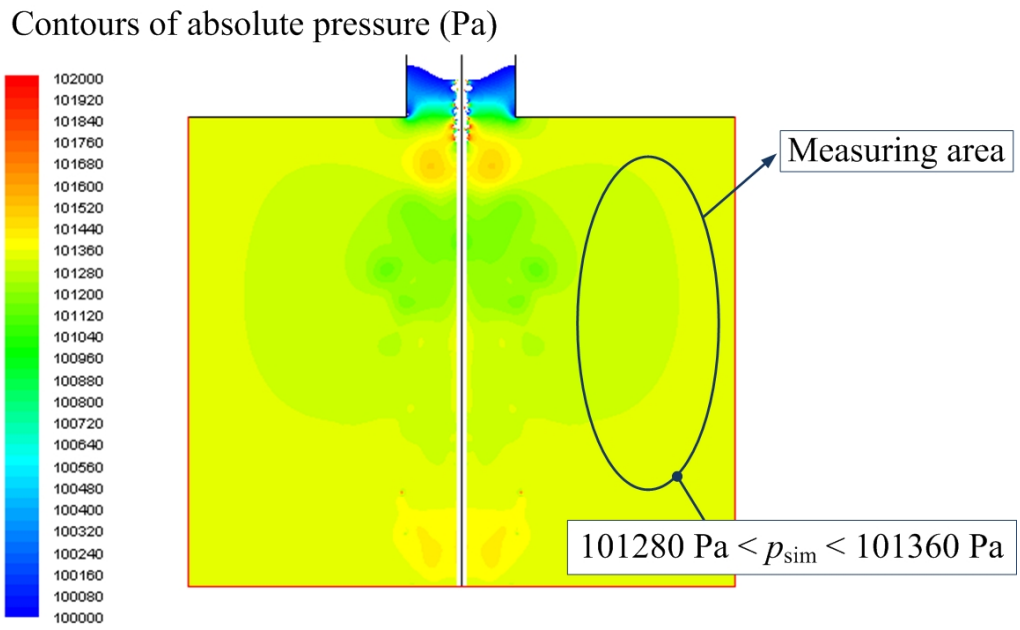

Figure 14.7: *Contours of absolute pressure in the measuring area.*

Note that in Section A.2, along the "outside" boundary, the BC is set up as atmospheric pressure: the previously reported pressure measurements are also useful to confirm that this setting is correct.

14.4 Mass balance through the domain

The following method is not actually a real validation, but rather a further way to check the convergence of the numerical model. In fact, it is suggested [21] to add to the convergence criteria based on the residuals decrease, other controls based on physical quantities (or derived from them); as instance, in the simulation of an aerodynamic structure, the coefficient of drag C_D must tend to a constant value going on with iterations or within each time step in case of unsteady solution. In this case, the mass balance is checked.

Theoretically, for each time step, the mass balance must be respected across the domain (Figure 14.8):

$$(\dot{m}_{w,in} - \dot{m}_{w,out}) + (\dot{m}_{a,in} - \dot{m}_{a,out}) = \Delta\dot{m}_w + \Delta\dot{m}_a = 0 \tag{14.3}$$

where the subscript "w" stands for water, "a" for air, "in" for entering the domain and "out" exiting the domain.

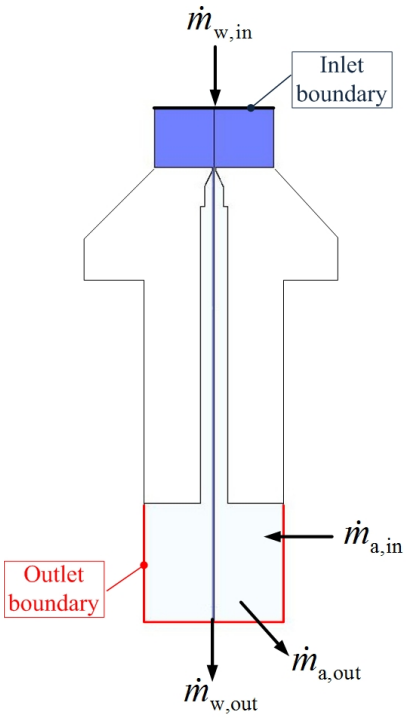

Figure 14.8: *Mass flow rates of water and air across the domain.*

In FLUENT®, it is possible to evaluate the history of mass flow rate balance across the "Inlet" and "Outlet" boundaries, and therefore calculate the history of mass balance, as reported in Figure14.9.

Note that since the equation of continuity is already checked by monitoring its residuals (with the limit set to 1.00E-05), the mass balance has obviously very low values, namely below 1.00E-05; the important remark to point out is rather that the value of mass flow rate balance keeps constant and not fluctuating within each time step, as shown in Figure 14.9; furthermore, its value is always decreasing tending to zero which is consistent with Equation (14.3). As mentioned, this is a further check on model convergence.

14.5 Future developments

Above the previously presented validations, further validations are possible:

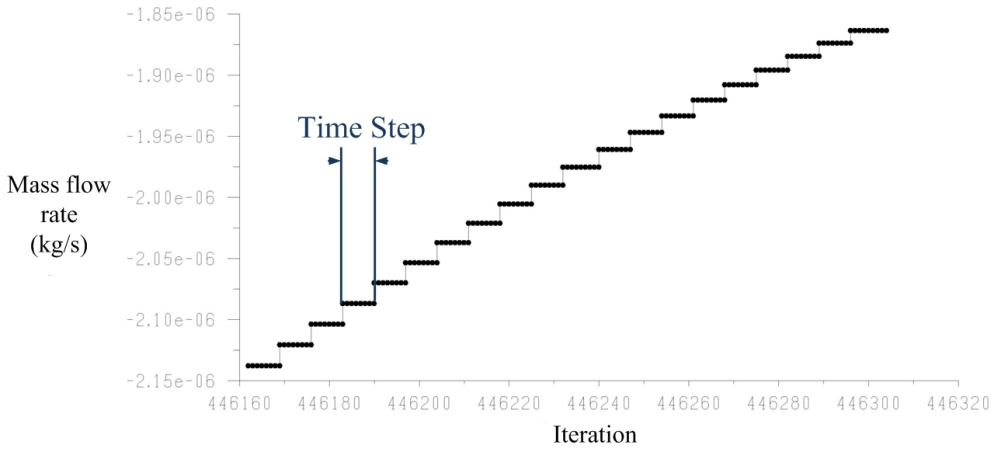

Figure 14.9: *History of mass flow rate balance as a function of iterations*

Velocity measurements by means of LDV: Department of Mechanics in Politecnico di Milano developed an equipment based on the Laser Doppler Velocimetry (LDV) technique, with the aim of measuring the velocity of the water jet [40]; it is therefore possible to measure the jet velocity and compare it with the velocity of the numerical model. The main difficulty in this case is that the jet produced by a PWJ orifice like the one used in present work is really small and coherent, and the setup of the LDV system in this conditions is very difficult and challenging.

Water flow rate measurements: once the velocity of the jet v_{jet} is measured (by means of LDV system for example) and the upstream water volume flow rate $\dot{m}_w$ is known (by means of a flow sensor), then it is possible to evaluate the actual coefficient of contraction C_c of the orifice:

$$\dot{m}_w = C_c \, A_o \, v_{jet} \longrightarrow C_c = \frac{\dot{m}_w}{A_o \, v_{jet}}$$

This value can be directly compared to the one calculated from the numerical model, as presented in Section 14.2.

Besides, it could be possibly used to set up the model geometry: since C_c is strongly dependent on r_{ed}, the radius of curvature of the orifice edge r_{ed} can be varied in the numerical model geometry until the two coefficients coincide.

Chapter 15

Conclusions

The presented work showed how irregular instabilities characterizing a working pure water jet can be coherently explained by disturbances caused by the presence of droplets inside the orifice tube. HSC analysis demonstrates that some water can be present inside the orifice before switching on the jet, while numerical simulations show that other droplets can be formed during the jet creation depending on the inner geometry and working conditions; moreover, condensed humidity, jet breakup or jet disturbances can increase the presence of droplets inside the tube during working conditions.

The droplets staying inside the orifice are then dragged by the high-velocity field created by the air sucked up inside the orifice tube and can possibly hit the jet causing local disturbances responsible for instabilities. Actually, it is shown that the main jet flowing downstream the capillary inside the orifice tube is basically insensible to the presence of droplets around it, since the dragged air surrounding it forms a sort of "protective layer" which prevent the droplets from affecting the jet stream.

The most critical region is localized in the capillary. In fact, when a droplet reaches the capillary, it can overfill its section causing the loss of the hydraulic flip condition: the flow regime can therefore switch into cavitating or single-phase, depending on the droplet dimension and speed. In both cases, theory and literature show that the jet produced by this two flow regimes is not so coherent as if it were in flipped conditions, and this can effectively explain the presence of vapor surrounding the jet and the wider angle at the exit when this irregularities happen.

Moreover, a high-turbulent field is localized inside the capillary and this can eventually enhance atomization and jet breakup when the disturbances due to droplets occur.

The present work belongs to the recent research line proposed by Politecnico

di Milano which intends to get a deeper insight of the water jet process by means of CFD analysis. Further improvements can obviously be done in order to develop always more precise and close-to-reality model, keeping the presented model as a reference starting point. The main guidelines for future developments are listed below:

- The addiction of air compressibility would make possible to track correctly pressure and temperature fields inside the orifice tube. Possible shock-waves or high temperatures can possibly be generated (especially in the high turbulence region in the capillary) and consequently affect the jet stability.

- Simulation of the atomization breakup and spreading of the jet during disturbances, coherently to what happen in reality and to what is seen by high-speed camera analysis. Manual changes to the numerical codes employed by the solver are necessary to achieve this target, since VOF multiphase model cannot simulate changes of phase and so it cannot model the atomization and the creation of vapour around the jet.

- The setup of a discrete phase model in addition to the multiphase model would lead to a three-phase numerical model (water-air-abrasive) which is for sure the most challenging and winning goal. With such a model it would be possible to get (and possibly control) the distribution and the velocity of the abrasive particles, and so the cutting power of the abrasive jet.

The previous developments are surely promising, but all of them bring along numerical problems due to the presence of several physical models in the same numerical simulation. This fact results in convergence difficulties and stability problems, still difficult to overcome.

Bibliography

[1] W. Ohnesorge. Die bildung von tropfen an düsen und die auflosung flüssiger strahlen. *Z. für Angewandte Mathematik und Mechanik*, 16(6):355–358, Dezember 1936. 4, 92, 98, 100, 168

[2] E. Markland A. Lichtarowicz, R. K. Duggins. Discharge coefficients for incompressible non-cavitating flow through long orifices. *Mechanical engineering science*, 7(2):210–219, 1965. 4

[3] A. H. Lefebvre. *Atomization and sprays*. Hemisphere publishing corporation, 1989. 5, 91, 98, 100, 168

[4] G. M. Faeth K. A. Sallam, Z. Dai. Liquid breakup at the surface of turbulent round liquid jets in still gases. *International journal of multiphase flow*, 28:427–449, 2002. 5

[5] A. Tomiyama A. Sou, S. Hosokawa. Effects of cavitation in a nozzle on liquid jet atomization. *International Journal of Heat and Mass Transfer*, (50):3575–3582, 2007. 5

[6] M. Monno M. Annoni. Effects of diamond orifice geometry on water jet cutting performance. In *16th BHR Conference on water jetting*. BHR Group, 2006. 5, 92, 98, 100, 168

[7] B. Pourdeyhimi N. Anantharamaiah, H. Vahedi Tafreshi. A study on flow through hydroentangling nozzles and their degradation. *Chemical Engineering Science*, 61(14):4582–4594, July 2006. 5, 92, 101, 120

[8] G. H. Schnerr W. Yuan. Numerical simulation of two-phase flow in injection nozzles: interaction of cavitation and external formation. *Journal of Fluids Engineering*, 125:963–969, November 2003. 5, 92, 120

[9] D. D. Joseph S. Dabiri, W. A. Sirignano. Cavitation in an orifice flow. *Physics of Fluids*, 19, July 2007. 5, 91

[10] B. Pourdeyhimi N. Anantharamaiah, H. Vahedi Tafreshi. Numerical simulation of the formation of constricted waterjets in capillary nozzles: effects of nozzle geometry. *Chemical Engineering Research and Design*, 84(A3):231–238, 2001. 5, 101, 120

[11] M. Annoni A. T. Basha. Numerical simulation of the formation and reatachment length of water jet for different orifice geometries. In *2009 American WJTA Conference and Expo*, Huston, Texas, August 2009. 5, 97, 101, 120, 133

[12] Wikipedia - the free enciclopedia. Internet website. www.wikipedia.com. 9

[13] M. Monno. Tecnologia water jet / abrasive water jet. Technical report, Politecnico di Milano - Dipartimento di Meccanica. 9, 10, 167

[14] C. Olsen. Waterjets.org - the most complete waterjet resource on the web. Internet website. www.waterjets.org. 14, 167

[15] G. Noseda D. Citrini. *Idraulica*. Casa Editrice Ambrosiana, via Gargano 21, 20139 Milano, seconda edizione edition, 1987. 19, 22, 27, 170

[16] I. M. Cohen P. A. Kundu. *Fluid Mechanics*. Academic Press, 525 B Street, Suite 1900 San Diego, California, 92101-4495, USA http://www.academicpress.com, second edition edition, 2002. 40, 41, 42, 49

[17] A. Bakker. Applied computational dynamics. Tutorial presentations. 41, 42, 43, 45, 46, 48, 51, 53, 68, 167

[18] M. Riva F. Ballio, A. Guadagnini. Meccanica dei fluidi II. Internet tutorials. Notes for Mechanical Engineering course. 49, 52

[19] Cfd online. Internet website about CFD. www.cfd-online.com. 53, 119

[20] S. Thangam V. Yakhot, S. A. Orszag. Development of turbulence models for shear flows by a double expansion technique. *Physics of fluids*, 4(7):1510–1520, 1992. 53

[21] Fluent Inc., *FLUENT 6.3 User's Guide*. 54, 57, 59, 60, 67, 71, 72, 77, 82, 92, 93, 108, 109, 110, 113, 114, 122, 123, 147, 150, 167, 168

[22] A. Shabbir T. H. Shih, W. W. Liou. A new k-epsilon eddy-viscosity model for high reynolds number turbulent flows - model development and validation. *Computers fluids*, 24(3):227–238, 1995. 54

[23] A. Bakker E. M. Marshall. Computational fluid mixing. Technical notes TN144, Fluent Inc., 10 Cavendish Court, Centerra Resource Park Lebanon, NH 03766, January 2001. 55, 60, 61, 167

[24] S. V. Patankar. *Numerical Heat Transfer and Fluid Flow*. Hemisphere, Washington, DC, 1980. 59, 64

[25] W. Malalasekera H. K. Versteeg. *An Introduction to Computational Fluid Dynamics: The Finite Volume Method*. Longman Scientific and Technical, Essex, UK, 1995. 59

[26] S. Mokhtari B. P. Leonard. ULTRA-SHARP nonoscillatory convection schemes for high- speed steady multidimensional flow. NASA TM 1-2568 (ICOMP-90-12), NASA Lewis Research Center, 1990. 62

[27] R. I. Issa. Solution of implicitly discretized fluid flow equations by operator splitting. *Journal of computational physics*, 62:40–65, 1986. 65

[28] M. Peric J. L. Ferzieger. *Computational Methods for Fluid Dynamics*. Springer-Verlag, Heidelberg, 1996. 65

[29] M. Sommerfeld C.U. Böttner. Euler/lagrange calculations of particle motion in turbulent flow coupled with an electric field. In *ECCOMAS Computational Fluid Dynamics Conference*, September 2001. 72

[30] Å. Akademi S. Kallio. On the mixture model for multiphase flow. Publication 288, VTT Energy, 1996. 73

[31] L. Marshall S. A. Velasquez. Multiphase models - separate fluent from the rest. Newsletter, FLUENT Inc., Fall 2004. 73

[32] B. D. Nichols C. W. Hirt. Volume of fluid (vof) method for the dynamics of free boundaries. *Journal of Computational Physics*, 39:201–225, 1981. 78

[33] C. Zemach J. U. Brackbill, D. B. Kothe. Continuum method for modeling surface tension. *Journal of Computational Physics*, 100:335–354, 1992. 83, 84

[34] Contact angle and surface energy measurements on steel. Technical report, First Ten Ångstroms, 465 Dinwiddie Street - Portsmouth, Virginia 23704, July 2003. 84, 120

[35] B. Pourdeyhimi H. Vahedi Tafreshi. Cavitation and hydraulic flip. Fluent news, FLUENT Inc., 13(1): 38, Spring 2004. http://www.fluent.com/about/news/ newsletters/04v13i1/a29.htm. 92

[36] R.D. Reitz S.P. Lin. Drop and spray formation from a liquid jet. *Annual Review of Fluid Mechanics*, 30:85–105, 1998. 98

[37] B. Pourdeyhimi H. Vahedi Tafreshi. The effects of nozzle geometry on waterjet breakup at high reynolds numbers. *Experiments in fluids*, 35:364–371, 2003. 100

[38] Photron Inc. *FASTCAM-APX RS Hardware Manual*. Photron Inc., 1 edition, January 2004. www.photron.com. 103

[39] M. Hashish. Abrasive-waterjet (AWJ) studies. Technical report, Flow International corporation, USA. 145

[40] M. Norgia C. Svelto M. Annoni, L. Castaldi. Measurement of water jet velocity distribution using laser velocimetry. *IEEE TRANSACTIONS ON INSTRUMENTATION AND MEASUREMENT*, 57(8):1524–1528, August 2008. 152

[41] S. Deorowicz and A. Skórczyński. *LEd documentation*. 2004.

[42] A. Bakker E. M. Marshall. Computational fluid mixing. Technical notes, Fluent Inc., Centerra Resource Park
10 Cavendish Court
Lebanon NH 03766 - USA, 2001.

[43] L. Pantieri. *L'arte di scrivere con LaTeX*. http://www.lorenzopantieri.net/, October 2009.

[44] R. D. Webb S. P. Lin. A branching liquid jet. *Physics of Fluids*, 6(8):2671–2675, August 1994.

[45] M. Faeth Z. Dai, W.-H. Chou. Drop formation due to turbulent primary breakup at the free surface of plane liquid wall jets. *Physics of Fluids*, 10(5):1147–1157, May 1998.

[46] T. T. Tuohimaa H. M. Hertz M. Otendal, O. Hemberg. Microscopic high-speed liquid-metal jets in vacuum. *Experiments in Fluids*, 39:799–804, August 2005.

[47] M. Acar E. Ghassemieh, H. K. Versteeg. The effect of nozzle geometry on the flow characteristics of small water jets. *Mechanical Engineering Science*, 220:1739–1753, September 2006.

[48] A. T. Basha I. Etxeberria Agote A. Suarez Gonzalez F. Arleo, M. Annoni. Numerical simulation of a pure wayer jet inside an orifice: jet stability and effect of droplets. BHR Group, October 2010.

[49] P. H. Alfredsson L. D. Soderberg. Experimental and theoretical stability investigations of plane liquid jets. *European Journal of Mechanics - B/Fluids*, 17(5):689–737, 1998.

[50] K. Pianthong M. Behnia S. Zakrzewski, B.E. Milton. Supersonic liquid fuel jets injected into quiescent air. *International Journal of Heat and Fluid Flow*, (25):833–840, 2004.

[51] A. W. Patwardhan M. T. Kandakure, V. G. Gaikar. Hydrodynamic aspects of ejectors. *Chemical Engineering Science*, (60):6391–6402, 2005.

[52] T. Howes B. S. Cheong. Capillary jet instability under the influence of gravity. *Chemical Engineering Science*, (59):2145–2157, February 2004.

[53] K. A. Sallam C.-L. Ng, R. Sankarakrishnan. Bag breakup of non turbulent liquid jets in cross flow. *International Journal of Multiphase Flow*, (34):241–259, 2008.

[54] F. J. Salvador J. Gimeno R. Payri, J. M. Garcia. Using spray momentum flux measurements to understand the influence of diesel nozzle geometry on spray characteristics. *Fuel*, (84):551–561, 2005.

Appendices

Appendix A

Differential uncompensated pressure transducers 24PC type

Pressure Sensors

24PC Series

Gage and Differential/Unamplified-Noncompensated

Basic Sensors

FEATURES

- Lowest priced pressure sensor
- Miniature package
- Variety of gage pressure port configurations - easily and quickly modified for your special needs
- Choice of termination for gage sensors
- 2 mA constant current excitation significantly reduces sensitivity shift over temperature *
- Can be used to measure with vacuum or positive pressure

24PC SERIES PERFORMANCE CHARACTERISTICS at 10.0 ±0.01 VDC Excitation, 25°C

	Min.	Typ.	Max.	Units
Excitation	---	10	12	VDC
Null Offset	-30	0	+30	mV
Null Shift, 25° to 0°, 25° to 50°C	---	±2.0	---	mV
Linearity, P2 > P1, BFSL	---	±0.25	±1.0	%Span
Sensitivity Shift, 25° to 0°, 25° to 50°C	---	±5.0*	---	%Span
Repeatability & Hysteresis	---	±0.15	---	%Span
Response Time	---	---	1.0	msec
Input Resistance	---	5.0 K	---	ohms
Output Resistance	---	5.0 K	---	ohms
Stability over One Year	---	±0.5	---	%Span
Weight	---	2	---	grams

ENVIRONMENTAL SPECIFICATIONS

Operating Temperature	-40° to +85°C (-40° to +185°F)
Storage Temperature	-55° to +100°C (-67° to +212°F)
Shock	Qualification tested to 150 g
Vibration	Qualification tested to 0 to 2 kHz, 20 g sine
Media (P1 & P2)	Limited only to those media which will not attack polyetherimide, silicon and fluorosilicone seal

24PC SERIES ORDER GUIDE

Catalog Listing	Pressure Range psi	Span, mV			Sensitivity mV/psi Typ.	Overpressure psi Max.
		Min.	Typ.	Max.		
24PCE Type	0.5	24	35	46	70	20
24PCA Type	1.0	30	45	60	45	20
24PCB Type	5.0	85	115	145	23	20
24PCC Type	15	165	225	285	15	45
24PCD Type	30	240	330	420	11	60
24PCF Type	100	156	225	294	2.25	200
24PCG Type	250	145	212	280	0.85	500

* Non-compensated pressure sensors, excited by constant current instead of voltage, exhibit temperature compensation of Span. Application Note #1 briefly discusses current excitation.

Constant current excitation has an additional benefit of temperature measurement. When driven by a constant current source, a silicon pressure sensor's terminal voltage will rise with increased temperature. The rise in voltage not only compensates the Span, but is also an indication of die temperature.

Constant Current Excitation Schematic

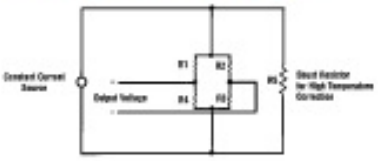

Figure A.1: *Technical characteristics of differential uncompensated pressure transducers 24PC type*

Pressure Sensors

24PC Series

Gage and Differential/Unamplified-Noncompensated

SENSOR SELECTION GUIDE

2 Product Family	4 Circuit Type	PC Pressure Transducer	A Pressure Range	F* Type of Seal	A Type of Port	2 Termination Style	G Pressure Measurement
2 20PC family	**4** Noncompensated		**A** 1 psi **B** 5 psi **C** 15 psi **D** 30 psi **E** 0.5 psi **F** 100 psi **G** 250 psi	**F** Fluorosilicone	**A** Straight **B** Barbed **C** Luer **D** Modular **H** M5 Thread **I** 90° Port **J** Needle **M** ¼ - 28 UNF Thread	**1** 1 x 4 **2** 2 x 2	**G** Gage **D** Differential

Example: 24PCAFA2G
Standard, non-compensated 1 psi sensor with fluorosilicone seal, straight port, 2 x 2 terminals, and Gage pressure measurement.
*Other media seal materials may be available.

ACCESSORIES SELECTION GUIDE

Catalog Listing	Description
PC10182	Steel locking (Included with Port Style A, 1 x 4 terminals only)
PC10949	Single hole plastic bracket (Must be separately ordered)

Not all combinations are established. Contact 800 number before final design. The following listings are typically stocked in small quantities.

Unamplified

Figure A.2: *Technical characteristics of differential uncompensated pressure transducers 24PC type*

List of Symbols and Abbreviations

Symbol	Description	Definition
A_{jet}	Water jet section area	page 146
A_{o}	Nominal capillary section area	page 146
Ca	Capillary number	page 83
d_{o}	Orifice capillary nominal diameter	page 88
$D(\kappa)$	Dissipation rate spectrum	page 47
$E(\kappa)$	Turbulent energy spectrum	page 46
I	Turbulent intensity	page 117
k	Turbulent kinetic energy	page 42
k_{eff}	Effective thermal conductivity	page 81
L_{o}	Capillary length	page 88
Oh	Ohnesorge stability number	page **??**
p	Pressure	page 20
p_{atm}	Atmospheric pressure	page 147
p_{down}	Downstream pressure	page 92
p_{up}	Upstream pressure	page 92
p_{meas}	Measured pressure	page 147
p_{ref}	Reference pressure	page 147
p_{v}	Vapor pressure	page 92
$\dot{p}$	Particulate loading	page 74
Pe	Peclet number	page 61
r_{ed}	Radius of curvature of orifice edge	page 91
Re	Reynolds number	page 40
Re_{h}	Reynolds number based on hydraulic head	page 93
Re_{λ}	Taylor-scale Reynolds number	page 45
s	Surface tension	page 22
St	Stokes number	page 75
T	Temperature	page 20
$\mathbf{v}$	Velocity vector	page 27
v_{th}	Theoretical velocity	page 145

Symbol	Description	Definition
v_{sim}	Simulated velocity	page 145
We	Weber number	page 84
γ	Specific gravity	page 20
ϵ	Modulus of elasticity of volume	page 21
ε	Turbulent dissipation rate	page 42
θ	Contact angle	page 84
κ	Turbulent wavenumber	page 46
λ	Taylor microscale	page 45
μ	Cinematic viscosity	page 23
μ_t	Turbulent viscosity	page 52
ν	Dynamic viscosity	page 24
ν_t	Turbulent cinematic viscosity	page 52
ρ	Density	page 20
$\underline{\mathbf{\Phi}}$	Stress tensor	page 33

Abbreviation	Description	Definition
AWJ	Abrasive Water Jet	page 12
BC	Boundary Conditions	page 37
CFD	Computational Fluid Dynamics	page 48
CV	Control Volume	page 27
EDM	Electrical Discharge Machining	page 17
HAZ	Heat Affected Zone	page 15
IC	Initial Conditions	page 37
PWJ	Pure Water Jet	page 12
RANS	Raynolds Averaged Navier-Stokes equations	page 50
URF	Under Relaxation Factor	page 67
VOF	Volume Of Fluid	page 73
WJ	Water Jet	page 9

List of Figures

List of Tables